

Creation of electron pulses with a laser-triggered micro fabricated electron beam deflector

Weppelman, I.G.C.

DOI

[10.4233/uuid:09ea6341-6dc2-4b01-ad33-d5d38e0bc282](https://doi.org/10.4233/uuid:09ea6341-6dc2-4b01-ad33-d5d38e0bc282)

Publication date

2021

Document Version

Final published version

Citation (APA)

Weppelman, I. G. C. (2021). *Creation of electron pulses with a laser-triggered micro fabricated electron beam deflector*. [Dissertation (TU Delft), Delft University of Technology].
<https://doi.org/10.4233/uuid:09ea6341-6dc2-4b01-ad33-d5d38e0bc282>

Important note

To cite this publication, please use the final published version (if applicable).
Please check the document version above.

Copyright

Other than for strictly personal use, it is not permitted to download, forward or distribute the text or part of it, without the consent of the author(s) and/or copyright holder(s), unless the work is under an open content license such as Creative Commons.

Takedown policy

Please contact us and provide details if you believe this document breaches copyrights.
We will remove access to the work immediately and investigate your claim.

Creation of electron pulses with a laser-triggered micro fabricated electron beam deflector



The work in this dissertation was conducted at the Charged Particle Optics Group, Department of Imaging Physics, Faculty of Applied Sciences, Delft University of Technology.

Printed by: Ridderprint, www.ridderprint.nl

ISBN: 978-94-6416-960-7

Cover: View along the Easton Glacier climbing route, photo taken by the author during a climb to the summit of Mt. Baker in WA, USA.

An electronic version of this dissertation is available at

<http://repository.tudelft.nl/>

Creation of electron pulses with a laser-triggered micro fabricated electron beam deflector

Dissertation

for the purpose of obtaining the degree of doctor

at Delft University of Technology

by the authority of the Rector Magnificus, Prof.dr.ir. T.H.J.J. van der Hagen

chair of the Board for Doctorates

to be defended publicly on

Tuesday the 14th of December 2021 at 12:30 o'clock

by

Izaäk Gerrit Cornelis WEPPELMAN

Master of Science in Applied Physics, Delft University of Technology, the Netherlands

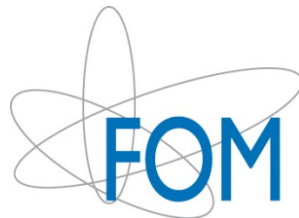
born in Lingewaal, the Netherlands

This dissertation has been approved by the promotors.

Composition of the doctoral committee:

Rector Magnificus,	chairperson
Prof.dr.ir. P. Kruit	Delft University of Technology, promotor
Dr.ir. J.P. Hoogenboom	Delft University of Technology, promotor
Independent members:	
Prof.dr. H.P. Urbach	Delft University of Technology
Prof.dr. P.C.M. Planken	Advanced Research Center for Nanolithography/University of Amsterdam
Prof.dr.ir. O.J. Luiten	Eindhoven University of Technology
Dr.ir. D. Maas	TNO Delft
Dr.ir. E.R. Kieft	Thermo Fisher Scientific

This research was funded by FOM Foundation for Fundamental Research on Matter (FOM), which is part of the Netherlands Organization for Scientific Research (NWO).



Contents

<i>Abstract</i>	9
<i>Samenvatting</i>	11
1 Introduction.....	15
1.1 Ultrafast Electron microscopes.....	17
1.2 Applications of Ultrafast electron microscopy.....	18
1.3 Challenges in ultrafast SEM.....	19
1.4 Outline of the thesis.....	20
2 An experimental platform for time-resolved, high spatial resolution integrated light and electron microscopy.....	25
2.1 Introduction.....	25
2.1.1 Cathodoluminescence microscopy.....	25
2.1.2 Laser-pump electron-probe microscopy.....	26
2.1.3 Outline.....	27
2.2 Femtosecond laser excitation in a SEM vacuum chamber.....	27
2.3 Generation and characterization of a pulsed electron beam.....	29
2.4 Proof-of-principle result for pump-probe microscopy.....	31
2.5 Discussion.....	33
2.6 Conclusions.....	34
Bibliography.....	35
3 Concept and design of a beam blanker with integrated photoconductive switch for Ultrafast Electron Microscopy.....	39
3.1 UFB concept and requirements.....	40
3.2 Photoconductive switch.....	42
3.2.1 Response time photoconductive switch.....	43
3.2.2 Electric field strength over the photoconductive switch.....	44
3.2.3 Conductivity photoconductive switch.....	45
3.3 Transmission of high frequency signals and implications for the design.....	45
3.4 Dimension MEMS Beam Blanker.....	46
3.5 Electron pulse length.....	48
3.6 Time jitter between the laser pulse and the electron pulse.....	51
3.7 Discussion.....	52
3.8 Conclusion.....	53
3.9 Acknowledgements.....	54

Appendix – Model photoconductive switch and electrical circuit.....	55
Bibliography	59
4 Pulse length, energy spread, and temporal evolution of electron pulses generated with an ultrafast beam blanker.....	63
4.1. Simulation setup, model and approximations.....	64
4.2. Model for the time-dependent conductivity of the photoconductive switch.....	66
4.3. Particle tracing of the electron beam and beam quality.....	70
4.4. Energy gain introduced by the blanker.....	72
4.5. Estimation energy gain of the UFB	74
4.6. Estimation energy spread.....	77
4.7. Temporal distortion of the electron pulse due to energy spread and magnetic lens	78
4.8. Influence of even versus odd UFB voltage switching.....	79
4.9. Conclusions	80
4.10. Acknowledgements.....	81
Appendix A – Sensitivity of simulation results to mesh refinement	82
Appendix B – Energy spread induced by quasi-static fields	84
Appendix C – Maple worksheet of the blur calculation.....	87
Bibliography.....	90
5 MEMS Fabrication of the UFB and incorporation in the SEM.....	93
5.1 UFB fabrication requirements.....	94
5.2 Overview of UFB microfabrication and quality control process	94
5.3 Design and fabrication of photoconductive switch electrodes	96
5.3.1 Grating electrode design	96
5.3.2 Fabrication of the photoconductive switch with grating electrodes.....	97
5.4 Fabrication and quality control of the MEMS deflector.....	98
5.4.1 Microfabrication process of the deflector.....	98
5.4.2 Deflector voltage and resistance measurements.....	102
5.5 Design blanker stick and alignment laser	103
5.5.1 Design of the blanker stick	103
5.5.2 Blanker mounting and alignment of the laser optics	104
5.5.3 Mounting of the blanker in the SEM and electron optics alignment	105
5.6 Initial characterization electron pulse length and performance	107
5.7 Discussion.....	112
5.8 Conclusion.....	113

Bibliography.....	114
Appendix B - Background signal elastically scattered electrons	117
6 Valorisation and applications	119
6.2 Valorisation	120
6.2.1 Towards a prototype - Design improvements	121
6.2.2 Incorporation in a TEM.....	123
6.3 Application for Ultrafast SEM	124
6.4 Bunching and pulse shaping of femtosecond electron pulses	124
6.5 Conclusion.....	127
Bibliography.....	127
Appendix	129
<i>Acknowledgements</i>	130
<i>Curriculum Vitae</i>	136

Abstract

This thesis is dedicated to the development of a beam blanker for Ultrafast Electron Microscopy. Ultrafast electron microscopy aims to resolve structural dynamics at the nanometer and (sub) picosecond time scale. In these temporal and spatial scales many important processes in physics, chemistry and biology do occur. Examples of these are the interaction of light with small nano-patterned devices, the propagation of acoustic waves and phonons, the dynamics of melting and crystallization of materials. An example in biology is in photosynthesis, i.e. the dynamics of light harvesting complexes.

In the introduction, chapter 1, we describe the current state of the art in electron microscopy, where very high spatial resolution can be reached: Currently EMs can achieve resolution in the Angstrom domain. To also enable temporal imaging, ultrafast electron microscopes have been developed that utilize pulsed electron beams. However, these microscopes typically require drastic modifications to the source unit in order to generate the pulses. Furthermore, to obtain high resolution in the temporal domain is still challenging. A technique that can change an existing EM easily into a time-resolved apparatus operating with short pulses, for instance using a retractable blanker, is lacking.

In Chapter 2 we revisit and show experiments where we push a standard commercial electrostatic blanker to pulse lengths below 100 ps. A streak camera is developed and characterized and measurements show that 90 ps pulses are created with a standard electrostatic blanker, which is more than sufficient for many photoluminescence and nanophotonics studies.

Time-resolved experiments in the ultrafast domain are often measured in a stroboscopic manner where a laser pulse acts as a pump and an electron pulse as a probe. Hence we present an optical setup to couple a femtosecond laser into the vacuum chamber of a ThermoFisher FEI Quanta 200 SEM to illuminate the sample. We show we can compensate for the dispersion of light in the objective lens and vacuum window to achieve a pulse length of 15 fs and spatial resolution of 620 nm. Subsequently we show a proof-of-principle pump-probe experiment on a semiconductor sample, aimed at resolving carrier dynamics by secondary electron contrast. A flake of MoS₂ is deposited on an ITO-coated glass slide, the flake is illuminated with an infrared laser pulse, and the 90 ps electron pulses are varied in time delay with respect to the laser pulse.

In Chapter 3 we present a new and alternative method to create femtosecond electron pulses. In this thesis we investigated an approach whereby an ultrafast EM should be such that a user can rapidly switch between normal imaging mode and ultrafast mode of operation. For this, we use the concept of an electrostatic beam deflector, we make it compact (so it can be easily inserted in the beam line via standard entry ports of an EM) and we require electromagnetic fields with extremely fast rise times. So in Chapter 3 we propose to combine an electrostatic switch with an electrostatic beam deflector. The deflector will sweep over an aperture to create ultrafast electron pulses. With back-of-the-envelope calculations we estimate the required dimensions of such an ultrafast beam blanker (UFB). These calculations indicate that a tens of

micrometers sized deflector and photoconductive switch would be required. Low temperature grown GaAs is a preferred semiconductor material as it allows the switch to rapidly go back to the dark state after illumination with a laser pulse.

In Chapter 4 we perform numerical calculations in COMSOL to model the UFB with a finite element method in full 3D. The response of the photoconductive switch is modeled with a Drude-Lorentz model, the laser pulse is modeled as having a Gaussian temporal shape. The electromagnetic fields in the simulation are calculated with the full Maxwell equations, so wave like behavior is taken into account in the simulation. An electron beam is traced through the deflector, and the potential brightness reduction and energy spread are calculated. Retardation effects are visible in the energy spread when the ground plate does not shield the deflector plate enough causing a significant increase in the energy spread of the beam in the order of 4 eV. We also present a design with proper shielding of the fluctuating fields the induced energy spread is reduced significantly to values below the energy spread of a Schottky source (0.6 eV), also the energy spread can be estimated with analytical models and related to the pulse length, beam brightness and current. No significant reductions in beam brightness are observed in the calculations.

Chapter 5 of this thesis describes a microfabrication process flow to make the ultrafast beam blanker, a design and light optical alignment of an insert (containing the ultrafast beam blanker) to bring the blanker into the beamline of a SEM and couple a laser beam in and focus it on the photoconductive switch. The photoconductive switch has a grating shaped electrode with a pitch of 100 nm, to enhance the photoconductivity. The device is fabricated with standard clean room techniques, i.e. thin film deposition, electron beam lithography, wafer dicers and focused ion beam milling.

Measurements of the DC current through a photoconductive switch we fabricated show that per laser pulse a factor 6 more than enough electron hole pairs are created than required to invert the voltage at the deflector plate of the UFB. Streak camera measurements show that the laser pulses induce deflection of the electron beam. Electron pulses created with the UFB are detected with an avalanche photodiode and time-correlator, however the exact pulse length could not be determined due to the about 1 ns response time of the scintillator and jitter of the avalanche photodiode.

Finally, we examined the valorization potential of the technology developed in this thesis. In Chapter 6 we describe the required improvement steps and technology readiness levels of the prototype developed in this thesis. Also potential applications of ultrafast SEM with the ultrafast beam blanker are discussed as well as the incorporation of our system in a STEM with beam energies in the 100-200 kV range. For the latter case we show that 100 fs pulses can be created with negligible or less than 1 eV in energy spread. Plots are given to show an operator in what range of current and pulse length the induced energy spread will be. Finally, numerical calculations are shown demonstrating that with some modifications to the design of the ultrafast beam blanker it can also be used as a buncher to compress electron pulses to less than 10 fs.

Samenvatting

Dit proefschrift gaat over de ontwikkeling van een elektronenbundel deflector voor ultrasnelle elektronen microscopie. Het doel van ultrasnelle elektronmicroscopie is om de dynamica in materialen te volgen met nanometer resolutie en op (sub-)picoseconde tijdschalen. Op deze schalen vinden veel belangrijke processen plaats in de natuurkunde, scheikunde en biologie. Voorbeelden hiervan zijn de interactie van licht met structuren gepatroneerd op een nanoschaal, de propagatie van akoestische golven en fononen, de dynamica van smeltprocessen en kristallisatie van materialen. Een voorbeeld in de biologie is de dynamica in de macromoleculaire complexen betrokken bij fotosynthese.

In het introductie hoofdstuk beschrijven we de huidige staat van de technologie in elektronenmicroscopie, waar hoge spatiale resoluties kunnen worden behaald: vandaag de dag zijn resoluties van 0,1 nanometer mogelijk. Om ook oplossend vermogen in de tijd te behalen worden gepulsde elektronenbundels gebruikt. Voor een hoge resolutie in ultrasnelle elektronenmicroscopie zijn zeer korte pulsen, onder de nanosecondes tot honderd femtosecondes, nodig. Om zulke pulsen te kunnen genereren hebben deze microscopen echter drastische modificaties nodig van de elektronenbron. Het verkrijgen van hoge resoluties in tijd is bovendien nog steeds een uitdaging. Een techniek die een bestaande elektronenmicroscop (EM) eenvoudig verandert in een tijds-opgeloste EM met korte elektronenpulsen ontbreekt. Een deflector die in en uit de microscoop te schuiven is, zou hier een oplossing voor kunnen zijn.

In hoofdstuk 2 laten we zien hoe met een standaard commerciële elektrostatistische blanker elektronen pulsen gemaakt kunnen worden. Om de duur van deze pulsen te meten, is een tijdsopgeloste camera ontwikkeld en gekarakteriseerd. De metingen laten zien dat elektronenpulsen van 90 ps met deze deflector gecreëerd kunnen worden, wat meer dan voldoende is voor veel studies op het gebied van luminescentie en nanofotonica.

Tijdsopgeloste experimenten in het ultrasnelle tijdsdomein worden vaak gedaan met stroboscopische technieken waar een laser puls gebruikt wordt om een systeem te modificeren en de elektronenpuls om een signaal te genereren op een vaste tijdsinterval na de laserpuls. Met dit doel wordt een optische opstelling gepresenteerd waarin een femtoseconde laser ingekoppeld wordt in de vacuüm kamer van een ThermoFisher FEI Quanta 200 SEM om een monster te belichten. We laten zien dat de dispersie van licht in het objectief en glazen vacuüm venster gecompenseerd kan worden zodat een pulse lengte van 15 fs en spatiele resolutie van 620 nm bereikt kan worden. Vervolgens laten we een demonstratiemeting zien op een halfgeleider materiaal, een dun stukje MoS₂, waarbij de MoS₂ wordt belicht met infrarode laserpulsen, en de 90 ps elektronen pulsen om de hoeveelheid geëxciteerde elektronen en gaten te meten als functie van de tijdsvertraging van de elektronenpuls ten opzichte van de laserpulsen.

In hoofdstuk 3 presenteren we onze nieuwe en alternatieve methode om femtoseconde elektronen pulsen te creëren. Hiervoor gebruiken we wederom een compacte elektrostatistische deflector, die via een standaard toegangspoort in de EM gebracht kan worden. Om sub-picoseconde pulsen te genereren, zijn daarnaast elektromagnetische velden met snelle

stijgtijden vereist. Om die reden stellen we in hoofdstuk 3 voor om een fotogeleidende schakelaar te combineren met een electrostatische deflector. De deflector zwenfelt de elektronenbundel over een apertuur om ultrakorte elektronen pulsen te creëren. Met schattingen op basis van fysische modellen bepalen we de dimensies van zo'n deflector en daaruit volgt dat dimensies in de orde van tientallen micrometers nodig zijn. Daarnaast is GaAs gegroeid op lage temperatuur nodig zodat de fotogeleidende schakelaar snel teruggaat naar de donkere toestand na belichting met een laser puls. Hoofdstuk 3 levert ons uiteindelijk een concept voor een laser-gestuurde ultrasnelle deflector voor elektronenmicroscopie.

In hoofdstuk 4 voeren we drie-dimensionale numerieke berekeningen met een eindige elementen methode uit om de ultrasnelle deflector verder te modelleren. De respons van de fotogeleidende schakelaar is gemodelleerd met een Drude-Lorentz model en de laser puls met een Gaussische puls. De elektromagnetische velden in de simulatie zijn berekend met de volledige Maxwells vergelijkingen, waardoor golfgedrag is meegenomen in de simulatie. Vervolgens traceren wij een elektronenbundel door de deflector, en kunnen zo de potentiële reductie van helderheid en toename van energiestreiding meenemen in de simulatie. Retardatie-effecten worden zichtbaar in de energiestreiding wanneer de grondelectrode de deflector niet voldoende afschermt. In dat geval neemt de energiestreiding toe met ongeveer 4 eV. We presenteren ook een ontwerp waarin de deflector en daarmee de fluctuerende velden in de deflector voldoende worden afschermd, in dat geval wordt de energiestreiding significant gereduceerd tot ongeveer 0.6 eV. De energiestreiding kan ook geschat worden met analytische modellen als functie van de puls lengte, bronhelderheid en stroom. In de berekeningen worden verder geen significante helderheidsreducties waargenomen.

Hoofdstuk 5 van dit proefschrift beschrijft de microfabricage van de ultrasnelle deflector, het ontwerp van de retractiestok om de deflector in de bundellijn van een EM te kunnen plaatsen en het licht optische systeem om een laser in te koppelen en te focuseren op de fotogeleidende schakelaar. Op de fotogeleidende schakelaar brengen we elektrodes met een 100 nm afstand traliestructuur aan om de fotogevoeligheid te verbeteren. De ultrasnelle deflector wordt gemaakt met standaard microfabricage technieken, zoals dunne film depositie, elektronen bundel lithografie, wafersnijders en gefocusseerde ionenbundels.

Hoofdstuk 5 beschrijft verder karakterisatie metingen van deze ultrasnelle deflector. Metingen van de gelijkstroom van de door ons geproduceerde de fotogeleidende schakelaar laten zien dat per laser puls een factor 6 meer elektron-gat paren geproduceerd worden dan benodigd zijn. Metingen met een tijdsopgeloste camera laten zien dat de laserpulsen inderdaad tot een afbuiging van de elektronenbundel leiden. Elektronenpulsen gemaakt met de deflector zijn gedetecteerd met een gevoelige fotodiode en tijds correlator, echter de exacte pulslengte kon niet afgeschat worden vanwege de tijdsjitter van ongeveer 1 ns in de scintillator en fotodiode.

Tenslotte beschouwen we de valorisatiepotentieel van de technologie beschreven in dit proefschrift. In hoofdstuk 6 beschrijven we de benodigde verbeteringen en de niveaus van gereedheid van de technologie voor het prototype ontwikkeld in dit proefschrift. Ook worden potentiële applicaties van ultrasnelle EM in een rasterlektronenmicroscop (SEM: scanning electron microscope) bediscussieerd als ook als de incorporatie in een raster transmissie-

elektronenmicroscop (STEM: scanning transmission electron microscope) met bundel energieën van 100-200 kV. Voor het laatste geval laten we zien dat 100 fs elektronpulsen gemaakt kunnen worden met energiespreidingen van minder dan 1 eV. Wij laten wat grafieken zien die een operator in staat stellen te bekijken wat de energiespreiding zal zijn bij een bepaalde keus van stroom en pulslengte zal zijn. Tenslotte laten we met numerieke berekeningen zien dat met een aantal aanpassingen aan het ontwerp van de UFB het mogelijk is om elektronpulsen te comprimeren in tijd.

1 Introduction

The dream of every microscopist would be a microscope to observe the movement of atoms in space and time to resolve melting, chemical reactions and interaction with photons. Electron microscopes (EM) achieve atomic resolutions, depending on beam acceleration voltage, an electron has a wavelength of about 10 pm, hence the diffraction limit implies that high spatial resolutions can be obtained. However, round lenses suffer from aberrations, which limits the opening angle of an electron beam to a few 10s of mrad. In fact Scherzers theorem states that a rotationally symmetric electro/magneto static lens will always suffer from a positive aberration coefficient. This constitutes a major limitation to the spatial resolution that can be obtained with electron microscopes. Only relatively recently aberration correctors have been developed that made it possible to increase the resolution to about 50 pm.

The aberrations of electron lenses limit, for a fixed current I , the opening angle α . The reduced brightness of an electron source is therefore important and is defined as:

$$B_r = \frac{4I_p}{\pi\phi\alpha^2 d_v^2} \quad (0.1)$$

where ϕ is the beam energy, and d_v is the geometrical probe size. The reduced brightness of electron sources varies from 10^4 A/(m²·sr·V) in the case of tungsten hairpin sources, to about 10^8 A/(m²·sr·V) for the commonly used Schottky sources [1] and between 10^8 and 10^9 A/(m²·sr·V) for cold field emitters.[2] Another important quality of a source is the energy spread, as this influences the amount of chromatic aberration and because it determines the energy resolution in electron energy loss spectroscopy (EELS). For a Schottky emitter, the energy spread is typically about 0.6 eV.

Over time electron microscopes were further improved, and thanks to the mentioned recent development of aberration correctors, commercial microscopes can reach atomic resolution. Nowadays, EMs are commonly employed to image structural defects, nanostructures, and protein structures. Hence, in the spatial domain the resolution seems sufficient and in practice sometimes not anymore limited by electron optics or electron source properties but by sample degradation due to the electron beam. However, compared to the drive to achieve high spatial resolution, much less attention has been devoted to techniques that can do temporal imaging, especially to achieve temporal resolution in the ultrafast (picosecond and lower) domain.

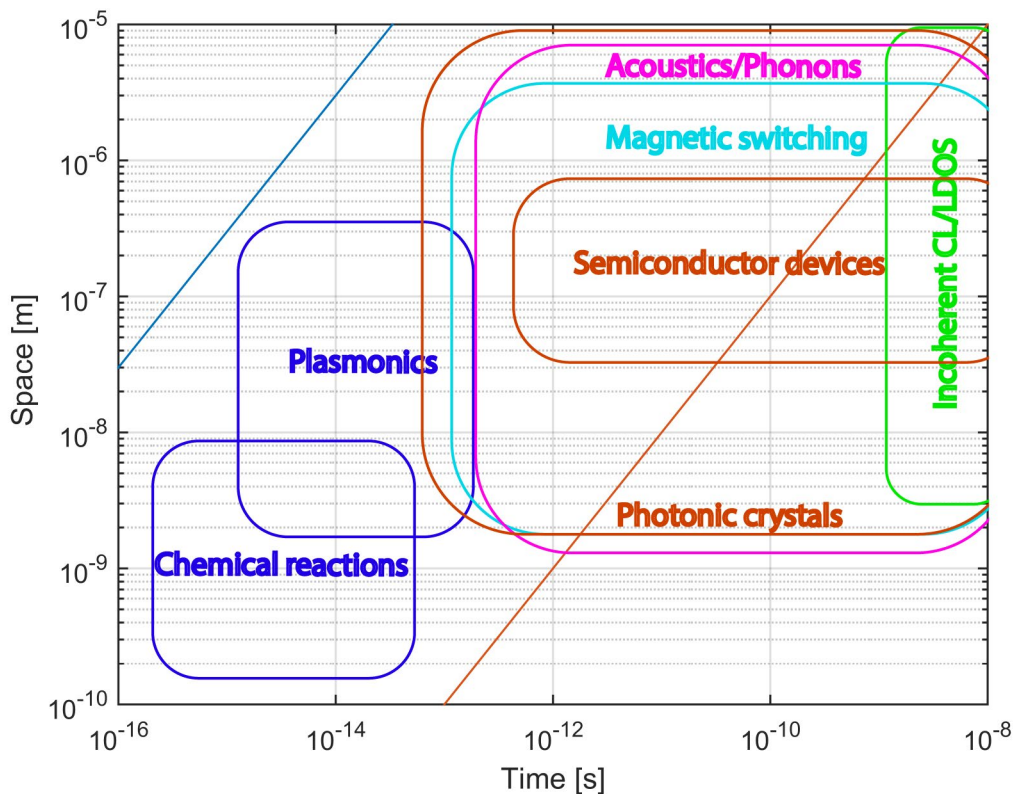


Figure 1.1: Various physical processes that take place at fast and ultrafast time and length scales, the boxes are meant to give a rough estimation. The blue line denotes the boundary of photon imaging, all indicated physical processes occur at length and time scales below this line. The red line is a phonon line with a velocity of 1000 m/s. As can be seen, many physical processes occur at ultrafast (< 10 ps) time scales and at spatial resolutions below the diffraction limit of light. The latter could be overcome with ultrafast electron microscopy.

This is a serious limitation as a wide variety of elementary physical processes occur at ultrafast, sub-picosecond time scales and at (sub-)nanometer spatial scales (see Figure 1.1). [3] Examples are chemical reactions, where during a chemical reaction a molecule is out of equilibrium which is challenging to numerically calculate. Another example is plasmonics and nanophotonics, where light can be confined at a spatial scale below the optical diffraction limit. A method to resolve materials dynamics in time and space below the diffraction limit of light is attractive as optical properties are critically determined by the crystallinity and exact morphology of the sample. Also the dynamics of acoustical waves and phonons depend on the morphology of the sample, and occur at spatial and temporal timescales relevant for UEM. Experimental methods to reveal the precise relations between these ultrafast processes and sample properties such as morphology are thus required for basic understanding and also to verify the performance, quality control and understanding of nanoscale devices. The same argument holds for semiconductor devices. The study of incoherent light emission and excited state dynamics of a molecule and the emission of a photon can be critical to the performance of nanophotonic devices and occur in time scales of 1 ns and longer, which will be discussed more extensively in Chapter 2 of this thesis. Finally, another example is the dynamics of magnetization processes at ultrafast and nanometric spatial scales. [4]

This thesis focuses on the development of methods for time-resolved, ultrafast electron microscopy, with the aim to create a focused, pulsed electron beam with resolution in the low

picosecond or femtosecond time range. Sources for ultrafast electron diffraction are not discussed in this thesis, there the aim or 'holy grail' is to create single shot diffraction patterns. This requires electron pulses containing about a million electrons, while for UEM electron pulses will be focused on the sample and if a pulse contains more than about 0.5 electron per pulse coulomb interactions will have a negative effect on the beam quality, in terms of trajectory displacement, beam energy spread and electron pulse length.[5,6] A comprehensive overview of sources for UEM can be found in Zhang et al.[7]. In this thesis we focus on pulsed electron sources for UEM that rely on blanking a continuous electron beam.

The requirement that every electron pulse contains less than 1 electron requires integration of the signal over many electron pulses. Thus, only reversible processes can be studied in a stroboscopic fashion. In order to resolve temporal dynamics at time scales faster than the response time of electronics and detectors a technique called pump-probe is used: An ultrashort laser pulse will induce excitations and dynamics ('pump') in the sample and an ultrashort electron pulse arriving at a variable delay will probe the dynamics. Hence, detectors with a low temporal resolution can be used enabling the use of potentially all detectors in an EM and thus opening up the investigation of several contrast mechanisms for time resolved microscopy.

1.1 Ultrafast Electron microscopes

Stroboscopic imaging in a SEM started in the 1960's with the work of Plows and Nixon. They created 10 ns electron pulses by chopping a continuous beam with a deflector, synchronized to a voltage signal applied to a microcircuit. Voltage contrast was then used to stroboscopically image the voltage dynamics in the microcircuit.[8] Voltage contrast used the fact that the secondary electron yield of a surface is altered when a voltage is applied to the surface.

In the 1980's, beam blankers were further improved to create electron pulse lengths in the sub-picosecond domain, starting with Ura *et al.*, who demonstrated electron pulse lengths of 200 fs. They used an RF cavity and a buncher, which uses electromagnetic fields to compress electron pulses.[9,10] Fehr *et al.* created 100 fs electron pulses by employing a coaxial transmission line, with holes in the outer electrode and without dielectric material between the inner and outer electrode.[11] The short electron pulses created with such blankers were employed to resolve in time and space the voltage response of integrated circuits.[12] However, all these microscopes did not achieve the sub-10 nm resolution nowadays achieved with commercial SEMs.

Mourou and Williamson used a photocathode triggered with a laser pulse to create electron pulses for diffraction to observe melting Al films. However, their temporal resolution of 20 ps or larger was not sufficient to resolve the melting or recrystallization dynamics.[13,14] Photocathodes have a flat and large emission area, which may be beneficial as laser pulses cannot be focused to spot size smaller than about 1 μm , but their brightness is limited by space charge, as described by Child's law, to values of about $10^6 \text{ A}/(\text{m}^2\text{sr}\cdot\text{V})$ assuming a static extraction field.

Hommelhoff and others started to use sharp tips as photoelectron sources.[15,16] The physics of photoelectron emission is complicated. Essentially there are three emission mechanisms:

optical field emission, where electrons are accelerated out of the tip due to the laser field, multiphoton emission, and linear photoemission where the photon wavelength matches the work function (reduced due to thermal energy of the electrons and the Schottky effect). Both the optical field emission and multiphoton emission processes are non-linearly dependent on the (tip enhanced) laser intensity, so the thermal load on the tip will be larger, which can be a disadvantage. Secondly, the energy spread of the electrons emitted by such a non-linear source tends to increase [17,18], which is undesired for high quality EM as it reduces spatial, temporal resolution and, in EELS, energy resolution. Hence, for UEM it is preferred to use linear photoemission which can be accomplished with a Schottky source by reducing the temperature of the tip to prevent background emission of electrons. Ehberger showed that sharp tungsten tips illuminated with laser pulses have transversal coherences comparable to Schottky tips [19], hence the reduced brightness is also comparable for laser triggered and DC Schottky emitters as coherence and brightness are directly related.

The group of Zewail illuminated a Schottky source in a SEM with femtosecond laser pulses to create electron pulses with pulse lengths of about 300 fs.[20] Exact brightness and energy spread values have not been measured for this ultrafast-SEM (USEM). Cook estimated the brightness of this source as $10^8 \text{ A}/(\text{m}^2\text{-sr}\cdot\text{V})$. [21] Feist *et al.* also created femtosecond laser pulses, in a TEM, by illuminating a Schottky source operating at reduced temperatures to prevent DC emission of electrons. The peak brightness of that source in pulsed mode has been measured to be in the $10^8 \text{ A}/(\text{m}^2\text{-sr}\cdot\text{V})$ range with an energy spread of 0.6 eV, with no increase in energy spread measured when switching between both modes of operation.[22]

1.2 Applications of Ultrafast electron microscopy

The previous paragraph already described several applications of UEM. In ultrafast TEMs several papers have been published demonstrating that an electron can pick or lose a quantised photon energy when interacting with optical near fields, an effect called photon-induced near-field electron microscopy (PINEM). Zewail demonstrated this around silver nano-triangles and showed that PINEM can be used to measure the strength of the near fields around photonic structures, at high spatial resolution.[23,24] Feist *et al.* reproduced a similar effect around a sharp gold tip.[25] They demonstrated that this effect is essentially similar to a Ramsey like operation.[26] Also, they envisioned that with such a system a train of attosecond electron pulses can be created with temporal spacing given by the temporal period of the laser field.[26] Recently another application has been demonstrated where electron vortex pulses have been created with a plasmonic structure.[27]

Ultrafast melting of Al with high temporal resolution, in the picosecond range, has been measured in diffraction by Williamson *et al.* [14], and later significantly improved by Siwick *et al.*[28] Ultrafast electron diffraction (UED) has also been used to study and understand the dynamics of more complex systems like the transition from insulating to metallic phase in Vanadium oxide. [29] Another application of UEM is the study of phonon dynamics in materials at the nanoscale, like in thin graphite films by for example Park *et al.* [30] and Feist *et al.*[31] The pulsed electron beam in a STEM illuminates the sample with a spot size of about 10-30 nm and from the diffraction pattern the displacement of atoms is determined and hence the propagation of phonons, induced by the laser pulse, can be imaged in time and space.

Another application is time-resolved Lorentz microscopy, the temperature of a magnetic material is temporally raised above the Curie temperature due to a laser pulse and the local magnetization can be resolved by the deflection of the electron beam.[4] To summarize, UED is already commonly used for structural dynamics/material science studies. Also, there are operational ultrafast TEM's and they demonstrated high spatial and temporal resolution in transmission experiments.

Apart from ultrafast TEM's and UED setups, also an ultrafast SEM has been developed, as mentioned in the previous section, with electron pulses shorter than 700 fs.[20,32] The advantage of an SEM is that thick, non-electron transparent, bulk samples can be investigated. Also a SEM can perform backscatter diffraction and a high degree of surface contrast is possible in secondary electron imaging mode. The latter can potentially be used in an USEM to resolve carrier dynamics in semiconductor materials like GaAs in space and time.[33] Surface acoustic waves can also be resolved in space and time with an USEM.[34] A SEM can also be equipped with detectors to detect cathodoluminescence, i.e. light generated by the excitation of a material with an electron beam, see Abajo and references therein.[35] Still, so far no experiments have been demonstrated in an ultrafast SEM showing time-resolved features with resolution below the diffraction limit of visible light, about 250 nm, and at time scales of picoseconds or smaller.

1.3 Challenges in ultrafast SEM

An electron source for an USEM and UEM in general has to fulfil several requirements: a high reduced brightness, low energy spread, and low amount of jitter between the laser and electron pulse. The latter is important as it is convoluted with the electron pulse length to determine the temporal resolution in the pump-probe experiment. A last important requirement is that it should be easy to switch between pulsed and DC mode. The reason is that it is first necessary to find a region of interest where the ultrafast experiment or measurement is to be performed. In pulsed mode the current will be low, so it will be convenient to use a continuous beam for this purpose. Photo-emitters seem to require up to 1 hour to change from continuous beam (DC), to pulsed mode of operation.[22]

Beam blankers can rapidly switch between pulsed and DC mode of operation. For this reason, there is increased interest in beam blankers in the field of UEM. Microwave cavities have been developed that show a conservation of brightness and no or only a small increase in energy spread.[36,37] Experimentally it has already been demonstrated that electron pulses of 1.1 – 1.3 ps can be created with microwave cavities without degradation in beam quality in the electron pulse. In these experiments, the electron pulse length was estimated by measuring the reduction in current after the blanking aperture.[38] Instead of RF fields, research is also done to use optical and THz fields.[39,40] Both these methods rely on relatively large systems, microwave cavities or high energy laser pulses and parabolic mirrors in the beam line like in the work of Ehberger *et al.* [39] In this thesis the aim is to develop a more compact beam blander so it can be easily integrated in the beam line of a commercial EM and allow the operator relatively fast switching between DC and ultrafast imaging operation mode.

To compare electron pulses created with sharp photo tips to pulses created with beam blankers, it is relevant to consider the average current in the probe beam at the sample, as the current determines the signal to noise ratio. We assume the reduced brightness of the photoemitter, during an electron pulse, to be equal to that of a Schottky DC source and denote this with B_r . The time averaged current in the probe of a photoemitter is then equal to:

$$\begin{aligned} I_{p,avg} &= 2f_{rep}\tau I_{pulse} \\ I_{p,avg} &= \frac{1}{2}\tau f_{rep} B_r \pi^2 d_p^2 \alpha_p^2 \phi \end{aligned} \quad (0.2)$$

where f_{rep} is the repetition rate of the electron pulse/laser pulse, τ the FW50 electron pulse length, I_{pulse} is the current during an electron pulse, i.e. the charge per pulse divided by the pulse length, d_p is the probe size, a the half opening angle and ϕ the beam energy. The charge per pulse should be less than 0.5 to prevent degradation in beam brightness and energy spread, assuming sub-1 picosecond electron pulses are to be produced.[6]

For a chopped electron beam the average current in the pulsed probe beam is equal to:

$$\begin{aligned} I_{b,avg} &= 2f_{rep}\tau I_{DC} \\ I_{b,avg} &= \frac{1}{2} B_r \tau f_{rep} \pi^2 d_b^2 \alpha_b^2 \phi \end{aligned} \quad (0.3)$$

where I_{DC} is the current before the blanking aperture, i.e. the probe current in DC mode of operation. The average current $I_{b,avg}$ in a chopped pulse has a factor 2 in it because we use a FW50 value for the pulse length, ie in τ only 50% of the electrons are present. Hence both equations for the current in a probe are equivalent, i.e. an ultrafast blanker can achieve the same performance as a photoemitter. This is under the assumption that the peak reduced brightness and the reduced brightness of a Schottky and photoemitter source are equivalent. As mentioned above, this was indeed observed by Feist *et al.* and indirectly confirmed by measuring the amount of current in a coherent beam created with a photoemitter by Ehberger.[19,22]

One problem of ultrafast electron microscopy is that it is not easy to implement in electron microscopes our aim is to improve that with an ultrafast beam blanker which can be inserted in the beam line like detectors and sample holders. Secondly we explore the possibilities and applications to perform time resolved experiments in a scanning electron microscope.

1.4 Outline of the thesis

In Chapter 2 we discuss the integration of a femtosecond laser in the SEM, and describe the dispersion compensation of the laser pulse. Electron pulses are generated using a standard commercial FEI blanker and we use a home-built streak camera to characterize the electron pulse length. A proof of principle pump-probe measurement is also discussed. Basically the setup described in the Chapter 2 is a platform for time-resolved SEM.

Our approach to create femtosecond electron pulses is presented in Chapter 3. The idea is essentially to combine an electrostatic beam blanker with a photoconductive switch. We explain why in our design the beam blanker is integrated with the photoconductive switch and why the device has to have submicron dimensions. The electron pulse length and spatial resolution are estimated by back-of-the-envelope calculations.

The ultrafast beam blanker is further analysed using numerical calculations, which allows discussion of the electron beam quality and electron pulse length. This is presented in chapter 4. This chapter shows that the length of the electron pulse is close to what is to be expected from analytical calculations. Also the energy spread of the beam is numerically calculated and estimated with respect to the beam energy.

Chapter 5 describes the fabrication of the blanker with MEMS technology and the integration with the photoconductive switch in detail. A design and alignment of a blanker stick to get the UFB in the beamline of a commercial SEM is described too. Performance characterisation of the ultrafast beam blanker is also discussed.

The last chapter of this thesis, Chapter 6, describes several required steps for valorisation of our technique to create ultrafast electron pulses. We also discuss the incorporation of the system in a TEM and the effect on beam brightness and energy spread when operating with typical TEM beams in the 100 kV to 300 kV range.

Bibliography

- [1] A.H. V. van Veen, C.W. Hagen, J.E. Barth, P. Kruit, Reduced brightness of the ZrO/W Schottky electron emitter, *J. Vac. Sci. Technol. B Microelectron. Nanom. Struct.* 19 (2001) 2038. doi:10.1116/1.1409390.
- [2] B. Cook, T. Verduin, C.W. Hagen, P. Kruit, Brightness limitations of cold field emitters caused by Coulomb interactions, *J. Vac. Sci. Technol. B Microelectron. Nanom. Struct.* 28 (2010) C6C74. doi:10.1116/1.3502642.
- [3] A.H. Zewail, Four-dimensional electron microscopy., *Science.* 328 (2010) 187-93. doi:10.1126/science.1166135.
- [4] T. Eggebrecht, M. Müller, J.G. Gatzmann, N. Rubiano Da Silva, A. Feist, U. Martens, H. Ulrichs, M. Münzenberg, C. Ropers, S. Schöfer, Light-Induced Metastable Magnetic Texture Uncovered by in situ Lorentz Microscopy, *Phys. Rev. Lett.* 118 (2017) 1-7. doi:10.1103/PhysRevLett.118.097203.
- [5] A. Gahlmann, S. Tae Park, A.H. Zewail, Ultrashort electron pulses for diffraction, crystallography and microscopy: theoretical and experimental resolutions., *Phys. Chem. Chem. Phys.* 10 (2008) 2894-909. doi:10.1039/b802136h.
- [6] B. Cook, P. Kruit, Coulomb interactions in sharp tip pulsed photo field emitters, *Appl. Phys. Lett.* 109 (2016) 151901. doi:10.1063/1.4963783.
- [7] L. Zhang, J.P. Hoogenboom, B. Cook, P. Kruit, Photoemission sources and beam blankers for ultrafast electron microscopy, *Struct. Dyn.* 6 (2019). doi:10.1063/1.5117058.

- [8] G.S. Plows, W.C. Nixon, Stroboscopic scanning electron microscopy, *J. Phys. E.* 1 (1968) 595–600. doi:10.1088/0022-3735/1/6/302.
- [9] K. Ura, H. Fujioka, T. Hosokawa, Picosecond Pulse Stroboscopic Scanning Electron Microscope, *J. Electron Microsc. (Tokyo)*. 27 (1978) 247–252.
- [10] T. Hosokawa, H. Fujioka, K. Ura, Generation and measurement of subpicosecond electron beam pulses., *Rev. Sci. Instrum.* 49 (1978) 624. doi:10.1063/1.1135464.
- [11] J. Fehr, W. Reiners, L.J. Balk, E. Kubalek, D. Köther, I. Wolff, A 100-FEMTOSECOND ELECTRON BEAM BLANKING SYSTEM, *Microelectron. Eng.* 12 (1990) 221–226.
- [12] D. Winkler, R. Schmitt, M. Brunner, B. Lischke, Flexible picosecond probing of integrated circuits with chopped electron beams, *IBM J. Res. Dev.* 34 (1990) 189–203. doi:10.1147/rd.342.0189.
- [13] G. Mourou, S. Williamson, Picosecond electron diffraction, *Appl. Phys. Lett.* 41 (1982) 44–45. doi:10.1063/1.93316.
- [14] S. Williamson, G. Mourou, J.C.M. Li, Time-resolved laser-induced phase transformation in aluminum, *Phys. Rev. Lett.* 52 (1984) 2364–2367. doi:10.1103/PhysRevLett.52.2364.
- [15] P. Hommelhoff, C. Kealhofer, M.A. Kasevich, Ultrafast Electron Pulses from a Tungsten Tip Triggered by Low-Power Femtosecond Laser Pulses, *Phys. Rev. Lett.* 97 (2006) 247402. doi:10.1103/PhysRevLett.97.247402.
- [16] P. Hommelhoff, Y. Sortais, A. Aghajani-Talesh, M. a. Kasevich, Field Emission Tip as a Nanometer Source of Free Electron Femtosecond Pulses, *Phys. Rev. Lett.* 96 (2006) 077401. doi:10.1103/PhysRevLett.96.077401.
- [17] G. Herink, D.R. Solli, M. Gulde, C. Ropers, Field-driven photoemission from nanostructures quenches the quiver motion., *Nature*. 483 (2012) 190–3. doi:10.1038/nature10878.
- [18] M. Krüger, M. Schenk, P. Hommelhoff, Attosecond control of electrons emitted from a nanoscale metal tip., *Nature*. 475 (2011) 78–81. doi:10.1038/nature10196.
- [19] D. Ehberger, J. Hammer, M. Eisele, M. Krüger, J. Noe, A. Högele, P. Hommelhoff, Highly Coherent Electron Beam from a Laser-Triggered Tungsten Needle Tip, *Phys. Rev. Lett.* 114 (2015) 1–5. doi:10.1103/PhysRevLett.114.227601.
- [20] D.-S. Yang, O.F. Mohammed, A.H. Zewail, Scanning ultrafast electron microscopy., *Proc. Natl. Acad. Sci. U. S. A.* 107 (2010) 14993–8. doi:10.1073/pnas.1009321107.
- [21] B. Cook, *Brightness Limitations in sources for static & ultra-fast high resolution electron microscopy*, Delft University of Technology, 2013.
- [22] A. Feist, N. Bach, N. Rubiano da Silva, T. Danz, M. Möller, K.E. Priebe, T. Domröse, J.G. Gatzmann, S. Rost, J. Schauss, S. Strauch, R. Bormann, M. Sivilis, S. Schäfer, C. Ropers, Ultrafast transmission electron microscopy using a laser-driven field emitter: Femtosecond resolution with a high coherence electron beam, *Ultramicroscopy*. 176 (2017) 63–73. doi:10.1016/j.ultramic.2016.12.005.
- [23] B. Barwick, D.J. Flannigan, A.H. Zewail, Photon-induced near-field electron microscopy., *Nature*. 462 (2009) 902–6. doi:10.1038/nature08662.

- [24] S.T. Park, M. Lin, A.H. Zewail, Photon-induced near-field electron microscopy (PINEM): theoretical and experimental, *New J. Phys.* 12 (2010) 123028. doi:10.1088/1367-2630/12/12/123028.
- [25] A. Feist, K.E. Echternkamp, J. Schauss, S. V. Yalunin, S. Schäfer, C. Ropers, Quantum coherent optical phase modulation in an ultrafast transmission electron microscope, *Nature*. 521 (2015) 200–203. doi:10.1038/nature14463.
- [26] K.E. Echternkamp, A. Feist, S. Schäfer, C. Ropers, Ramsey-type phase control of free-electron beams, *Nat. Phys.* 12 (2016) 1000–1004. doi:10.1038/nphys3844.
- [27] G.M. Vanacore, G. Berruto, I. Madan, E. Pomarico, P. Biagioni, R.J. Lamb, D. McGrouther, O. Reinhardt, I. Kaminer, B. Barwick, H. Larocque, V. Grillo, E. Karimi, F.J. García de Abajo, F. Carbone, Ultrafast generation and control of an electron vortex beam via chiral plasmonic near fields, *Nat. Mater.* 18 (2019) 573–579. doi:10.1038/s41563-019-0336-1.
- [28] B.J. Siwick, J.R. Dwyer, R.E. Jordan, R.J.D. Miller, An atomic-level view of melting using femtosecond electron diffraction., *Science*. 302 (2003) 1382–5. doi:10.1126/science.1090052.
- [29] V.R. Morrison, R.P. Chatelain, K.L. Tiwari, A. Hendaoui, A. Bruhács, M. Chaker, B.J. Siwick, A photoinduced metal-like phase of monoclinic VO₂ revealed by ultrafast electron diffraction, *Science* (80-.). 346 (2014) 445–448.
- [30] H.S. Park, J.S. Baskin, B. Barwick, O.-H. Kwon, A.H. Zewail, 4D ultrafast electron microscopy: Imaging of atomic motions, acoustic resonances, and moiré fringe dynamics, *Ultramicroscopy*. 110 (2009) 7–19. doi:10.1016/j.ultramic.2009.08.005.
- [31] A. Feist, W. Liang, C. Ropers, Nanoscale diffractive probing of strain dynamics in ultrafast transmission electron microscopy in ultrafast transmission electron microscopy, 014302 (2018). doi:10.1063/1.5009822.
- [32] O.F. Mohammed, D.-S. Yang, S.K. Pal, A.H. Zewail, 4D scanning ultrafast electron microscopy: visualization of materials surface dynamics., *J. Am. Chem. Soc.* 133 (2011) 7708–11. doi:10.1021/ja2031322.
- [33] J. Cho, T.Y. Hwang, A.H. Zewail, Visualization of carrier dynamics in p(n)-type GaAs by scanning ultrafast electron microscopy., *Proc. Natl. Acad. Sci. U. S. A.* 111 (2014). doi:10.1073/pnas.1400138111.
- [34] E. Najafi, B. Liao, T. Scarborough, A. Zewail, Imaging Surface Acoustic Wave Dynamics in Semiconducting Polymers by Scanning Ultrafast Electron Microscopy, *Ultramicroscopy*. (2017). doi:10.1016/j.ultramic.2017.08.011.
- [35] F.J. García de Abajo, Optical excitations in electron microscopy, *Rev. Mod. Phys.* 82 (2010) 209–275. doi:10.1103/RevModPhys.82.209.
- [36] A. Lassise, P.H.A. Mutsaers, O.J. Luiten, Compact, low power radio frequency cavity for femtosecond electron microscopy., *Rev. Sci. Instrum.* 83 (2012) 043705. doi:10.1063/1.3703314.
- [37] J.F.M. van Rens, W. Verhoeven, J.G.H. Franssen, A.C. Lassise, X.F.D. Stragier, E.R. Kieft, P.H.A. Mutsaers, O.J. Luiten, Theory and particle tracking simulations of a resonant

radiofrequency deflection cavity in TM 110 mode for ultrafast electron microscopy, *Ultramicroscopy*. 184 (2018) 77–89. doi:10.1016/j.ultramic.2017.10.004.

- [38] W. Verhoeven, J.F.M. van Rens, E.R. Kieft, P.H.A. Mutsaers, O.J. Luiten, High quality ultrafast transmission electron microscopy using resonant microwave cavities, *Ultramicroscopy*. 188 (2018) 85–89. doi:10.1016/j.ultramic.2018.03.012.
- [39] A.C. Kealhofer, W. Schneider, D. Ehberger, A. Ryabov, P. Baum, F. Krausz, All-optical control and metrology of electron pulses, *Science* (80-.). 352 (2016) 429–433.
- [40] A. Ryabov, P. Baum, Electron microscopy of electromagnetic waveforms, *Science* (80-.). 2182 (2016) 2179–2182.

2 An experimental platform for time-resolved, high spatial resolution integrated light and electron microscopy

2.1 Introduction

In nanotechnology, the functional building blocks typically have one or more dimensions that are far below the diffraction limit of light. These nanoscale dimensions can give rise to properties differing considerably from that of bulk materials, due to statistical and quantum mechanical effects. Also, nanostructures are highly relevant because they can strongly interact with light and enhance several optical processes. Examples are decay rate enhancement and directionality control of fluorescent emitters¹, metamaterials², optoelectronics^{3,4}, etc.⁵ For nanostructured solar cells both the interaction with light and the diffusion and dynamics of charge carriers is important for their performance and efficiency.⁶ Other examples are non-linear processes like tip enhanced Raman scattering⁷, second and higher harmonic light generation⁸ and multiphoton and optical field emission of electrons⁹. The latter application is also relevant as a source for ultrafast electron microscopes (UEM). The non-linear optical properties leading to photoemission of electrons can also be used for applications such as carrier-envelope-phase sensitive detectors as demonstrated by Putnam *et al.*¹⁰ or other optoelectronic devices like for example nanoscale vacuum-tube diodes.¹¹

The performance of such nanoscale devices can depend critically on the exact dimensions, composition and morphology of the nanostructure. Also, due to the large surface-to-volume ratios involved, surface or interface states and (epitaxial) defects may dominate the observed behaviour. Thus, for characterization and study of nanodevices, microscopy tools are required to assess optical performance and charge carrier dynamics at high spatial, sub-wavelength, resolution. Also a direct correlation between the optical response, carrier concentration and transport, and the sample morphology and composition is required at a high spatial resolution. Considering the length scales involved, this needs techniques using (focused) beams of electrons. In the following two sections we briefly describe two EM techniques for characterizing nanodevices both spatially and temporally, namely time-resolved cathodoluminescence and photon pump electron probe. After this we will discuss the outline of the remainder of this chapter.

2.1.1 Cathodoluminescence microscopy

Cathodoluminescence microscopy (CL) is now a well-established method to characterize optical properties of nanophotonic structures at deep sub-wavelength resolution. By exciting nanophotonic structures with a focused electron beam, light is emitted due to coherent processes like transition radiation and surface plasmon polaritons (SPPs), and incoherent processes like carrier recombination and excitation and subsequent decay to the ground state. These processes are extensively discussed by Abajo and references therein.¹²

CL microscopy is usually performed by inserting a parabolic mirror in between the final lens of the SEM and sample. A hole is made in the parabolic mirror such that the electron beam can pass through and excite the sample. The CL is collected by the PM and directed to, for example,

photodetectors and spectrometers. This method has been experimentally demonstrated by Yamamoto *et al.* and others.¹³⁻¹⁶

An alternative method for CL detection is the use of a normal inverted microscope in a SEM vacuum chamber. An advantage is that the numerical aperture (NA) and light collection efficiency can be higher especially when vacuum compatible immersion oils are used.¹⁷ In our group we have developed an inverted optical microscope with above the sample a commercial SEM, called scanning electron combined optical microscope (SECOM). For a detailed description of the SECOM platform we refer to the work of Zonneville *et al.*¹⁸ Another advantage of the SECOM system is that it enables to perform fluorescence microscopy directly correlated with electron microscopy, i.e. simultaneous correlative light electron microscopy, CLEM.^{19,20}

Narvaez *et al.* showed that the SECOM system allows to excite SPPs in Au nanostructures, like Au nanowires and triangles, on transparent substrates, employing either confocal filtering or low electron beam energies to suppress background CL from the ITO/glass substrate.^{17,21}

Cathodoluminescence imaging is a good technique to measure the modes and emission angles of nanophotonic structures and the spatial resolution of CL is high, in the order of tens of nanometers.¹⁵ In some cases also the radiative part of the local density of optical states (LDOS) can be inferred from CL measurements.¹⁴ However, a pulsed electron beam is required to measure the LDOS directly through measurement of the decay rate of an emitter. Characterizing the non-linear response of metallic nanostructures and particles will be difficult or not possible with an electron beam, as the excitation efficiency of CL is low, about 1 photon per 1000 electrons in case of direct excitation of plasmonic systems.¹⁴

Pulsing the electron beam allows for time-resolved CL, for example Merano *et al.* analyzed carrier dynamics in InGaAs/AlGaAs pyramidal quantum structures with a laser triggered source and measuring the CL with a streak camera.²² For such applications it could be attractive to use standard beam blankers, as it is a simple and standard technology and beam blankers easily achieve sub-nanosecond pulse lengths. Typical cathodoluminescence and excited state lifetimes are in the nanosecond and longer time range, hence electron pulses shorter than 1 nanosecond are sufficient.²³⁻²⁵

2.1.2 Laser-pump electron-probe microscopy

For applications where (sub-)picosecond temporal resolution is required, laser pump and electron probe microscopy, or (ultra)fast EM, has evolved in the past decade as a microscopy technique with high temporal and spatial resolution.²⁶ Ultrafast EM allows to induce non-linear optical processes and and/or excite electrons to the conduction band with a femtosecond laser pulse and study the resulting dynamics with the electron probe.²⁷ Electron pulses are typically generated by triggering the electron source with an ultrafast laser pulse.²⁶ The sample is also excited with a laser pulse and subsequently probed with the electron pulse where, by varying the time delay of the probe with respect to the pump pulse, the temporal dynamics is resolved.

In an SEM, the combination of a pulsed electron and a pulsed laser beam opens up the capability to resolve carrier dynamics on surfaces in space and time, as shown by the groups of Zewail and Mohammed.^{28,29} The laser pulse is used to excite electrons from the valence band to the conduction band. A subsequent electron pulse will generate secondary electrons and the escape probability of these low energy electrons will change when there are electrons in the conduction band.³⁰ Hence, by employing a pump-probe measurement with the laser as a pump and the electron pulse as a probe the dynamics of excited electrons can be resolved in both space and time.

In the existing schemes the laser is focused externally with a lens and coupled in via a vacuum window, hence the spot size is typically in the order of 30 μm .²⁷ The large laser spot size limits the resolution in excitation of a (nanostructured) sample, which is now at least a factor 10^3 worse than the resolution of the probing electron spot. For this reason, we coupled the femtosecond laser in via the SECOM platform, where a high NA objective lens is employed underneath the sample to focus the laser pulse to a spot smaller than 1 μm , this has the advantage that all BSE and ETD detectors of a SEM are still available. This can facilitate the excitation of the sample at specific points which may be an advantage for the study of carrier dynamics in micro- and nanofabricated solid state devices. In addition, high-k vectors provided by a tight focusing with a high-NA lens, may enable efficient coupling between the nanostructure and laser pulse, for example to launch surface plasmons.

2.1.3 Outline

In section 2.2 we will describe the optical setup to focus the laser on the sample and we characterize the optical resolution and laser pulse length. In section 2.3 we show the creation and characterization of sub-nanosecond electron pulses with a standard commercial blanker. In section 2.4 we show a proof of principle measurement of a pump probe measurement on a thin MoS_2 layer.

2.2 Femtosecond laser excitation in a SEM vacuum chamber

In this paragraph we give a detailed description of the experimental setup, a schematic is shown in Figure 2.1. We also present measurements of the laser pulse length. The laser pulses are derived from a Coherent Vitara-T Ti:Sapph femtosecond laser, the pulse repetition rate is equal to 95 MHz. The bandwidth of the laser can be varied between 30 nm and about 125 nm, with a tunable central wavelength of 800 nm. A telescope is used to expand the beam, an $f = +40$ mm achromatic doublet (Thorlabs, AC254-040-ML) is combined with an $f = +150$ mm (Thorlabs, LA1433-A) plano convex lens, which gives a magnification of 3.75.

A high-NA objective lens is required to tightly focus the laser pulse. Such an objective lens consists of a stack of lenses to compensate for aberrations to create a diffraction limited point-spread function. The objective lens is in the sample chamber of the SEM and a vacuum window is used to couple light in or out of the vacuum chamber. Hence, the laser pulse has to propagate through centimetres of glass, which has a non-zero group velocity dispersion (GVD). Thus the ultrashort laser pulse will be broadened before reaching the sample. This pulse broadening is pre-compensated by mirrors introducing GVD with opposite sign, see Figure 2.1. The group delay dispersion per reflection in the mirror is -175 fs^2 .

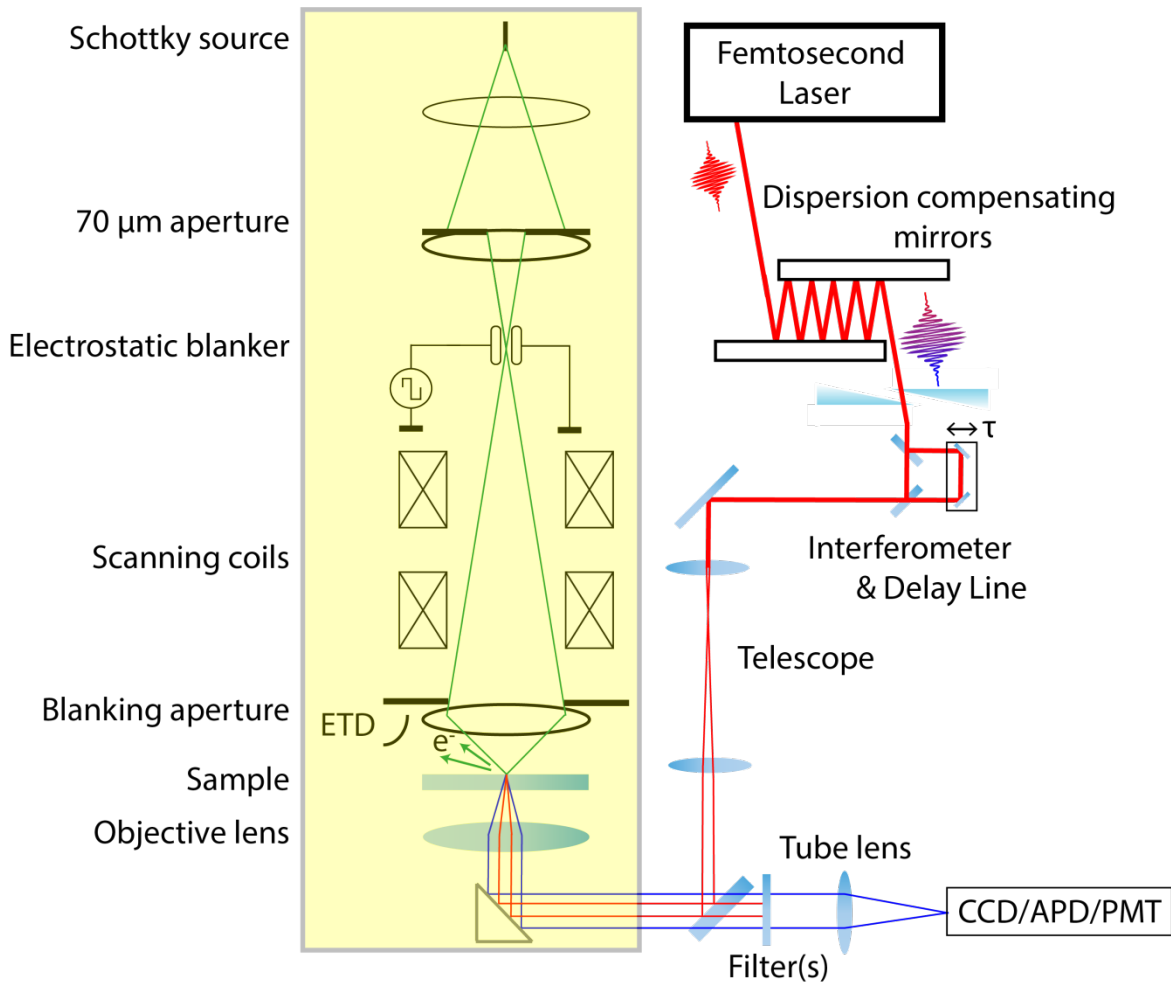


Figure 2.1: Schematic of the setup. The sample is exposed to a (pulsed) focused electron beam from above and illuminated by a laser from below which is focused to a small spot by the objective lens. The electron pulses are generated with an electrostatic blanker. A square wave from a pulse generator is applied over the blanker plates, resulting in a sweeping of the electron beam over the blanking aperture and by this chopping process electron pulses are created below the blanking aperture. The laser pulses from a coherent femtosecond Ti:Sapph laser will undergo anomalous dispersion at each bounce in the dispersion compensation mirrors, which is further fine-tuned by glass wedges, to pre-compensate the normal dispersion of the objective lens and other optical components in the beam path. A telescope with a magnification of 3.75 is used to fill up the back focal plane of the objective lens. Light emitted from the sample plane is collected by the same objective lens and focused with a tube lens on the detector, which can be an avalanche photodiode, a PMT or a CCD camera for alignment purposes.

The laser pulse length is measured with a second order autocorrelation, by means of a 100 μm thick barium borate (BBO) nonlinear crystal in the focal plane and an interferometer with a variable delay line.³¹ The full width at half maximum (FWHM) of a measured second order autocorrelation curve gives an indication of the laser pulse length.³² By fine tuning the glass wedges and adjusting the amount of bounces at the mirror, the laser pulse length is minimized. We found that the vacuum window and 1.25 NA Nikon CFI Apo Lambda S 40XWI objective lens have a total group delay dispersion of about 5600 fs². A Thorlabs DDSM100 direct drive stage is used for the delay line.

The second order autocorrelation trace in Figure 2.2 shows that the laser pulse length is about 15 fs FWHM in the focal plane using the Nikon 1.25 NA 40x water immersion lens. Hence our system can efficiently induce non-linear optical processes.

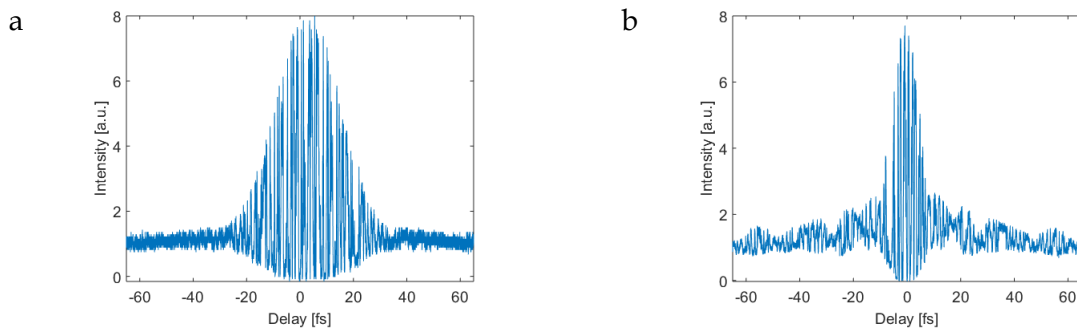


Figure 2.2: Second order autocorrelation measured with a BBO crystal in the focal plane of the objective lens inside the SECOM platform with a laser bandwidth of (a) 40 nm and (b) 125 nm. The delay is varied with a stepper motor and the SHG as function of delay is detected with a PMT, see Figure 2.1. The ratio of the peak to background is approximately 1:8 as expected.³² The bandwidth of 125 nm corresponds to a pulse length of about 15 fs. The FWHM of the trace in (b) indicates a pulse length of about 15 fs. A total of 32 bounces in the dispersion compensating mirrors are used.

In Figure 2.3 we show a measurement of the laser spot size using the two-photon excited signal from an InP nanowire. The spot size of the laser depends on the laser beam diameter before the objective lens and on the beam profile of the laser. The laser beam is not expanded far enough to fill up the back focal plane of the objective lens completely leading to a measured laser spot size of about 620 nm.

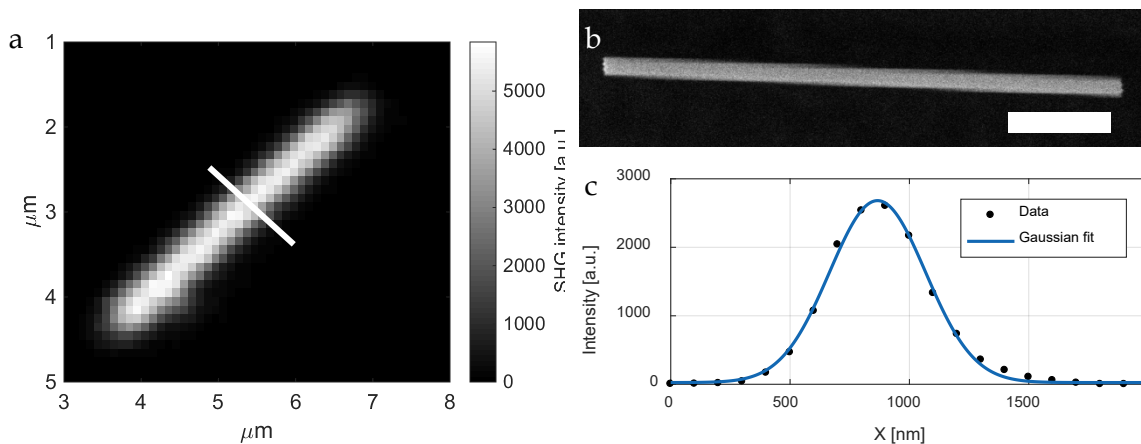


Figure 2.3: (a) Two-photon excitation image of an InP nanowire measured with an APD detector and an optical bandpass filter centered at 400 nm with a passband equal to 40 nm. The image is acquired by scanning the nanowire through the laser spot. (b) SEM image of the same InP NW with a diameter of 173 nm, the scale bar is 1 μm . (c) Cross section of the two-photon excitation signal over the white bar in image (a). The black dots are the data points and the blue line is a Gaussian fit. The FWHM of the fit is equal to 474 nm, corresponding to a laser spot size of 620 nm in the focal plane (where we take into account the dimensions of the InP nanowire and nonlinearity of the process).

2.3 Generation and characterization of a pulsed electron beam

In the previous paragraph we showed that the femtosecond laser is coupled in, the electron beam can be aligned with respect to the laser beam by shifting the electron beam to the spot where the laser beam excites the nanowire. This gives the capability to optically excite a sample

and use the electron pulse to probe the induced dynamics at a high spatial resolution. In order to also retrieve time-dynamic processes the electron beam has to be pulsed, so that the dynamics can be stroboscopically measured using pump-probe techniques.

Electron pulses with lengths in the low picoseconds or femtosecond time range are technically complicated to create, whether it is by illumination of the tip with femtosecond laser pulses or with gigahertz RF cavities.^{33,34} Electron pulses with lengths in the (sub) nanosecond range can be created with standard electrostatic beam blankers, which is a less complicated technology compared to RF cavities or laser illuminated tips. Secondly, fast switching between DC and pulsed mode is difficult with a laser illuminated tip, but quite straightforward using a beam blanker.

Hence our time-resolved experiments are performed by employing a standard commercial beam blanker from FEI/ThermoFisher: the deflector plates have a separation of 0.3 mm and the length along the electron optical axis is 6 mm. The electron beam is focused between the blanker plates, such that the beam blanker is positioned in a conjugate plane as indicated in Figure 2.1. Thus, the electron beam does not sweep over the sample when it is deflected.³⁵ The blanking aperture is inserted close to the pivot point of the SEM scanning coils as indicated in Figure 2.1. An E-H Research Laboratories 135 pulse generator with an output voltage of +/- 5 V in 50 Ω is connected to the electrostatic beam blanker.

The electron pulse length is measured using a home-built streak camera (see Figure 2.4). The idea is to generate an electric field ramp perpendicular to the propagation direction of the electron pulse, so that the temporal shape of the electron pulse is transferred in a spatial one which in turn can be imaged on a fluorescent material. To achieve a high temporal resolution streak camera the distance between the screen and deflector plate should be large and the electric field strength and rise time should be maximized too.

Due to the design of the SECOM platform we have only limited space: the distance between the pole piece and light optical objective lens is less than 10 mm, preferably even only 5 mm to reduce the aberrations of the final lens of the SEM. Hence, we reduced the gap between the deflector plates of the streak camera to about 0.1 mm, to maximize the deflection field strength. A picture of our streak camera is shown in Figure 2.4b. Also, we do not have access to electronic systems with sub-picosecond jitter and GHz electronics. Nevertheless we have demonstrated temporal resolutions of 36 ps at 4 keV, the temporal resolution is limited by electronic jitter in the pulse generators.³⁶ We apply a 5 V peak-to-peak voltage over the blanker plates, with a rise time of about 0.26 ns/V using the pulse generator (E-H Research Laboratories model 137). A pulse generator with a 10 V peak-to-peak voltage is used for the streak camera. In both the beam blanker and streak camera no 50 Ω termination is used, hence the voltage is doubled at the deflector electrodes, i.e 20 V peak-to-peak at the streak camera and 10 V peak-to-peak at the blanker plates. Electron pulse lengths of about 90 ps are measured in our system as shown in Figure 2.4d. This result is partially limited in length due the electronic jitter between both pulse generators.

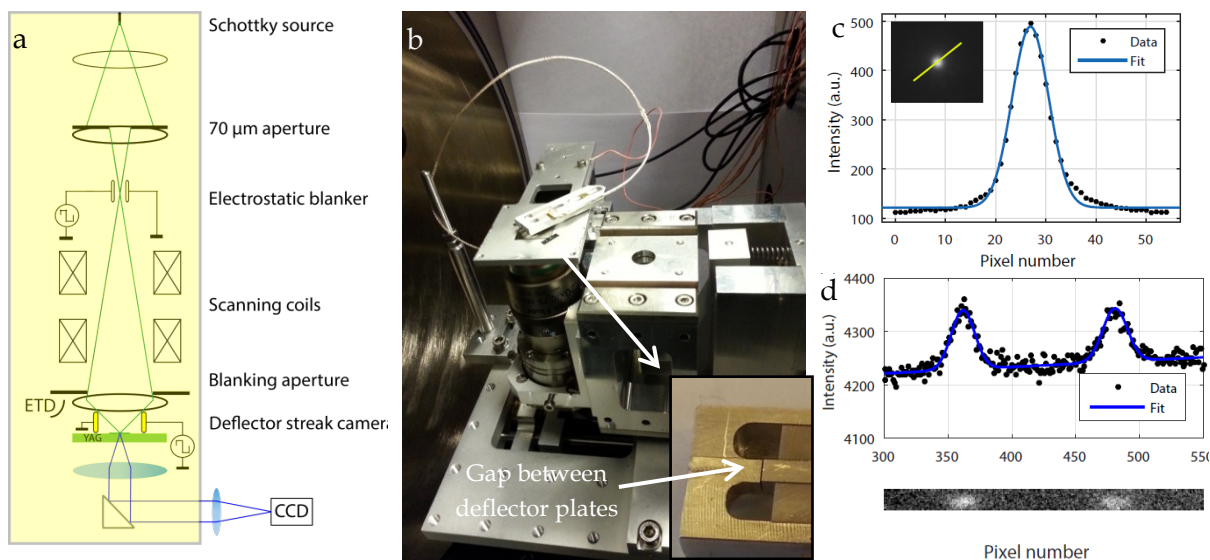


Figure 2.4: (a) Schematic of the experimental setup for measuring pulse duration. Electron pulses are created with an electrostatic blower. The pulse is transferred from the temporal domain to the spatial domain by the deflectors of the streak camera located below the blanking aperture and SEM final lens and is imaged on a YAG screen. (b) The streak camera is mounted directly above the sample holder and optical objective lens, the insert shows the deflector plates of the streak camera, the separation between the deflector plates is 100 μm, the length along the e.o. axis is 2 mm and the distance from the center to the YAG screen is about 3 mm. (c) Photometrics CoolSNAP CCD image of the electron spot on the YAG screen imaged with a 0.75 NA 20x objective lens, the Gaussian fits shows 8.6 pixels FWHM, the pixel size is 4.65 μm, (d) Intensity profile of 2 spots, created with a standard beam blower (< 90 ps pulse length), separated (temporal separation 0.5 ns), the spatial separation is 119.3 pixels. The applied rise time on the streak camera is 0.26 ns/V. (figure adapted from Moerland et al.³⁶)

The electron pulses created with the setup described here have been used successfully for time-resolved CL to probe the LDOS in metal coated dielectric cavities³⁷ and to discriminate fluorescent nanoparticles based on their CL lifetime.³⁸ In this paragraph, however, we will not focus on these applications but instead provide an initial example of the use of the sub-nanosecond electron pulses to perform a pump-probe experiment. When a semiconductor material is illuminated with a laser pulse, the conduction band will be populated with photo-excited electrons. When the material is next exposed to an electron pulse, a difference in SE yield compared to the situation without photo-excitation may be measured. While there may be different, material-dependent mechanisms involved in this change of SE yield, a simple, intuitive picture is that an electron in the conduction band can more easily overcome the work function.^{27,30} Alternatively, the variation in SE yield may come from a mechanical excitation of the sample by the laser beam, e.g., surface acoustic waves have been detected using ultrafast SEM.³⁹

2.4 Proof-of-principle result for pump-probe microscopy.

Previous work by the group of Zewail used sub-picosecond electron pulses for this type of measurements. Here, we provide a proof of principle for this kind of experiments with the setup described in this chapter, using sub-nanosecond electron pulses. In a first approximation, neglecting Coulomb forces, the diffusion of photo-excited charge carriers is described by Fick's law. The diffusion constant D relates the concentration of carriers to the net flux of carriers:

$$J = -D\nabla n \quad (2.1)$$

The diffusion coefficient is related to the mobility via Einstein's Relation:

$$D = k_b T \mu / e \quad (2.2)$$

where T is the temperature, e the Coulomb charge, μ the mobility and k_b the constant of Boltzmann. This relates to a diffusion length of:

$$L = \sqrt{D\tau} \quad (2.3)$$

where τ denotes the lifetime of the carriers. For example, in a system with a low mobility of $200 \text{ cm}^2\text{V}^{-1}\text{s}^{-1}$, charges will diffuse over a distance of approximately 300 nm in a time span of 200 ps. In principle, we would be able to resolve this in space and time with the 90 ps electron pulses from our beam blanker and the high-NA laser focusing.

In order to measure a combination of temporal and spatial dynamics with 90 ps electron pulse and the femtosecond laser, there are a few more requirements that have to be considered. First, as the measurements have to be conducted in a stroboscopic manner, the carrier lifetime has to be significantly less than the interval between laser pulses. For our laser, the repetition rate is 95 MHz, thus the carrier distribution has to relax in less than 10.5 ns. Second, the current experimental setup can only probe excited state dynamics provided that the lifetime is in the order of 90 ps or longer. Finally, charge carriers need to have a low mobility and be excitable with 800 nm light. Hence, only a limited amount of materials can currently be investigated with our experimental setup. One of these is bulk MoS₂, which we used for a proof of principle experiment shown in Figure 2.5. In this experiment, the electron pulse length is about 0.5 ns.

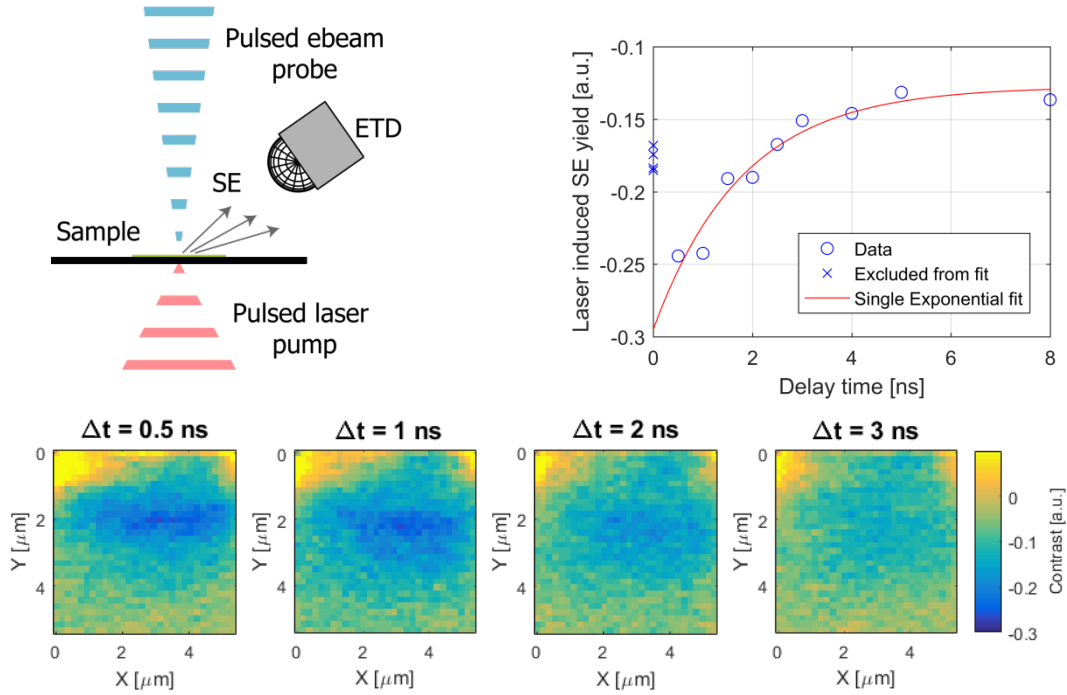


Figure 2.5: (a) A bulk MoS_2 material of about 30 nm thick is deposited on ITO coated glass slide. The MoS_2 flake is illuminated with 800 nm laser pulses from below and with ~ 0.5 ns electron pulses from above, the electron and laser pulses are synchronized. The pulsed electron beam is scanned over the sample, while the position of the laser spot is fixed. The phase-locked SE signal from the ETD is recorded to form an image. (b) Laser induced SE contrast as function of time difference between the electron pulses and laser pulses. The graph contains values that have been obtained from the sequence of images recorded with different time delay, examples of which are shown in panel (c). For each image, the contrast values of the 20 near-lowest pixels, except the lowest pixel value, have been plotted as a function of the delay between the electron and laser pulses. The laser spot is approximately located in the center of the images in (c). Figure adapted from MSc thesis of M.W.H. Garming.⁴⁰

The laser induced contrast, in Figure 2.5, is measured by using a chopper for the laser beam that is operated at a frequency of 940 Hz combined with a lock-in amplifier. The zero delay time between the laser and electron pulse is determined by measuring the laser excited two-photon signal and the electron-excited CL from an InP nanowire, and the arrival times are aligned and shifted with a coaxial delay box. We note that the decay time for the dark contrast obtained from a single-exponential fit to the data in Figure 2.5c corresponds well with the reported photo-luminescence lifetime of bulk MoS_2 . A dark contrast in laser pump electron probe experiments has previously been observed for GaAs and assigned to increased scattering of electrons from sub-surface valence bands by photo-excited conduction band electrons near the surface.³⁰ However, here we cannot confirm or deny this hypothesis and note that these results only serve to illustrate the fact that a delay-time dependent signal from pump-probe experiments can be obtained with the presented set-up. For further details and discussion of these experiments we refer to the MSc thesis of M.W.H. Garming.⁴⁰

2.5 Discussion

The dispersion of the objective lens and the vacuum window in the SECOM platform are pre-compensated by a set of dispersion compensating mirrors similar to for example Muller *et al.*⁴¹ An alternative approach is the use of a pulse shaper as demonstrated by for example Vacano *et al.*⁴², but a (commercial) pulse shaper is expensive compared to a set of dispersion compensating mirrors. With the achieved degree of dispersion compensation, there is a large

gap, about three orders of magnitude, in temporal resolution between the laser and electron pulses respectively. Shorter electron pulses could be created using a photo-emission electron source or using an RF cavity for blanking, but this would come at the expense of the benefits of using electrostatic beam blankers mentioned above, namely facile implementation in existing SEMs and ease of switching between DC and pulsed modes of operation, often pulses in the sub nanosecond range are sufficient and contain more current than femtosecond electron pulses.

We measured the length of pulses created with the electrostatic beam blanker with a simple home-built streak camera. The temporal resolution of the electron pulse and streak camera is partially limited by jitter in the pulse generators, which is some 40 ps as measured with a PicoHarp 300 time correlator. However, the 90 ps electron pulse length is sufficient for many applications. For time-resolved CL, the typical decay times of emitters (both fluorescent and phosphorescent) are in the nanosecond to microsecond time range. The electron pulses can easily be focused to spots smaller than 50 nm, hence the pulsed electron beam can be scanned over a nanophotonic structure and the spatial modulation of the LDOS can be measured quantitatively at spatial resolutions far below the optical diffraction limit, while we have also recently shown lifetime discrimination of emitters using this experimental platform.³⁶⁻³⁸

For photon pump electron probe, nanosecond electron pulses can also be sufficient to resolve carrier dynamics in time as many semiconductor materials have lifetimes in the nanosecond and microsecond timescales. However, suppose we have a material with a mobility of $0.3 \text{ m}^2\text{V}^{-1}\text{s}^{-1}$, typical for a common semiconductor like GaAs. It would be interesting to resolve in such a system the carrier dynamics, as the charges would diffuse 100 nm in a timespan of only 1.3 ps. Hence, ultrafast electron pulses are required to resolve carrier dynamics at these time and length scales. Creating picosecond and sub-picosecond electron pulse lengths while remaining the electron beam quality is not trivial and will be discussed in chapter 3 where we will introduce our own concept for a blanker to create ultrafast electron pulses.

2.6 Conclusions

We have presented an experimental platform based on an integrated light and electron microscope for (ultra)fast SEM including time-resolved CL and laser pump electron probe microscopy. Contrary to most existing recent approaches for these two techniques, we use a standard electrostatic beam blanker to create sub-100ps electron pulses focused in a spot smaller than 50 nm at a beam energy of 4 keV. Laser excitation is performed via the integrated light microscope using a high-NA objective lens. Pre-compensation of the dispersion introduced by objective lens and vacuum window, gives a measured laser pulse length in the focal plane of about 15 fs in a FWHM spot size of about 620 nm. We have demonstrated the spatial and temporal alignment of pulsed laser and electron beams with a proof-of-principle pump-probe measurement on MoS₂. Besides (ultra)fast SEM, the system could also be useful for correlative second harmonic generation, multi-photon luminescence, photo-electron (PE) emission and SEM. The PE signal could be collected with the standard Everhardt-Thornley detector of the microscope. The experimental setup described in this chapter is thus useful to measure both the optical properties at high spatial resolutions with a pulsed electron beam and

could potentially measure the carrier dynamics of solid state devices by combination of a tightly focused pulsed laser and electron beam.

Bibliography

1. Curto, A. G. *et al.* Unidirectional emission of a quantum dot coupled to a nanoantenna. *Science* **329**, 930–3 (2010).
2. Zhang, S. *et al.* Experimental demonstration of near-infrared negative-index metamaterials. *Phys. Rev. Lett.* **95**, 1–4 (2005).
3. Cao, L., Park, J. S., Fan, P., Clemens, B. & Brongersma, M. L. Resonant germanium nanoantenna photodetectors. *Nano Lett.* **10**, 1229–1233 (2010).
4. Tang, L. *et al.* Nanometre-scale germanium photodetector enhanced by a near-infrared dipole antenna. *Nat. Photonics* **2**, 226–229 (2008).
5. Novotny, L. & van Hulst, N. Antennas for light. *Nat. Photonics* **5**, 83–90 (2011).
6. Beard, M. C., Luther, J. M. & Nozik, A. J. The promise and challenge of nanostructured solar cells. *Nat. Nanotechnol.* **9**, 951–954 (2014).
7. Anderson, M. S. Locally Enhanced Raman Spectroscopy with an Atomic Force Microscope. *Appl. Phys. Lett.* **76**, 3130–3132 (2000).
8. Kauranen, M. & Zayats, A. V. Nonlinear plasmonics. *Nat. Photonics* **6**, 737–748 (2012).
9. Dombi, P. *et al.* Ultrafast strong-field photoemission from plasmonic nanoparticles. *Nano Lett.* **13**, 674–8 (2013).
10. Putnam, W. P., Hobbs, R. G., Keathley, P. D., Berggren, K. K. & Kartner, F. X. Optical-field-controlled photoemission from plasmonic nanoparticles. *Nat. Phys.* 1–5 (2016). doi:10.1038/nphys3978
11. Higuchi, T., Maisenbacher, L., Liehl, A., Dombi, P. & Hommelhoff, P. A nanoscale vacuum-tube diode triggered by few-cycle laser pulses. *Appl. Phys. Lett.* **106**, (2015).
12. García de Abajo, F. J. Optical excitations in electron microscopy. *Rev. Mod. Phys.* **82**, 209–275 (2010).
13. Yamamoto, N., Araya, K. & García de Abajo, F. J. Photon emission from silver particles induced by a high-energy electron beam. *Phys. Rev. B* **64**, 205419 (2001).
14. Kuttge, M. *et al.* Local density of states, spectrum, and far-field interference of surface plasmon polaritons probed by cathodoluminescence. *Phys. Rev. B* **79**, 2–5 (2009).
15. Sapienza, R. *et al.* Deep-subwavelength imaging of the modal dispersion of light. *Nat. Mater.* **11**, 781–7 (2012).
16. Coenen, T., Vesseur, E. J. R. & Polman, A. Angle-resolved cathodoluminescence spectroscopy. *Appl. Phys. Lett.* **99**, 143103 (2011).
17. Narváez, A. C. *et al.* Cathodoluminescence Microscopy of nanostructures on glass substrates. *Opt. Express* **21**, 29968–29978 (2013).

18. Zonneville, A. C. *et al.* Integration of a high-NA light microscope in a scanning electron microscope. *J. Microsc.* **252**, 58–70 (2013).
19. Liv, N. *et al.* Simultaneous Correlative Scanning Electron and High-NA Fluorescence Microscopy. *PLoS One* **8**, e55707 (2013).
20. Haring, M. T. *et al.* Automated sub-5 nm image registration in integrated correlative fluorescence and electron microscopy using cathodoluminescence pointers. *Sci. Rep.* **7**, 43621 (2017).
21. Narváez, A. C., Weppelman, I. G. C., Moerland, R. J., Hoogenboom, J. P. & Kruit, P. Confocal filtering in cathodoluminescence microscopy of nanostructures. *Appl. Phys. Lett.* **104**, 251121 (2014).
22. Merano, M. *et al.* Probing carrier dynamics in nanostructures by picosecond cathodoluminescence. *Nature* **438**, 479–482 (2005).
23. Meuret, S. *et al.* Photon bunching reveals single-electron cathodoluminescence excitation efficiency in InGaN quantum wells. *Phys. Rev. B* **96**, 1–8 (2017).
24. Meuret, S. *et al.* Complementary cathodoluminescence lifetime imaging configurations in a scanning electron microscope. *Ultramicroscopy* **197**, 28–38 (2019).
25. Polman, A., Kociak, M. & García de Abajo, F. J. Electron-beam spectroscopy for nanophotonics. *Nat. Mater.* (2019). doi:10.1038/s41563-019-0409-1
26. Zewail, A. H. Four-dimensional electron microscopy. *Science* **328**, 187–93 (2010).
27. Mohammed, O. F., Yang, D.-S., Pal, S. K. & Zewail, A. H. 4D scanning ultrafast electron microscopy: visualization of materials surface dynamics. *J. Am. Chem. Soc.* **133**, 7708–11 (2011).
28. Yang, D.-S., Mohammed, O. F. & Zewail, A. H. Scanning ultrafast electron microscopy. *Proc. Natl. Acad. Sci. U. S. A.* **107**, 14993–8 (2010).
29. Sun, J., Melnikov, V. A., Khan, J. I. & Mohammed, O. F. Real-Space Imaging of Carrier Dynamics of Materials Surfaces by Second-Generation Four-Dimensional Scanning Ultrafast Electron Microscopy. *J. Phys. Chem. Lett.* **6**, 3884–3890 (2015).
30. Cho, J., Hwang, T. Y. & Zewail, A. H. Visualization of carrier dynamics in p(n)-type GaAs by scanning ultrafast electron microscopy. *Proc. Natl. Acad. Sci. U. S. A.* **111**, (2014).
31. Stavenga, T. *Compensation of dispersion experienced in an objective lens for ultrashort laser pulses.* (2014).
32. Diels, J.-C. M., Fontaine, J. J., McMichael, I. C. & Simoni, F. Control and measurement of ultrashort pulse shapes (in amplitude and phase) with femtosecond accuracy. *Appl. Opt.* **24**, 1270–1282 (1985).
33. Hommelhoff, P., Sortais, Y., Aghajani-Talesh, A. & Kasevich, M. a. Field Emission Tip as a Nanometer Source of Free Electron Femtosecond Pulses. *Phys. Rev. Lett.* **96**, 077401 (2006).
34. Lassise, A., Mutsaers, P. H. A. & Luiten, O. J. Compact, low power radio frequency cavity for femtosecond electron microscopy. *Rev. Sci. Instrum.* **83**, 043705 (2012).

35. Thong, J. T. L. Picosecond electron pulse generation via beam deflection-chopping in the SEM. *Meas. Sci. Technol.* 207–216 (1991).
36. Moerland, R. J., Weppelman, I. G. C., Garming, W. H., Kruit, P. & Hoogenboom, J. P. Time-resolved cathodoluminescence microscopy with sub-nanosecond beam blanking for direct evaluation of the local density of states. *Opt. Express* **24**, 499–504 (2016).
37. Moerland, R. J., Weppelman, G., Scotuzzi, M. & Hoogenboom, J. P. Nanoscale imaging of light-matter coupling inside metal-coated cavities with a pulsed electron beam. *Nano Lett.* (2018). doi:10.1021/acs.nanolett.8b00546
38. Garming, M. W. H. *et al.* Nanoparticle discrimination based on wavelength and lifetime-multiplexed cathodoluminescence microscopy. *Nanoscale* (2017). doi:10.1039/C7NR00927E
39. Najafi, E., Liao, B., Scarborough, T. & Zewail, A. Imaging Surface Acoustic Wave Dynamics in Semiconducting Polymers by Scanning Ultrafast Electron Microscopy. *Ultramicroscopy* (2017). doi:10.1016/j.ultramic.2017.08.011
40. Garming, M. W. H. Photon electron pump probe microscopy with nanoscale resolution. (Delft University of Technology, 2017).
41. Müller, M., Squier, J., Wolleschensky, R., Simon, U. & Brakenhoff, G. Dispersion pre-compensation of 15 femtosecond optical pulses for high-numerical-aperture objectives. *J. Microsc.* **191**, 141–150 (1998).
42. von Vacano, B., Buckup, T. & Motzkus, M. Shaper-assisted collinear SPIDER: fast and simple broadband pulse compression in nonlinear microscopy. *J. Opt. Soc. Am. B* **24**, 1091 (2007).

3 Concept and design of a beam blanker with integrated photoconductive switch for Ultrafast Electron Microscopy

This chapter is published in Ultramicroscopy [1] and in [2].

Ultrafast electron microscopy (UEM) is an emerging field where the aim is to achieve sub-picosecond temporal resolution with spatial resolution in the nanometer scale. This capability enables imaging in space and time of phenomena such as spin dynamics[3], excited state dynamics[4], optical near fields[5–8], quantum optical effects[9] and motion of atoms.[10] Almost all applications of UEM rely on pump-probe experiments, where a laser pulse serves as the pump modifying the characteristics of the sample and the electron pulse probes the relaxation of the sample towards equilibrium. Thus, accurate, preferably jitter-free, locking of the ultrashort electron pulses to a laser clocking pulse is of paramount importance. Also, the repetition rate of the electron pulses should be equal to the repetition rate of the laser.

Typically, pulsed electron beams are created by modifying the source unit of an electron microscope (EM) to allow laser-triggered emission. For example, a flat photocathode illuminated with a femtosecond laser can be employed to create femtosecond electron pulses.[11] However, flat photocathodes have a low brightness. For this reason tip based photo-field emitters are used[12–14], which can have brightness values comparable to regularly used Schottky emitters [15] as measured by Feist *et al.* [16] and also by Dominik *et al.* because coherence is related to the reduced brightness.[17]

A known alternative to a laser triggered source is the use of a beam blanker. Beam blankers allow both pulsed electron beam operation for time-resolved measurements and DC operation mode for normal imaging, where a user can relatively quickly switch between both modes of operation. For a laser triggered Schottky source, switching between DC and pulsed modes of operation can take up to 1 hour.[16] Beam blankers based using microwave cavities to create ultrashort electron pulses were envisioned and realized by Oldfield[18] and Ura and co-workers. In this way, electron pulses of 200 fs were created.[19] At that time, the electron pulses were used to measure switching speeds in electronic circuits and transistors by means of voltage contrast.[20,21] Lassise *et al.* and van Rens *et al.* calculated that a TEM₁₁₀ cavity positioned conjugate to the electron beam focal point is able to create ultrashort electron pulses while maintaining the brightness of the continuous electron beam, recently such a TEM₁₁₀ cavity is incorporated in a commercial TEM.[22–24] Advances in technology now allow synchronization between an RF microwave cavity and a laser clock pulse to values of 100 fs and shorter, where additionally care has to be taken to match the GHz microwave frequency to typical MHz laser repetition rates.[25,26] Beam blanking triggered by a laser clocking pulse would directly and in a straightforward way synchronize electron and laser pulses.

Here, we present such an approach to create ultrafast electron pulses with a laser-triggered beam blanker. In our concept femtosecond electron pulses are achieved through a combination of an electrostatic beam blanker and a photoconductive switch illuminated with femtosecond laser pulses.[27] The use of a photoconductive switch enables miniaturization of the ultrafast beam blanker (UFB) such that it can be directly inserted in an existing, commercial EM. Also

the UFB is jitter-free locked to the laser pulse, essential for achieving electron pulses deep in the femtosecond time range. We will first present the concept of our UFB and discuss the basic requirements for realization. We will then turn more in-depth to the requirements on the photoconductive switch and physical properties of available materials, which leads to a set of parameters for the actual design. Based on these we derive the spatial and temporal resolution that could be achieved with such a design. This shows that electron pulses in the 100 femtosecond time range with sub-10 nm spatial resolutions may be feasible.

3.1 UFB concept and requirements

Electrostatic beam blankers are commonly used in EM's to ensure that the sample is exposed to the electron beam only when demanded, for example for electron-beam lithography. In such a blanker the electron beam is deflected and then blocked by an aperture. The preferred position for the blanker is in a plane conjugate to the image plane located at the sample, as indicated in Figure 3.1. [28][24] This ensures that the position of the electron spot is at a steady position at the sample while the blanker deflects the electron beam. We want to use this same concept to generate femtosecond electron pulses, sweeping the electron beam over an aperture in (sub-) picosecond time scales.

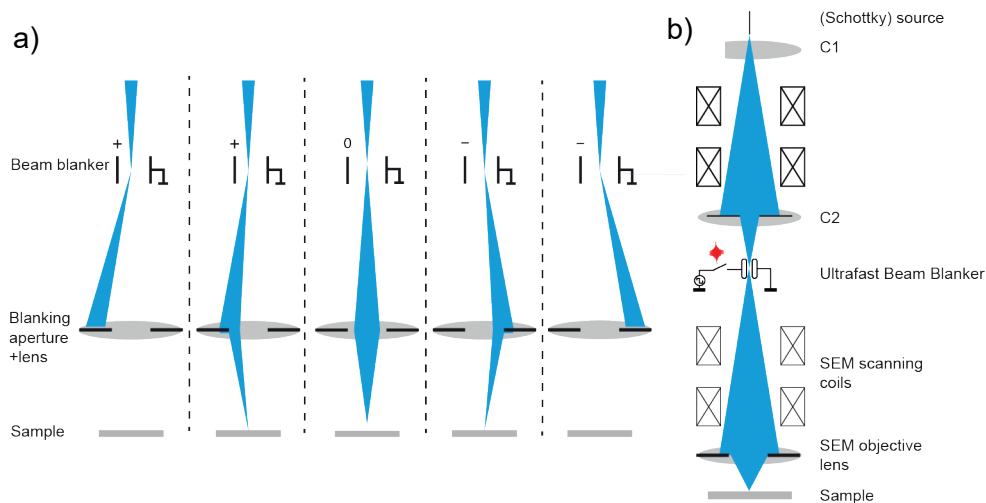


Figure 3.1. a) Schematic drawing indicating conjugate beam blanking using an electrostatic deflector to sweep the electron beam over a blanking aperture. The deflector is in a conjugate plane with respect to the image/sample plane to ensure that the electron probe is always at the same location at the sample irrespective of the electric field strength in the deflector, neglecting aberrations of the objective lens. b) System overview of a commercial SEM, which can have a high brightness Schottky electron source. C1 and C2 denote condenser lenses to focus the electron beam between the blanker plates. The UFB is positioned at the standard entry port for blankers or variable apertures.

A first requirement for our beam blanker is that the electron beam sweeps back and forth over the aperture at (sub-)picosecond timescales. Obviously, this needs inversion of the voltage over the deflector. As we want to synchronize the electron pulses to the output of a femtosecond laser (see details later), another important requirement is that the electron pulses are generated at a rate equal to the repetition rate of the laser. In order to sweep the electron beam ultrafast over the aperture in both positive and negative direction, we propose the innovative scheme shown in Figure 3.2.

By electrically connecting the photoconductive switch and beam deflector in series, the voltage at the feed plate can be inverted each time the switch has been illuminated with the laser pulse. For this to be possible the photoconductive switch has to return to its insulating state after laser illumination on a timescale fast compared to the interval between the laser pulses. In that case the voltage at the feed plate can be inverted while the voltage at the deflector plate remains constant. This then ensures that the electron beam is swept over the blanker aperture in opposite directions for consecutive laser pulses. Hence, below the blanking aperture we will generate electron pulses at a repetition rate equal to the femtosecond laser system.

To increase the average current in the pulsed electron beam, it is advantageous to work at highest possible laser repetition rates, in practice about 100 MHz. This requirement limits the pulse energy available for operating the photoconductive switch to the nanojoule range, as this is the typical operation energy for high repetition rate femtosecond lasers.

For pump-probe measurements with a laser and electron pulse the temporal resolution is not only set by the electron pulse length but also by the amount of jitter between the laser pulse and electron pulse. The latter requirement of minimal jitter is relatively easily satisfied because we use a photoconductive switch illuminated with a laser pulse to change the deflection voltage at the beam blanker. In other words there is a direct link between the laser pulse and the change in voltage. A minimal amount of timing jitter is still present, we will discuss this at the end of this chapter.

In general, for photoconductive switches, a short recombination time is important to generate short voltage pulses. However, in our case this is not important, because we directly connect the photoconductive switch to the beam blanker (see Figure 3.2) and only use the rising part to charge the deflector plate and sweep the beam. When the laser illuminates the photoconductive switch, electrons are excited to the conduction band, and, under influence of the bias electric field, diffuse to the blanker plate and (de)charge it.

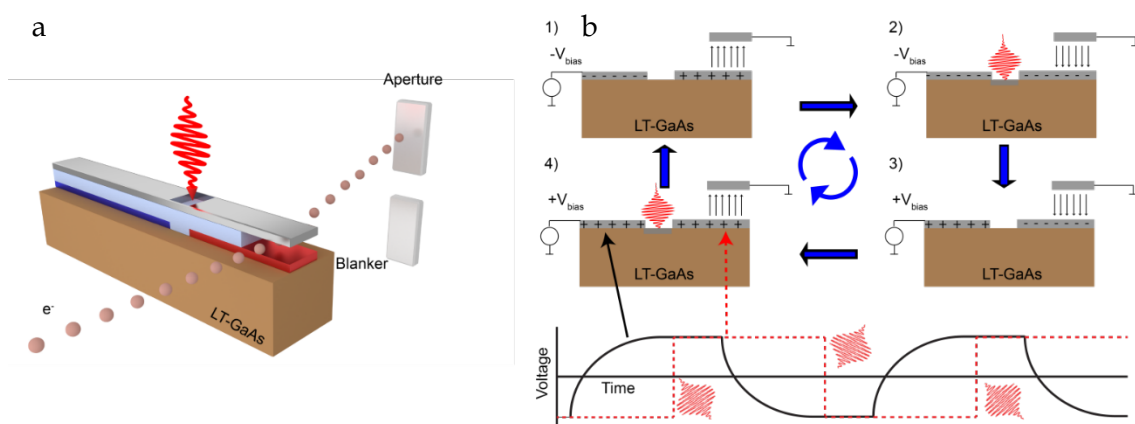


Figure 3.2: (a) Schematic indication of our UFB concept: a photoconductive switch is connected to an electrostatic beam blanker, the electron beam is deflected and intercepted by an aperture, the colors of the electrodes indicate +10 V (blue), negative -10 V (red) and ground (grey). (b) Full modulation cycle for the UFB: (1) the beam is initially blanked by the deflection field in the blanker; (2) laser irradiation provides a conductive channel in the GaAs wafer inverting the voltage on the deflector and thus the deflection direction; (3) after the laser pulse, the GaAs restores to its insulating state, subsequently the bias on the feed voltage from the supply line is switched; (4) a next laser pulse again inverts the field in the deflector, sweeping the beam in opposite direction, after which the voltage supply inverts again and the modulation cycle is back to the initial situation.

Finally, to create ultrashort electron pulses with the concept discussed here, it is essential that photoconductive switch and deflector have a short response time. For this reason we discuss the physical processes occurring in the photoconductive switch and resulting implications for the design in the next paragraphs. We start with a short literature discussion that shows that photoconductive switches are known to have ultrashort response times. We then discuss the requirements on the semiconductor material to be used and subsequently calculate the achievable conductivity in and field strengths over the switch. Based on the photoconductive switch design requirements the dimensions of the beam deflection unit can be calculated, which we show in paragraph 3.4. Then, in paragraph 3.5, we provide an estimation of the achievable electron pulse length for the set of parameters required for the design. We also estimate the amount of jitter of the electron pulse with respect to the laser pulse in paragraph 3.6. The chapter ends with a conclusion and discussion of the concept and results.

3.2 Photoconductive switch

In the above concept, a photoconductive switch is used to create an ultrafast voltage ramp. A photoconductive switch basically consists of a semiconductor material in between two metal contacts, see Figure 3.3. In the literature, such a device is also called an Auston switch, named after the inventor.[29]

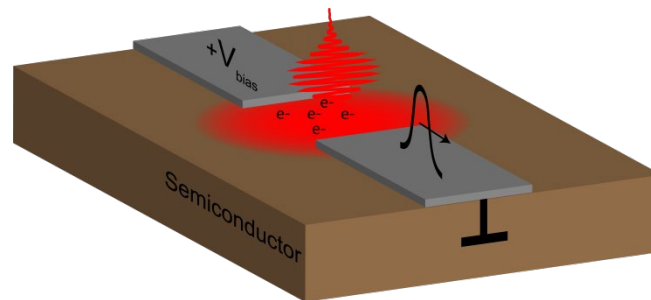


Figure 3.3: Basic principle of a photoconductive switch. Two conductors are connected via an isolating semiconductor material, a laser pulse creates free carriers to provide a conductive channel between the electrodes. Due to recombination of e-h pairs and/or diffusion of electrons and holes to the metal electrodes the conductivity will decrease again after illumination with the laser pulse.

Photoconductive switches creating 825 V pulses with 1.4 ps rise time have been demonstrated[30], and fast photoconductive switches with >100 GHz bandwidth have also been demonstrated.[31] Photoconductive switches are also commonly used to generate THz pulses.[32] Photoconductive switches are also employed to create streak cameras to characterize electron pulses[33] and for X-ray streak cameras[34]. Most photoconductive switches are made of the direct band-gap semiconductors GaAs or LT-GaAs, the latter consisting of a special top layer of GaAs grown at a lower temperature.[35] These two semiconductor materials have the highest conductivity under laser illumination. LT-GaAs has a somewhat lower conductivity under laser illumination compared to GaAs but a shorter carrier recombination time, of the order of 1 ps while normal GaAs has a recombination time of about 1 ns.[36] In applications where short voltage pulses are required, LT-GaAs is the preferred choice, because the voltage pulse length is limited by the carrier lifetime.

For the UFB only the rising part of the photocurrent is important, as this determines the time to charge the deflector plate. However, as discussed above and indicated in Figure 3.2, the photoconductive switch also has to return to the insulating state comparatively fast to be able

to modulate the voltage at the feed plate. Otherwise, the voltage at the deflector plate, indicated with the red dotted line in Figure 3.2, will be affected when the voltage at the feed plate is inverted. Hence, to sufficiently isolate the deflector and feed plate the dark resistance, $R_{s,off}$, has to obey the following inequality:

$$R_{s,off} C_{blanker} > \frac{1}{f} \quad (3.1)$$

where $C_{blanker}$ is the capacity of the deflector plate and f is the repetition rate of the laser. In the following paragraphs we will argue that the capacitance of the deflector plate has to be lower than 10 fF. A typical Ti:Sapph laser has a repetition rate, of about $f = 100$ MHz, lower repetition rates are not attractive because the average probe current will be reduced, as mentioned in the previous paragraph. Hence, high values of the dark resistance are required, of the order of $10^6 \Omega$ range. This in turn requires a relatively short recombination time. For this reason it is not preferred to use regular, 1 ns recombination time, GaAs for the photoconductive switch, but LT-GaAs instead. For experiments where a low repetition rate is required, the repetition rate of the electron pulse can be reduced by switching the feed plate voltage, indicated in Figure 3.2b, at half the desired repetition rate for the electron pulses.

3.2.1 Response time photoconductive switch

We will now discuss the conductivity values that can be achieved and the electric field strength that can be maximally applied over the photoconductive switch. Hereto, we first consider the physical processes occurring in the photoconductive switch after and during illumination with a femtosecond laser pulse, based on a Drude-Lorentz model.

Upon laser illumination, electron hole pairs are created in the photoconductive switch provided the photon energy is larger than the bandgap. We assume that every photon in the pulse creates an electron hole pair with the same probability, determined by an absorption coefficient and a quantum efficiency. Initially, electron and hole will be at 'rest' followed by acceleration in the electric field. The average electron velocity, v , is described by Newton's 2nd law:

$$\frac{dv}{dt} = \frac{e}{m^*} E - \frac{v}{\tau_s} \quad (3.2)$$

where m^* is the effective mass of the electrons, equal to 6.7% of the electron rest mass, E is the local electric field, τ_s is the momentum scattering time, equal to about 30 fs.[37] The scattering term describes the loss of kinetic energy due to collisions of the free carriers with the lattice. The electric field consists primarily of the voltage applied on the electrodes but can be partially screened by surrounding free charges. We note that each electron also has a random thermal motion, but equation (3.2) describes the net average velocity opposite the direction of the electric field.

With the average velocity we can calculate the current density in the semiconductor:

$$j = nev = \sigma E \quad (3.3)$$

where n is the free carrier density and σ the conductivity. We assume a constant or slowly changing electric field E , and convolve the solution of equation (3.2) with a Gaussian laser pulse, with a typical length of 50 fs FWHM, to find how the conductivity in the semiconductor develops in time. The result is given in Figure 3.4, which shows that the conductivity builds up in about 100 fs.

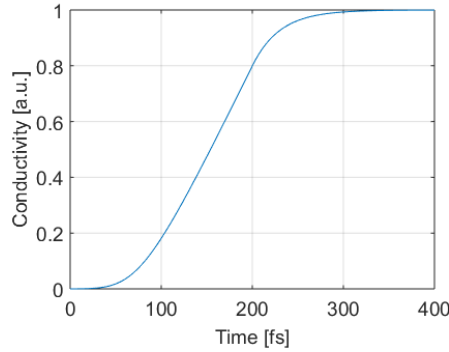


Figure 3.4: Conductivity in the photoconductive switch as function of time for illumination with a Gaussian laser pulse of 50 fs duration and a scattering time in the semiconductor of 30 fs. The calculation is based on a Drude- Lorentz model for the average electron drift velocity, equation(3.2), convoluted with a typical 50 fs FWHM Gaussian laser pulse. It takes approximately 100 fs to build up conductivity in the semiconductor.

We don't take into account negligible nonlinear effects like optical rectification inducing displacement currents at terahertz frequencies. Note that there is also another instantaneous effect on the conductivity, which we did not take into account in calculation the result in Figure 3.4: the laser illumination will lead to a polarization in the semiconductor material which in turn will induce a bound current. However, from literature, this is known to give a negligible contribution to the current at high bias fields.[38,39]

3.2.2 Electric field strength over the photoconductive switch

In the Drude-Lorentz model, the charge carriers at some point reach their so-called drift velocity, v_d , the maximum average velocity due to collisions with each other and the lattice:

$$v_d = \mu E \quad (3.4)$$

where μ is the mobility, about $0.3 \text{ m}^2\text{V}^{-1}\text{s}^{-1}$ for LT-GaAs.[36,40] For example, with a field strength of 2 MV/m, the drift velocity will be $1.6 \cdot 10^5 \text{ m/s}$ according to the Drude-Lorentz model and parameters used in equation (3.2). At low fields the temperature of the charge carriers is equal to the lattice temperature, but at higher fields the carrier temperature begins to deviate from the lattice temperature. Then, the drift velocity no longer increases linearly with the field and starts to saturate. In GaAs, the saturation velocity is about $2 \cdot 10^5 \text{ m/s}$.[41], which is slightly above the drift velocity at 2 MV/m. Note that the thermal velocity of conduction electrons is about $3.7 \cdot 10^5 \text{ m/s}$.

Thus, for an electric field of 2 MV/m, we can assume a linear relation between bias voltage and current. We will use this value in the remainder of this chapter. In principle it is possible to further increase the bias voltage, but other effects like impact ionization and voltage breakdown may then happen. In addition, in III-V compounds, like GaAs, the electron mobility

also decreases with increasing field due to scattering of electrons by optical phonons. It has been shown experimentally that the photocurrent increases at a slower rate at higher fields.[37]

3.2.3 Conductivity photoconductive switch

Equation (3.3) may seem to imply that a higher laser power induces a larger photocurrent and conductivity. However, it should be noted that at relatively high free carrier densities oscillations in the photocurrent may be induced. As the laser creates a plasma of free carriers in the semiconductor material, electrons and holes in the plasma will separate due to the applied electric field. Due to the resulting Coulomb forces the plasma may start oscillating and/or the photocurrent may decay very rapidly. A laser pulse shorter than the momentum scattering time can also lead to these oscillations. In Jepsen *et al.*, these effects are explained in detail and fitted to measurements.[37] It is shown that the onset of plasma oscillations is determined by the product of the scattering time and the plasma frequency, defined as:

$$\omega_p = \sqrt{\frac{ne^2}{\epsilon m^*}} \quad (3.5)$$

where ϵ is the permittivity. We would enter the regime where these oscillations start to occur at $a = \omega_p \tau_s \sim 1$. Therefore, we want to have a density of free carriers at most equal to:

$$n = \frac{a^2 \epsilon m^*}{e^2 \tau_s^2} = 1.15 \cdot 10^{24} \quad [\text{m}^{-3}] \quad (3.6)$$

where we assume a value 12.3 for the relative permittivity and for the product of $\omega_p \tau_s$, we took a value of a equal to 2. Note that there is a difference between the situation described by Jepsen *et al.* and our design, as in their case the electric field over the switch is constant.

To conclude this section, a carrier density of about $1 \cdot 10^{24} \text{ m}^{-3}$ should be achievable in combination with an electric field of 2 MV/m over the photoconductive switch. The switch can be brought in the conductive state in about 100 fs, later we will give more accurate values where we take into account the change in electric field over the photoconductive switch. In the next paragraph we will discuss the dimensions required for the photoconductive switch.

3.3 Transmission of high frequency signals and implications for the design

We have seen above (see Figure 3.4) that the conductivity of the photoconductive switch will change on time scales smaller than 1 ps. This corresponds to terahertz-range frequencies. Transmission of electrical signals with such high frequency components to the deflector is not trivial: Normally for electronics, it is assumed that the potential along a perfect conductor is independent of position even when the potential is time-dependent. However, electrical signals are transferred at the local speed of light. So, when the signal delay, as determined by the length of the cable and its effective permittivity, becomes comparable to 0.1 times the signal rise time, the potential becomes position dependent.

In *vacuum*, a 1 ps electromagnetic wave has a wavelength of $300\ \mu\text{m}$, a line longer than $30\ \mu\text{m}$ will behave like a transmission line. In our case we also have to consider that we have a broadband signal while the response of the electrical circuit can be strongly wavelength dependent. In addition, dispersion may reduce the rise time of the electrical signal. Another issue is that high-frequency signals are absorbed quite strongly by metals due to the low skin-depth and finite conductivity.

Finally, an essential requirement is that the amount of charges necessary to charge or discharge the deflector plate has to be less than the amount of charges created by the laser pulse. Because when all free charges (created by the laser pulse) are taken up by the electrodes the resistance of the photoconductive switch is equal to the initial dark resistance and the photocurrent will drop to zero.

We choose a photoconductive switch with dimensions of 10 by $10\ \mu\text{m}$ because it is only a fraction of the wavelength (of the electromagnetic wave inverting the voltage at the deflector plate) and because the field is set to $2\ \text{MV/m}$, see section paragraph 3.2.2, resulting in a voltage difference of $20\ \text{V}$ over the photoconductive switch which is relatively easy to achieve with standard pulse generators in a few nanoseconds. Under those conditions, we would generate $\sim 10^8$ free carriers, taking into account the required carrier density calculated in section 3.2.3 and assuming a skin depth of $1\ \mu\text{m}$. This means the maximum capacitance we can switch is equal to $8\ \text{pF}$ for a $20\ \text{V}$ difference. The required laser power is low: with an $800\ \text{nm}$ femtosecond laser at a repetition rate of $100\ \text{MHz}$, $5\ \text{mW}$ is required, excluding losses.

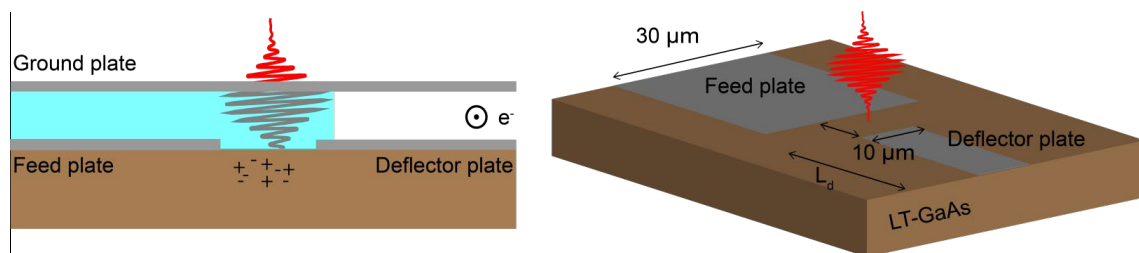


Figure 3.5: (a) Sketch of the photoconductive switch with feed, ground, and deflector plates. The electron beam traverses the space between the ground and deflector plate perpendicular to this plane. (b) View of the LT-GaAs plane from (a), with feed and deflector plates. The photoconductive switch is 10 by $10\ \mu\text{m}$ as discussed in the text. The feed plate is $30\ \mu\text{m}$ wide to assure that locally enough charges are present to charge the deflector plate when the photoconductive switch is in the conductive state.

To summarize, the capacitance that can be connected to the photoconductive switch is limited. Together with the need to reduce absorption, dispersion, and transmission line behavior, this translates to photoconductive switch dimensions of the order of ten micrometers. Therefore, we choose to integrate the photoconductive switch and the deflector in a single MEMS-sized device.

3.4 Dimension MEMS Beam Blanker

In the previous paragraph we discussed that the photoconductive switch and deflector should be integrated in a single MEMS sized device. From this requirement and the required sub- $10\ \text{nm}$ spatial resolution we can calculate typical dimensions for the deflector.

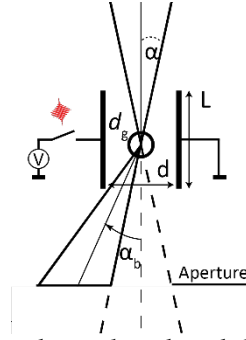


Figure 3.6: Sketch of a beam blanker. The incoming electron beam has a half-opening angle α and has a crossover of diameter d_g between the deflector plates. The deflector has a length l and the plates are separated by a distance d . The deflector sweeps the beam over an aperture. α_b is the smallest deflection angle with which the beam is completely blocked by the aperture.

The deflection angle can be calculated from the dimensions of the blanker using the following equation (see also Figure 3.6):

$$\alpha_b = \frac{El}{2\phi} = \frac{V_b l}{2\phi d} \quad (3.7)$$

where E is the electric field between the deflector plates, V_b the voltage difference over the deflector plates and ϕ is the acceleration voltage. All other variables are defined in Figure 3.6.

The two requirements for blanking are:

$$\begin{aligned} \alpha_b &> 2\alpha \\ d &> d_g + \alpha l \end{aligned} \quad (3.8)$$

where d_g is the diameter of the focused spot between the deflector plates, i.e. the crossover diameter. The first requirement states that we have to deflect at least an angle α_b to have the beam completely blocked by the aperture. The second requirement states that the beam should not hit the deflector plate.

Equation (3.8) tells that the blanking angle will be determined by the half opening angle. In electron microscopy, the choice of half-opening angle α_b is a balance between spatial resolution and probe current. A higher opening angle leads to a larger current but at the cost of spatial resolution due to increasing lens aberrations, except at very low opening angles where diffraction can become dominant. With our beam blanker, the current at the sample will be reduced significantly compared to continuous beam operation. Therefore, in the remainder of this section we will work with a high beam current of 16 nA. For 100 fs electron pulses and a repetition rate of 100 MHz, this will result in a duty cycle of $1 \cdot 10^{-5}$. With this 16 nA DC current, every electron pulse will on average contain 0.01 electron.

With the 16 nA current, and considering the probe size limited by spherical aberration and source to image plane magnification, the probe size at the sample is given by[42]:

$$I_p = 2.47 \frac{d_p^{8/3} B_r \phi}{C_s^{2/3}} \quad (3.9)$$

where we assume a reduced brightness $B_r = 5 \cdot 10^7$ A/m²srV and $C_s = 15$ mm. Notice that we a spherical aberration coefficient for a non-immersion lens, in a system with an immersion lens

the spherical aberration coefficient will be lower and subsequently the probe will be reduced. The acceleration voltage, ϕ , is taken to be equal to 30 kV to obtain highest spatial resolution and because at lower beam energies the electron pulse length will increase more due to the energy spread within the pulse. The effects of energy spread will be discussed in detail in chapter 4. With the numbers stated above, we see that for a DC current of 16 nA, a spot size of 8.3 nm can be obtained.

With the geometrical part of the spot size at the sample we calculate a FW50 value of 200 nm for the spot size at the blanker, d_g , for a sample to deflector magnification of 30. The opening angle at the blanker can be calculated using conservation of brightness:

$$\alpha_p = \sqrt{\frac{4I_p}{B_r \pi^2 \phi} \frac{1}{d_g}} \quad (3.10)$$

This results in a half-opening angle of 0.32 mrad.

To be able to design the deflector we have to estimate the product of the blanking voltage V_b and blanker length l which can be calculated as:

$$V_b l > 2\phi\alpha_b d = 38.9 \cdot 10^{-6} [\text{V} \cdot \text{m}] \quad (3.11)$$

with a separation between the deflector plates, $d = 1 \mu\text{m}$, and $\alpha_b = 0.32$ mrad. The separation between the deflector plates is chosen to be in micrometer-range for two reasons. The first one is that the distance between the electrode containing the signal and the ground plate is preferred to be (deep) subwavelength. The second reason is that with smaller separation, the electric field will be maximized which reduces the required length and blanking voltage. Note that the blanking voltage has to be lower than the maximum deflection voltage that we can deliver with the photoconductive switch, which was 10 V as discussed in the previous paragraph. Also, even smaller distance between the plates is difficult because the system becomes more sensitive to drift and mechanical stability and is also limited by the 200 nm spot diameter of the electron beam in the blanker. Finally, we note that a deflector with an aspect ratio larger than 1:10 will be more difficult to align with respect to the electron optical axis. We then see that for a 10 μm long deflection plate, a blanking voltage of 3.8 V is required.

3.5 Electron pulse length

With the dimensions of the blanker and the blanking voltage set, we can estimate the electron pulse length. Hereto, we need a calculation for the time-dependent voltage at the deflector plate. Two approximations in this section are described to calculate the electron pulse length. In the first approximation we consider the photoconductive switch as a resistor and the deflector as a capacitor and we calculate the RC time.

From the conductivity, calculated in section 3.2.3, a mobility of 3000 $\text{cm}^2/\text{V}\cdot\text{s}$, and skin-depth of 800 nm light in GaAs of 1 μm , the resistance of the photoconductive switch is about 18 Ω . The deflector plate, indicated in

Figure 3.5, can be approximated as a parallel plate capacitor with a capacitance of 6 fF, neglecting parasitic capacitances. Where it is assumed that the area is equal to $l \cdot L_d = 300 \mu\text{m}^2$,

and the plate separation is $1 \mu\text{m}$ in combination with a relative permittivity of 2.25 due to the presence of glass. Hence the RC time is about 110 fs, in combination with a conductivity built-up of about 100 fs, shown in Figure 3.4, and square addition the electron pulse length will be in the order of 150 fs.

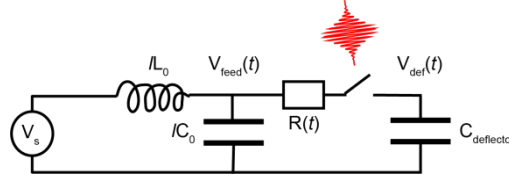


Figure 3.7: Schematic of the electrical circuit used. With a set of differential equations the time-dependent voltage at the feed plate, $V_{\text{feed}}(t)$, and at the deflector plate $V_{\text{def}}(t)$ is calculated. The voltage delivered by the source, V_s , is constant. The resistance of the photoconductive switch, $R(t)$ is time-dependent. Also the Drude model and a laser pulse duration of 25 fs is taken into account.

In the RC time calculation the response of the photoconductive switch is not considered. In reality the photoconductive switch has a non-zero response time as described by the Drude-Lorentz model in equation (3.2). Also the electric field over the photoconductive switch depends on time after illumination.

For this reason, we performed a second approach which also takes into account the response time and the time-dependency of the conductivity. We implement a time-dependent field over the photoconductive switch by modeling the transmission line between constant voltage source and photoconductive switch with an inductor L_0 and capacitor C_0 (Figure 3.7). Also, we take a time-dependent resistance of the photoconductive switch using the Drude-Lorentz model described in section 3.2.1. Finally, the finite duration of the laser pulse is taken into account using a Gaussian pulse shape with 25 fs FWHM. In this way, we derive a set of differential equations, as detailed in the Appendix of this chapter. These are numerically solved with MATLAB. A scattering time τ_s of 30 fs is assumed for this calculation which corresponds to a mobility of $786 \text{ cm}^2/\text{Vs}$, the exact mobility and scattering time do depend on, for example, the annealing time of the LT-GaAs layer.[36] The results of the calculation are shown in Figure 3.8, all values used in the calculations are listed in the Appendix.

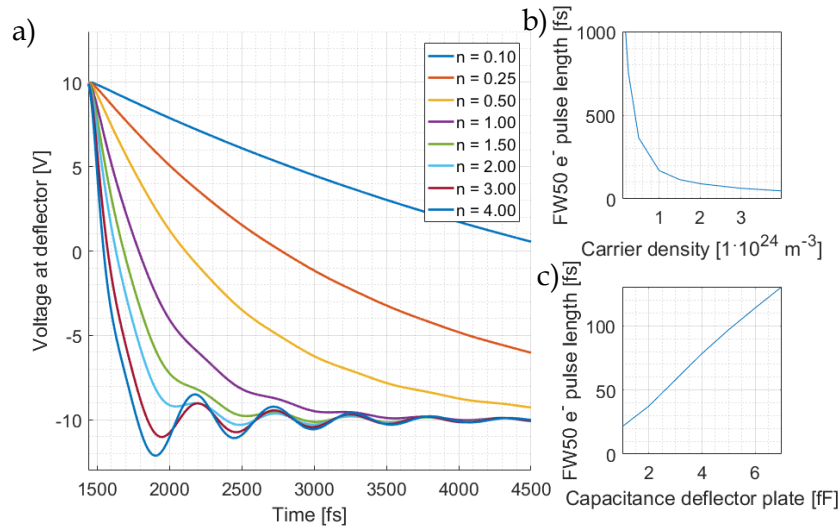


Figure 3.8: (a) Calculated voltage at the deflector plate as function of time for different free carrier densities n in $[1 \cdot 10^{24} \text{ m}^{-3}]$. At high carrier densities oscillations occur which has to do with the delay in the supply of charges at the feed plate. (b) The FW50 electron pulse length increases with lower carrier density. In (a) and (b) the capacitance of the deflector is 6 fF. (c) FW50 electron pulse length as function of the feed plate capacitance, for a fixed carrier density of $1.5 \cdot 10^{24} \text{ m}^{-3}$. In the calculations, the voltage at which the electron beam is fully blanked is assumed to be 3.8V.

In Figure 3.8b we can see that the FW50 electron pulse length increases when the carrier density decreases, which does not occur in the simple linear relation predicted by the bare RC model. One reason for this is that in the time-dependent model, the response of the switch becomes limited by the acceleration of free carriers.

Figure 3.8c clearly shows that the pulse length strongly depends on the capacitance of the deflector plate. A low value for the capacitance results in a short electron pulse length. However, as stated before (see, e.g., equation (3.1)), a low capacitance also reduces the RC time in the dark state of the switch. For too low capacitance, it will become impossible to invert the voltage at the feed plate between two subsequent laser pulses while keeping the voltage at the deflector plate constant. A typical dark resistance is measured to be in the 10 M Ω range, resulting in a RC time of 10 ns for a 1 fF deflector. This is too low for a laser repetition rate of 100 MHz.

The electron pulse length depends linearly on the capacitance of the deflector plate, as shown in

Figure 3.8c. Analytical equations to estimate the exact capacitance of a 3D geometry with different dielectric materials around the deflector are not available. We will discuss this further in chapter 4 where we performed numerical simulations of the UFB.

3.6 Time jitter between the laser pulse and the electron pulse

In the previous section we have calculated that electron pulses in the 100 fs range are feasible. However, the temporal resolution in a UEM is not only determined by the electron pulse length but also due to time jitter between the laser pulse envelope and the electron pulse. The jitter is present because the photoconductive switch converts an optical signal, the laser pulse, to an electronic signal which has some noise. The noise on the voltage will be converted to time jitter due to a time shift in the zero crossing of the deflector voltage.

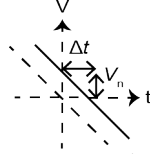


Figure 3.9: Voltage over the deflector as function of time in case without noise, dotted line, due to voltage noise, V_n , the graph moves to the right, solid line, the zero crossing by an amount Δt . Hence the electron pulse is also shifted by an amount of Δt .

We consider two contributions to the jitter; thermal noise and shot noise. Firstly the latter contribution is estimated, the rms shot noise current is given by:

$$I_{shot} = \sqrt{2eI_{avg}\Delta f} = \sqrt{\frac{2en_f I_{avg}}{\tau_0}} \quad (3.12)$$

where I_{avg} is the average current and Δf is the bandwidth. The bandwidth is equal to a factor n_f times the inverse of the time constant τ_0 of the system. The power spectral density of shot noise is constant as long as the frequency is smaller than $1/\tau_e$, where τ_e is the pulse width of a one electron pulse.

The average current, I_{avg} , through the capacitor is calculated as follows:

$$I(t) = C_{def} \frac{dV}{dt} = 2 \frac{C_{def} V_0}{\tau_0} \exp(-\tau / \tau_0) \quad (3.13)$$

$$I_{avg} = \frac{C_{def} V_0}{4\tau_0^2} \int_0^{4\tau_0} \exp(-\tau / \tau_0) d\tau \approx \frac{C_{def} V_0}{2\tau_0}$$

where we estimate the deflector is exponentially charged with a time constant τ_0 . The average current I_{avg} is calculated by integrating the current over a time window of $4\tau_0$. The shift in charging time is approximated as:

$$\Delta t \approx \frac{I_{shot}}{I_{avg}} \tau_0 = 2 \sqrt{\frac{qm_f}{V_0 C_{def}}} \tau_0 \quad (3.14)$$

When a time constant of 300 fs, a deflection voltage of 10 V and a capacitance C_{def} of 7 fF and a n_f of 3 (corresponding to a 10 THz bandwidth) is assumed, the shot noise jitter contribution is about 1 fs.

Jitter is also introduced by thermal agitation of charge carriers, as discussed by Nyquist.[43] Thermal voltage noise over a capacitor can be calculated with the equipartition theorem and is equal to:[44]

$$v_n = \sqrt{\frac{kT}{C_{def}}} \quad (3.15)$$

where k is Boltzmann's constant and T the temperature. The drop of thermal noise at high frequencies, around 1 THz, is neglected. From equation (3.15) the time jitter, due to thermal noise, is calculated as:

$$\Delta t \approx \frac{v_n}{V_0} \tau_0 = \frac{1}{V_0} \sqrt{\frac{kT}{C_{def}}} \tau_0 \quad (3.16)$$

For a temperature of 300 K, and all other parameters equal to the values used for the shot noise jitter contribution, a value of 23 as is obtained.

Amplitude noise in the laser will induce noise in the photoconductivity and hence jitter in the electron pulse. In a model where the conductivity of the switch varies linearly with the amount of photons in the pulse, the resulting time jitter for a relative laser amplitude noise η is equal to:

$$\Delta t = t_0 \ln(2) \eta \quad (3.17)$$

For a laser amplitude noise of 0.05% RMS over a bandwidth from 10 Hz the jitter is about 10 as, for longer time scales the power stability is some 0.5% resulting in a time drift of about 1 fs. The latter contribution is only relevant for measurements who require long integration times. The rms amplitude noise and power stability are typical for a Coherent Vitara Ti:Saphh oscillator.

Thus the dominant source of jitter is shot noise which is in the order of 1 fs, so the time jitter is negligible to the electron pulse duration of 100 fs. The amount of time jitter is also significantly lower compared to systems employing GHz cavities, for example Brussard *et al.* achieved 96 fs time jitter and more recently Gliserin *et al.* reduced the timing jitter to 4 fs.[25,26]

In reality the jitter will be larger as the mechanical and thermal stability of the whole setup is essential, mechanical vibration amplitudes in the optical setup will easily add a few femtosecond. Nevertheless, the amount of jitter can be expected to be significantly smaller than the electron pulse length.

3.7 Discussion

The above considerations and modeling have demonstrated the feasibility of operating an UFB based on a laser-illuminated photoconductive switch. In the calculations several idealized assumptions are made, for instance ideal electrical contacts to the photoconductive switch, no parasitic capacitances, no leakage current except through the photoconductive switch.

In our calculations, we have worked with a relatively high DC current of 16 nA in order to optimize the average number of electrons per pulse. A higher brightness electron source or a

lower desired current will lead to (significantly) smaller opening angles and hence higher spatial resolution and shorter electron pulses. We have been conservative by assuming a reduced brightness value of $5 \cdot 10^7$ A/[m²srV]. A factor 4 higher can be achieved with a Schottky emitter as shown by van Veen *et al.*[45]. This would reduce the blanking voltage by a factor of 16 for the same DC current and probe size. Hence, the exact design of the UFB can depend on the EM to be used and for some application lower currents might be acceptable.

The resistance of the photoconductor in its photoconductive state can be adjusted by setting the amount of photons per laser pulse. With fewer photons per pulse, the rise time of the deflection field would decrease. This can be used to increase the pulse length and thus also increase the current for experiments where a lower temporal resolution is acceptable. If required, the repetition rate of the electron pulse can be reduced by inverting the voltage at the feed plate at a rate lower than the laser repetition rate.

The concept of a MEMS-based UFB presented here would in principle be applicable to any type of EM because of its small dimensions. This way constitute a unique advantage compared to other UFB concepts, such as GHz resonant cavities.[46,47] The MEMS sized device could be inserted via a standard EM entry ports used for aperture strips and regular pico- to nanosecond scale beam blankers.[48] At the same time, all DC imaging modalities are kept intact because neither the high brightness electron source nor the column is modified. Also, an EM equipped with a UFB can be switched between pulsed and DC operation without any realignments. In this chapter we assume that the UEM would be used in an imaging mode where the sample and UFB are in conjugate planes. For some imaging techniques like Lorentz microscopy and holography, this is not possible. The effects of sweeping the beam, such as a possible reduction of transverse coherence or a correlation between the spatial domain and the time within the electron pulse will be discussed in chapter 4.

Fabrication of the MEMS sized UFB is in principle possible by using nanotechnology tools such as standard lithography, deposition and etching tools, this will be discussed in chapter 5 of this thesis.

3.8 Conclusion

In this chapter, we have presented a new concept for an ultrafast beam blanker using a combination of an electrostatic deflector connected in series with a photoconductive switch. We have demonstrated the feasibility of this concept based on a design that followed from basic, practical requirements for operation of such an UFB in a standard EM. A crucial aspect of our design is that only the rising part of the signal from the switch is used to invert the voltage over the deflector at sub-picosecond time scales. By inverting the voltage at the feed plate in between laser pulses, it is possible to scan the electron beam over a blanking aperture at ultrafast time scales. By integrating the photoconductive switch with a beam blanker the dimensions can be kept substantially smaller than the wavelength and the capacitance can be reduced, enabling inverting the deflector voltage at (sub-) picosecond time scales. According to our basic models, 100 fs electron pulses with spatial resolution of less than 10 nm can be achieved. Moreover, as the electron beam is only transmitted through the blanking aperture when a laser pulse illuminates the photoconductive switch, there will be minimal jitter (only about 1 fs) between the laser pulse and electron pulse. Our calculations have shown that all

dimensions of the UFB need to be micron scale to prevent transmission line behavior, dispersion and absorption of the high frequency signal components, which is feasible with MEMS fabrication technology. Our concept for an UFB may provide an attractive alternative to do ultrafast electron microscopy, as it does not require modification of the microscope nor realignment between DC and pulsed mode of operation.

3.9 Acknowledgements

This work is part of the research programme of the Foundation for Fundamental Research on Matter (FOM), which is part of the Netherlands Organisation for Scientific Research (NWO). The authors would like to thank P. Planken for useful discussions.

Appendix – Model photoconductive switch and electrical circuit

Here we describe a model of the electrical circuit and photoconductive switch, in order to calculate the time-dependent voltage over the deflector. For the model a set of differential equations is derived describing the time-dependent voltages in the system as function of parameters like the deflector capacitance and laser pulse energy. The results are shown in Figure 3.8 of paragraph 3.5.

In the model it is assumed that the currents in the UFB can be described by basic circuit laws, valid because the dimensions are significantly smaller than the wavelength. Figure 3.10 shows the electrical circuit used for the model. We assume a constant voltage at the source, V_s , connected via a transmission line to the photoconductive switch. The transmission line is simplified as a combination of a capacitor and inductor.

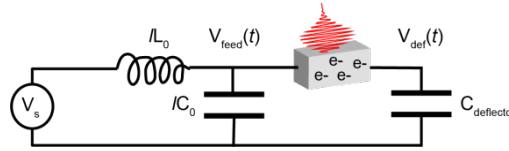


Figure 3.10: Scheme of the electric circuit. A laser pulse illuminates the photoconductive switch which has a length L and cross area A and generates a free carrier density $n(t)$. The carriers accelerate in the field, according to a Drude-Lorentz model, the average velocity, $v(t)$, of the electrons is considered positive when they move to the left in this figure.

The capacitance and inductance in Figure 3.10, L_0 and C_0 , are estimated by assuming the electrodes are like a micro strip line. The characteristic impedance Z_0 of a microstrip line is estimated using the equations in Demarest[49]:

$$\begin{aligned} \epsilon_{eff} &\approx \frac{1}{2}(\epsilon_r + 1) + \frac{1}{2}(\epsilon_r - 1) \left(1 + 12 \frac{w}{h}\right)^{-\frac{1}{2}} \\ Z_0 &\approx \frac{120\pi}{\sqrt{\epsilon_{eff}}} \left[\frac{w}{h} + 1.393 + 0.667 \ln \left(\frac{w}{h} + 1.444 \right) \right]^{-1} \end{aligned} \quad (3.18)$$

This equation is valid for $w/h > 1$, all variables are defined in Figure 3.11. For the relative permittivity we take the average of glass and GaAs which have refractive indices of 1.5 and 3.4 respectively. In our design the characteristic impedance is equal to 4.3Ω .

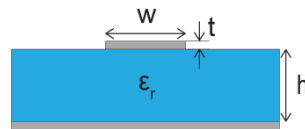


Figure 3.11: Microstrip line with electrode separation h , in our case $1 \mu\text{m}$, the width, w , is equal to $30 \mu\text{m}$. The dielectric has a relative permittivity ϵ_r .

The capacitance per unit length is calculated under the assumption of a simple 2 plate capacitor, with the dimensions indicated in Figure 3.11 and is equal to 1.9 nF/m . From the capacitance and impedance the inductance per unit length is calculated using $L_0 = Z_0^2 C_0$ and is equal to 36 nH/m .

In the following section we use Kirchhoff's current law at the feed plate and deflector plate to derive two higher order ordinary differential equations. The differential equations are

rewritten in a set of first order ordinary differential equations which are numerically solved with Matlab.

The sum of the currents at the feed plate has to be equal to zero:

$$\frac{1}{L_f} \int (V_s - V_f) dt - C_0 \frac{dV_f}{dt} - eAn(t)v(t) = 0 \quad (3.19)$$

The first term describes the effect of the coil, included in the model because the source can't instantaneously deliver new charges to the feed plate. The next term describes the current flowing from the feed plate due to its capacitance. The last term describes the current flowing into the photoconductive switch. Which is determined by the amount of carriers generated by the laser pulse and the average velocity, $v(t)$. Differentiating this equation to time, in order to get rid of the integral, gives:

$$\frac{(V_s - V_f)}{L_0} - C_0 \frac{d^2V_f}{dt^2} - eA \left(v \frac{dn}{dt} + n \frac{dv}{dt} \right) = 0 \quad (3.20)$$

The velocity is described with a Drude-Lorentz model given in equation (3.2), which has an additional term to correct for the reduction in average velocity due to the newly generated free carriers at later time instances[40]:

$$\frac{dv}{dt} = \frac{e}{m^*} E - \frac{v}{\tau_s} - v \frac{dn}{dt} \quad (3.21)$$

where n is the density of charges, proportional to the integral of a Gaussian shaped laser pulse:

$$n(t) = \frac{1}{2} n_0 \left(1 + \operatorname{erf} \left[1.67 \frac{t - t_0}{\tau} \right] \right) \quad (3.22)$$

where n_0 is the total amount of carriers generated by the laser pulse, t_0 is the time the laser pulse illuminates the photoconductive switch and τ is the FWHM laser pulse length. Recombination of electron-hole pairs is not taken into account because it happens at a time scale of 10-15 ps.

Inserting equation (3.21) in equation (3.20) results in the following equation:

$$\frac{(V_s - V_f)}{L_0} - C_0 \frac{d^2V_f}{dt^2} - eA \left(\frac{ne}{Lm^*} (V_f - V_d) - \frac{nv}{\tau_s} \right) = 0 \quad (3.23)$$

Combining this equation with (3.19) by replacing the term $n(t)v(t)$ and differentiating to time:

$$\begin{aligned} & -\frac{1}{L_f} \frac{dV_f}{dt} - C_0 \frac{d^3V_f}{dt^3} - \frac{Ae^2}{Lm^*} \left(\frac{dV_f}{dt} - \frac{dV_d}{dt} \right) n - \frac{Ae^2}{Lm^*} (V_f - V_d) \frac{dn}{dt} + \\ & + \frac{1}{L_f \tau_s} (V_s - V_f) - \frac{C_0}{\tau_s} \frac{d^2V_f}{dt^2} = 0 \end{aligned} \quad (3.24)$$

We now have a differential equation independent of the velocity, v , describing the voltage at the feed plate V_f . A second equation is required because there are still two unknowns, V_f and V_d .

A second differential equation is derived by applying Kirchhoff's circuit rule at the deflector plate:

$$C_d \frac{dV_d}{dt} - eAnv = 0 \quad (3.25)$$

Differentiating this equation to time gives:

$$C_d \frac{d^2V_d}{dt^2} - eA \left(n \frac{dv}{dt} + v \frac{dn}{dt} \right) = 0 \quad (3.26)$$

Inserting equation (3.21) in equation (3.26) results in:

$$\begin{aligned} C_d \frac{d^2V_d}{dt^2} - eA \left(n \frac{e}{m^*} E - \frac{nv}{\tau_s} - v \frac{dn}{dt} \right) &= 0 \\ C_d \frac{d^2V_d}{dt^2} - eA \left(n \frac{e}{m^*} \frac{V_f - V_d}{L} - \frac{nv}{\tau_s} \right) &= 0 \\ \frac{d^2V_d}{dt^2} = \frac{e^2An}{LC_d m^*} (V_f - V_d) - \left(\frac{1}{\tau_s} \right) \frac{dV_d}{dt} \end{aligned} \quad (3.27)$$

With 2 differential equations and 2 unknowns it is possible to numerically calculate the voltages as function of time. In order to solve the set of differential equations numerically, using MATLAB, we rewrite it in a set of first order differential equations, where we define:

$$\begin{aligned} v(1) &= V_d \\ v(2) &= \frac{dV_d}{dt} \\ v(3) &= V_f \\ v(4) &= \frac{dV_f}{dt} \\ v(5) &= \frac{d^2V_f}{dt^2} \end{aligned} \quad (3.28)$$

The set of coupled first order differential equations we solved in MATLAB are:

$$\begin{aligned} v'(1) &= v(2) \\ v'(2) &= \frac{\alpha n}{C_d} (v(3) - v(1)) - \frac{1}{\tau_s} v(2) \\ v'(3) &= v(4) \\ v'(4) &= v(5) \\ v'(5) &= -\frac{1}{\tau_f^2} v(4) - \frac{\alpha n}{C_f} [v(4) - v(2)] \\ &\quad - \frac{\alpha}{C_f} [v(3) - v(1)] \frac{dn}{dt} \\ &\quad + \frac{1}{\tau_s \tau_f^2} [V_s - v(3)] - \frac{1}{\tau_s} v(5) \end{aligned} \quad (3.29)$$

where:

$$\alpha = \frac{e^2 A}{m^* L}, \quad \tau_f^2 = C_f L_f \quad (3.30)$$

A value of 1.9 nF/m and 35 nH/m is used for respectively the capacitance and inductance of the feed plate. We use a length, L_f , of 10 μm for the transmission line. The cross section A is equal to 10 μm^2 , L is equal to 10 μm and the effective mass is $0.067m_0$, where m_0 is equal to the electron rest mass. A value of 6 fF is used for the capacitance of the deflector plate. The electron scatter time is taken to be equal to 30 fs, corresponding to a mobility of 786 $\text{cm}^2/\text{V}\cdot\text{s}$.

Bibliography

- [1] I.G.C. Weppelman, R.J. Moerland, J.P. Hoogenboom, P. Kruit, Concept and design of a beam blaker with integrated photoconductive switch for Ultrafast Electron Microscopy, *Ultramicroscopy*. 184 (2017) 8–17. doi:10.1016/j.ultramic.2017.10.002.
- [2] I.G.C. Weppelman, P. Kruit, WO2016076718A3, WO2016076718A3, n.d.
- [3] R.M. Van Der Veen, O. Kwon, A. Tissot, A. Hauser, A.H. Zewail, Single-nanoparticle phase transitions visualized by four-dimensional electron microscopy, *Nat. Chem.* (2013) 1–8. doi:10.1038/NCHEM.1622.
- [4] D.-S. Yang, O.F. Mohammed, A.H. Zewail, Environmental scanning ultrafast electron microscopy: structural dynamics of solvation at interfaces., *Angew. Chem. Int. Ed. Engl.* 52 (2013) 2897–901. doi:10.1002/anie.201205093.
- [5] B. Barwick, D.J. Flannigan, A.H. Zewail, Photon-induced near-field electron microscopy., *Nature*. 462 (2009) 902–6. doi:10.1038/nature08662.
- [6] A. Yurtsever, R.M. van der Veen, A.H. Zewail, Subparticle Ultrafast Spectrum Imaging in 4D Electron Microscopy, *Science* (80-.). 335 (2012) 59–64. doi:10.1126/science.1213504.
- [7] A. Feist, K.E. Echternkamp, J. Schauss, S. V. Yalunin, S. Schäfer, C. Ropers, Quantum coherent optical phase modulation in an ultrafast transmission electron microscope, *Nature*. 521 (2015) 200–203. doi:10.1038/nature14463.
- [8] A. Ryabov, P. Baum, Electron microscopy of electromagnetic waveforms, *Science* (80-.). 2182 (2016) 2179–2182.
- [9] K.E. Echternkamp, A. Feist, S. Schäfer, C. Ropers, Ramsey-type phase control of free-electron beams, *Nat. Phys.* 12 (2016) 1000–1004. doi:10.1038/nphys3844.
- [10] A.H. Zewail, Four-dimensional electron microscopy., *Science*. 328 (2010) 187–93. doi:10.1126/science.1166135.
- [11] B. Barwick, H. Soon Park, O.-H. Kwon, J.S. Baskin, A.H. Zewail, 4D Imaging of Transient Structures and Morphologies in Ultrafast Electron Microscopy, *Science*. 369 (2008) 1227–1232. doi:10.1007/978-1-59745-294-6.
- [12] V.A. Lobastov, R. Srinivasan, A.H. Zewail, Four-dimensional ultrafast electron microscopy., *Proc. Natl. Acad. Sci. U. S. A.* 102 (2005) 7069–73. doi:10.1073/pnas.0502607102.
- [13] P. Hommelhoff, C. Kealhofer, M.A. Kasevich, Ultrafast Electron Pulses from a Tungsten Tip Triggered by Low-Power Femtosecond Laser Pulses, *Phys. Rev. Lett.* 97 (2006) 247402. doi:10.1103/PhysRevLett.97.247402.
- [14] D.-S. Yang, O.F. Mohammed, A.H. Zewail, Scanning ultrafast electron microscopy., *Proc. Natl. Acad. Sci. U. S. A.* 107 (2010) 14993–8. doi:10.1073/pnas.1009321107.

- [15] B. Cook, P. Kruit, Coulomb interactions in sharp tip pulsed photo field emitters, *Appl. Phys. Lett.* 109 (2016) 151901. doi:10.1063/1.4963783.
- [16] A. Feist, N. Bach, N. Rubiano da Silva, T. Danz, M. Möller, K.E. Priebe, T. Domröse, J.G. Gatzmann, S. Rost, J. Schauss, S. Strauch, R. Bormann, M. Sivis, S. Schäfer, C. Ropers, Ultrafast transmission electron microscopy using a laser-driven field emitter: Femtosecond resolution with a high coherence electron beam, *Ultramicroscopy*. 176 (2017) 63–73. doi:10.1016/j.ultramic.2016.12.005.
- [17] D. Ehberger, J. Hammer, M. Eisele, M. Krüger, J. Noe, A. Högele, P. Hommelhoff, Highly coherent electron beam from a laser-triggered tungsten needle tip, (2014) 1–7. <http://arxiv.org/abs/1412.4584v1> (accessed December 16, 2014).
- [18] L.C. Oldfield, A rotationally symmetric electron beam chopper for picosecond pulses, *J. Phys. E.* 9 (1976) 455–463. doi:10.1088/0022-3735/9/6/011.
- [19] T. Hosokawa, H. Fujioka, K. Ura, Generation and measurement of subpicosecond electron beam pulses., *Rev. Sci. Instrum.* 49 (1978) 624. doi:10.1063/1.1135464.
- [20] K. Ura, H. Fujioka, T. Hosokawa, Picosecond Pulse Stroboscopic Scanning Electron Microscope, *J. Electron Microsc. (Tokyo)*. 27 (1978) 247–252.
- [21] M. Brunner, D. Winkler, B. Lischke, Electron-Beam Test System for High-speed Devices, 9 (1987) 201–204.
- [22] A.C. Lassise, *Miniaturized RF Technology for Femtosecond Electron Microscopy*, Eindhoven University of Technology, 2012.
- [23] J.F.M. van Rens, W. Verhoeven, J.G.H. Franssen, A.C. Lassise, X.F.D. Stragier, E.R. Kieft, P.H.A. Mutsaers, O.J. Luiten, Theory and particle tracking simulations of resonant, radio frequency cavities in TM₁₁₀ mode as dynamic electron-optical elements for ultrafast electron microscopy, *ArXiv*. (2017). <http://arxiv.org/abs/1707.08835>.
- [24] W. Verhoeven, J.F.M. van Rens, E.R. Kieft, P.H.A. Mutsaers, O.J. Luiten, High quality ultrafast transmission electron microscopy using resonant microwave cavities, *ArXiv*. (2017).
- [25] G.J.H. Brussaard, A. Lassise, P.L.E.M. Pasmans, P.H.A. Mutsaers, M.J. van der Wiel, O.J. Luiten, Direct measurement of synchronization between femtosecond laser pulses and a 3 GHz radio frequency electric field inside a resonant cavity, *Appl. Phys. Lett.* 103 (2013) 141105. doi:10.1063/1.4823590.
- [26] A. Gliserin, M. Walbran, P. Baum, Passive optical enhancement of laser-microwave synchronization, *Appl. Phys. Lett.* 103 (2013) 1–5. doi:10.1063/1.4815929.
- [27] P. Kruit, I.G.C. Weppelman, Device and method for generating charged particle beam pulses, WO2016076718 A3, 2016.
- [28] J.T.L. Thong, Picosecond electron pulse generation via beam deflection-chopping in the

- SEM, *Meas. Sci. Technol.* (1991) 207–216.
- [29] D.H. Auston, P. Lavallard, N. Sol, D. Kaplan, An amorphous silicon photodetector for picosecond pulses, *Appl. Phys. Lett.* 36 (1980) 66. doi:10.1063/1.91276.
- [30] T. Motet, J. Nees, S. Williamson, G. Mourou, 1.4 ps rise-time high-voltage photoconductive switching, *Appl. Phys. Lett.* 59 (1991) 1455–1457.
- [31] Y. Chiu, S.B. Fleischer, D. Lasaosa, J.E. Bowers, Ultrafast (370 GHz bandwidth) using low-temperature-grown GaAs p-i-n traveling wave photodetector using low-temperature-grown GaAs, *Appl. Phys. Lett.* 71 (1997) 2508–2510. doi:10.1063/1.120115.
- [32] C.A. Schmuttenmaer, Exploring dynamics in the far-infrared with terahertz spectroscopy, *Chem. Rev.* 104 (2004) 1759–1779. doi:10.1021/cr020685g.
- [33] G.H. Kassier, K. Haupt, N. Erasmus, E.G. Rohwer, H.M. Von Bergmann, H. Schwoerer, S.M.M. Coelho, F.D. Auret, A compact streak camera for 150 fs time resolved measurement of bright pulses in ultrafast electron diffraction, *Rev. Sci. Instrum.* 81 (2010). doi:10.1063/1.3489118.
- [34] J. Feng, H.J. Shin, J.R. Nasiatka, W. Wan, A.T. Young, G. Huang, A. Comin, J. Byrd, H.A. Padmore, An x-ray streak camera with high spatio-temporal resolution, *Appl. Phys. Lett.* 91 (2007) 134102. doi:10.1063/1.2793191.
- [35] A.M. Johnson, D.H. Auston, P.R. Smith, J.C. Bean, J.P. Harbison, A.C. Adams, Picosecond transient photocurrents in amorphous silicon, *Phys. Rev. B.* 23 (1981) 6816–6819. doi:https://doi.org/10.1103/PhysRevB.23.6816.
- [36] M.C. Beard, G.M. Turner, C.A. Schmuttenmaer, Subpicosecond carrier dynamics in low-temperature grown GaAs as measured by time-resolved terahertz spectroscopy, *J. Appl. Phys.* 90 (2001) 5915. doi:10.1063/1.1416140.
- [37] P.U. Jepsen, R.H. Jacobsen, S.R. Keiding, Generation and detection of terahertz pulses from biased semiconductor antennas, *J. Opt. Soc. Am. B.* 13 (1996) 2424. doi:10.1364/JOSAB.13.002424.
- [38] A. V. Kuznetsov, C.J. Stanton, Ultrafast optical generation of carriers in a dc electric field: Transient localization and photocurrent, *Phys. Rev. B.* 48 (1993) 10828–10845.
- [39] B.B. Hu, A.S. Weling, D.H. Auston, A. V. Kuznetsov, C.J. Stanton, dc-electric-field dependence of THz radiation induced by femtosecond optical excitation of bulk GaAs, *Phys. Rev. B.* 49 (1994) 2234–2237.
- [40] H. Neumeier, A. Pashkin, P. Kuznetsov, M. Khazan, S. Schnuor, I. Wilke, Carrier dynamics in low-temperature grown GaAs studied by terahertz emission spectroscopy, *J. Appl. Phys.* 90 (2001) 1303–1306. doi:10.1063/1.1380414.
- [41] J. Požela, A. Reklaitis, Electron transport properties in GaAs at high electric fields, *Solid. State. Electron.* 23 (1980) 927–933. doi:10.1016/0038-1101(80)90057-X.

- [42] P. Kruit, M. Bezuijen, J.E. Barth, Source brightness and useful beam current of carbon nanotubes and other very small emitters, *J. Appl. Phys.* 99 (2006). doi:10.1063/1.2162270.
- [43] H. Nyquist, Thermal agitation of electric charge in conductors, *Phys. Rev.* 32 (1928) 110–113. doi:10.1103/PhysRev.32.110.
- [44] R. Sarpeshkar, T. Delbruck, C.A. Mead, White Noise in MOS Transistors and Resistors, *IEEE Circuits Devices Mag.* 9 (1993) 23–29. doi:10.1109/101.261888.
- [45] A.H. V. van Veen, C.W. Hagen, J.E. Barth, P. Kruit, Reduced brightness of the ZrO/W Schottky electron emitter, *J. Vac. Sci. Technol. B Microelectron. Nanom. Struct.* 19 (2001) 2038. doi:10.1116/1.1409390.
- [46] A. Lassise, P.H.A. Mutsaers, O.J. Luiten, Compact, low power radio frequency cavity for femtosecond electron microscopy., *Rev. Sci. Instrum.* 83 (2012) 043705. doi:10.1063/1.3703314.
- [47] W. Verhoeven, J.F.M. van Rens, M.A.W. van Nindhuijs, W.F. Toonen, E.R. Kieft, P.H.A. Mutsaers, O.J. Luiten, Time-of-flight electron energy loss spectroscopy using TM110 deflection cavities, *Struct. Dyn.* 3 (2016) 054303. doi:10.1063/1.4962698.
- [48] R.J. Moerland, I.G.C. Weppelman, W.H. Garming, P. Kruit, J.P. Hoogenboom, Time-resolved cathodoluminescence microscopy with sub-nanosecond beam blanking for direct evaluation of the local density of states, *Opt. Express.* 24 (2016) 499–504.
- [49] K.R. Demarest, *Engineering Electromagnetics*, Prentice Hall, 1998.

4 Pulse length, energy spread, and temporal evolution of electron pulses generated with an ultrafast beam blanker

This chapter is published in Structural Dynamics.¹

Ultrafast Electron Microscopy (UEM) is an emerging field of research where the aim is to image structural dynamics at ultrafast time scales with high spatial resolution. Both imaging and diffraction modes, as well as Electron Energy Loss Spectroscopy (EELS), can be used in UEM to study ultrafast dynamics in materials.²⁻⁴ UEM systems have also enabled the study of quantum mechanical interactions between photons and electrons.⁵ For all these applications it is important to generate high brightness electron pulses as the brightness directly determines the amount of current that can be used to illuminate the sample with a particular beam opening angle. High brightness ultrafast electron pulses, with peak brightness comparable to Schottky emitters, can be created using laser pulse illumination of a sharp metal tip⁶ or alternatively by using a microwave cavity to chop a continuous electron beam.⁷ The latter method has been implemented in a Transmission Electron Microscope (TEM) and both numerical calculations and experimental measurements have shown the conservation of beam emittance.^{8,9} Both laser source illumination and insertion of a microwave cavity may require extensive modification of the electron microscope column.

In the previous Chapter 3 an alternative concept for obtaining short electron pulses is presented, which relies on the integration of an electrostatic beam blanker with a photoconductive switch in a single device made with MEMS technology.^{10,11} Such an ultrafast blanker (UFB) could be inserted into the column of an existing electron microscope, thus allowing to rapidly alternate between static DC operation and time-resolved imaging using electron pulses. Based on back-of-the-envelope calculations, simplified models, and reported experimental performance of photoconductive Auston switches, we argued in Chapter 3 that with a MEMS-sized UFB it should be possible to create electron pulses of about 100 fs focused in a 10 nm spot at an acceleration voltage of 30 kV. Chapter 3 also describes calculations that the time-response of an UFB would be critically influenced by the capacitance of the deflector electrode.¹¹ This capacitance is difficult to estimate with analytical equations and challenging to measure experimentally. Also, it is difficult to incorporate the full response of a photoconductive switch and thus the temporal dynamics of the blanking voltage in an analytical model, while this may influence the achievable brightness (or emittance) and the energy spread in the pulse. Both brightness and energy spread are important to evaluate as brightness determines the obtainable current and the energy spread is important for the reason that chromatic aberrations cause a decrease in spatial resolution limit the spectral resolution in EELS measurements. For UEM, energy spread is also important as it causes a temporal broadening when the pulse travels from blanker to sample.

Fowler and Good have shown that in general creating electron pulses by chopping a continuous beam may reduce the beam quality.¹² Equations describing the energy spread induced by a blanker have been derived by Thong for different blanker configurations, such as conjugate blanking and sweeping a focused beam over a blanking aperture.¹³ Thong concluded that, to first order, a conjugate blanker does not introduce any additional energy spread. Oldfield analysed the beam quality for a combination of two cavities where the first is

used for chopping the beam and the second for correcting the induced energy spread.¹⁴ Further analyses of conjugate beam blanking using magnetic deflection fields inside a resonant radio frequency field (RF) cavity has been performed by Lassise and van Rens.^{8,15,16} They showed that their RF blanker will introduce negligible energy spreads for 100 fs electron pulses at 30 keV beam energies. This system has now been incorporated in a TEM.⁹ A MEMS sized electrostatic beam blanker driven by sinusoidal RF fields has been analysed by Cook. He found that such a blanker introduced a negligible increase in emittance and energy spread apart from a 1.7 eV constant energy gain for 400 fs electron pulses.¹⁷ Our MEMS-sized UFB controlled by a photoconductive switch is significantly smaller and uses a broadband deflection field with frequencies up to the terahertz range. Recently experiments have been performed demonstrating the possibility of Terahertz fields to control electron pulses and to measure Terahertz fields by respectively Kealhofer *et al.* and Ryabov *et al.*^{18,19} The potential emittance growth and energy spread introduced by such deflection fields in a MEMS device have so far not been addressed. In this chapter, we present time-dependent, three-dimensional numerical simulations to better evaluate the time-dependent deflection fields inside the UFB and thus the influence of the UFB on the quality of the electron pulses. In order to perform such simulations, a model of the time-dependent conductivity of an Auston switch is required, which is also discussed below. This model can then be used to calculate the response of the photoconductive switch under illumination of a laser pulse and, in combination with Maxwell's equations, be used to numerically evaluate the time-dependent deflection fields in and around the UFB

4.1. Simulation setup, model and approximations

First, we briefly review the UFB concept, which has been described in full detail in Chapter 3.¹⁰ The beam blanker consist of two plates, one grounded and the other connected to an photoconductive switch as indicated in Figure 4.1, called the deflector plate. The other electrode of the photoconductive switch is connected to an electrical circuit delivering a voltage, called the feed plate. The beam blanker is integrated with a photo switch in a single micrometers scaled device. The photoconductive switch is activated by a femtosecond laser pulse that creates free carriers in the semiconductor material resulting in a current due to the bias field over the switch. This current is used to (de)charge the deflector plate of the beam blanker, hence in a short time scale the deflection field in the blanker will be inverted. A DC electron beam propagating between the blanker plates will sweep over an aperture and an ultrafast electron pulse is created below this blanking aperture. Numerical simulations are conducted using Comsol Multiphysics modeling software.

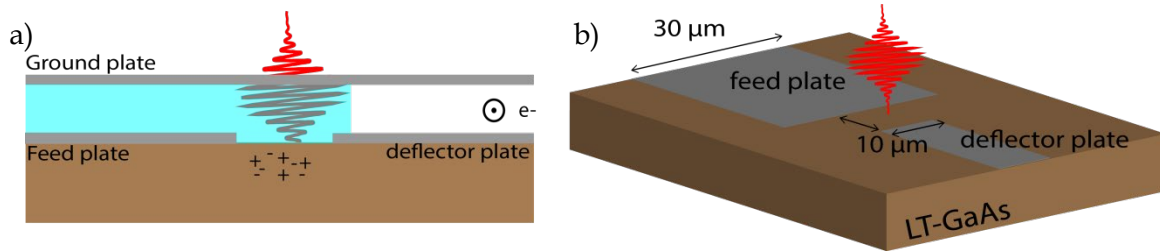


Figure 4.1: Sketch of UFB with a photo switch located between the feed and deflector plate of the blanker. The electron beam propagates between the ground plate and deflector plate perpendicular to this plane as indicated. A glass layer indicated in light blue separates ground plate from the feed plate. (b) Side view of (a) with the ground plate removed and typical dimensions indicated.

Figure 4.2 shows how the UFB design was implemented in Comsol Multiphysics, where we used a half symmetry to reduce the calculation time and memory space required.

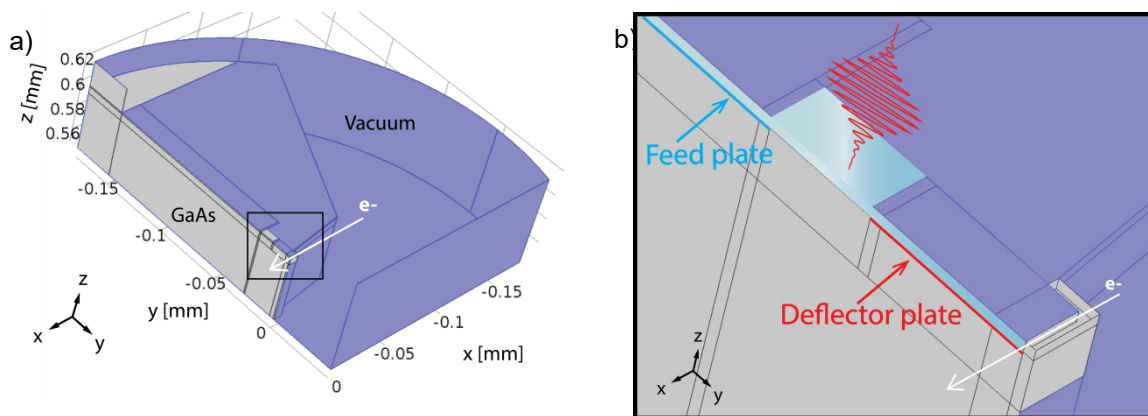


Figure 4.2 UFB simulation geometry. (a) A half pillbox is used, the fields are symmetrical at the flat (left) side and the electrons will elastically reflect from the symmetry boundary. All blue plates are electrically grounded perfect metals, and hence are reflecting boundaries for the time-dependent simulation. The white arrow shows the propagation direction of the electron beam along the x -direction. (b) Zoom in at the position of the photo switch and blanker (indicated with a black square in (a)). The deflector plate is indicated with a red line and the feed plate with a blue line. The electron beam is deflected due to the voltage difference between the deflector plate and ground. In light blue the glass layer is indicated which separates the ground plates and the electrodes, an opening in the ground plate is present such that the laser pulse can illuminate the photoconductive switch.

The simulation of the UFB and photoconductive switch consists of three steps. First we calculate the electrostatic potential in the whole domain. A Poisson solver is used to calculate the electrostatic potential and the photoconductive switch is assumed to be a perfect electrical insulator. The voltage of the feed plate and the deflector plate are -10 V and $+10$ V respectively. A relative permittivity of 12.25 is assumed for GaAs and a permittivity of 2.25 is used for the SiO_2 layer that separates the ground plate and deflector/feed plates.

The calculated surface charge density on the deflector plate is used to determine the capacitance of the deflector plate. We found that a $15 \mu\text{m}$ long deflector plate results in a desired capacitance of 6.6 fF: a factor of 2 higher than expected according to our previous back-

of-the-envelope calculation shown in Chapter 3 and Weppelman *et al.*¹¹, which assumed a parallel plate capacitor. We attribute this to the fact that the high permittivity GaAs supporting the capacitor is not included in the parallel plate capacitor model. Also, parasitic capacitances and the complicated geometry around the deflector were not taken into account in the simplified model.

The calculated potential is then used as an initial condition in the second step for the full (time-dependent) transient Maxwell solver. Hereto, a time-dependent conductivity is required for the photoconductive switch. In the subsequent section we explain the calculation of the conductivity of the photoconductive switch. Then, the last step is to trace electrons through the time-dependent electromagnetic fields.

4.2. Model for the time-dependent conductivity of the photoconductive switch

The laser illumination creates free carriers (electrons and holes) in the photoconductive switch which are subsequently accelerated due to the electric field applied over the switch. In the model we only consider free electrons, which have the dominant contribution to the conductivity. The reason is that the effective mass of electrons is an order of magnitude lower than of holes in GaAs.²⁰ The relation between the conductivity, electric field and current density is linear:

$$j = \sigma E \quad (4.1)$$

The current density is equal to:

$$j = n(t)e\langle v(t) \rangle \quad (4.2)$$

where $n(t)$ is the density of free carriers as function of time, generated by the laser pulse and $\langle v \rangle$ is the average drift velocity of free electrons.

The average drift velocity is described in each mesh point by the following equation, based on a Drude-Lorentz model:

$$\frac{d\langle v \rangle}{dt} = -\frac{\langle v \rangle}{\tau_s} + \frac{e}{m^*} |E(t)| \text{sign}(E_y(t)) - \langle v \rangle \frac{G(\mathbf{x}, t)}{n(\mathbf{x}, t)} \quad (4.3)$$

where $E(t)$ is the local electric field, E_y is the field in y -direction as defined in

Figure 4.2, $n(x, t)$ is the density of free carriers as function of time and space, $G(x, t)$ is the time derivative of $n(x, t)$, i.e. the generation rate of new free electrons. The scattering time, τ_s , is estimated to be 30 fs and the effective mass, m^* is equal to 0.067 times the rest mass of an electron.²¹ Drude-Lorentz models are often successfully used in the literature to describe the dynamics of charges in Auston switches, for example by Jepsen²¹ *et al.*, Piao²² *et al.* and Duvillaret²³ *et al.*

Free electrons will be displaced over a typical distance of 100 nm in a timescale of 1 ps, based on a maximum drift velocity of $1 \cdot 10^5$ m/s that we also used in our previous work.¹¹ Spatial diffusion can be neglected in equation (4.3) because the displacement is smaller than both the mesh size and electromagnetic wavelengths. In the numerical calculation screening of the electric field in the photoconductive switch due to charge separation and coulomb interactions between the holes and electrons is neglected. According to literature this is a reasonable assumption as long as the carrier density is below 10^{18} cm⁻³.^{21,22}

The density of free carriers, $n(x, t)$, follows the time integral of the laser pulse, $G(x, t)$, which has a Gaussian temporal envelope and is equal to:

$$n(\mathbf{x}, t) = \frac{1}{2} n_i \left(1 + \operatorname{erf} \left(t / 1.67 \tau \right) \right) g(x, y, z) \quad (4.4)$$

where n_i is the total density of generated free carriers, $g(x, y, z)$ is the spatial variation of the laser intensity and τ the FWHM of the laser pulse. Recombination of electron-hole pairs is not taken into account because the recombination time is in the order of 10 to 15 ps, much longer than the time scales relevant in the simulation.

The z -dependence of the function $g(x, y, z)$ in equation (4.4) takes into account that deeper into the GaAs less charges are generated due to the absorption of light in GaAs, as described by a Lambert-Beer model:

$$I(z) = I_0 \exp(-4\pi k z / \lambda) \approx I_0 \exp(-z / \lambda) \quad (4.5)$$

where k is the imaginary part of the index of refraction, in case of GaAs equal to 0.089 at 800 nm.²⁴ Underneath the electrodes the laser intensity is lower, we use a rough approximation by simply assuming a homogenous laser intensity illuminating the photoconductive switch and linear decreasing field under the metal, as depicted in Figure 4.3. To verify the linear model we compared it with the laser intensity calculated with Lumerical, a commercial finite difference time domain (FDTD) solver of Maxwell's equations. In this simulation a plane wave is injected just above the ground plate propagating towards the GaAs layer. The contact layers are modelled as Molybdenum plates with a thickness of 30 nm, the optical constants are taken from Ordal *et al.*²⁵ As depicted in Figure 4.3b, the FDTD calculation confirms that the linear model of the laser intensity will give conservative estimations of the photoconductivity around the contact electrodes. Note that a very basic design for the electrodes is assumed for the calculation, more advanced electrodes with significant improvements in terms of photocurrent have been demonstrated in the literature, see for example the review paper of Lepehov *et al.* and references therein.²⁶

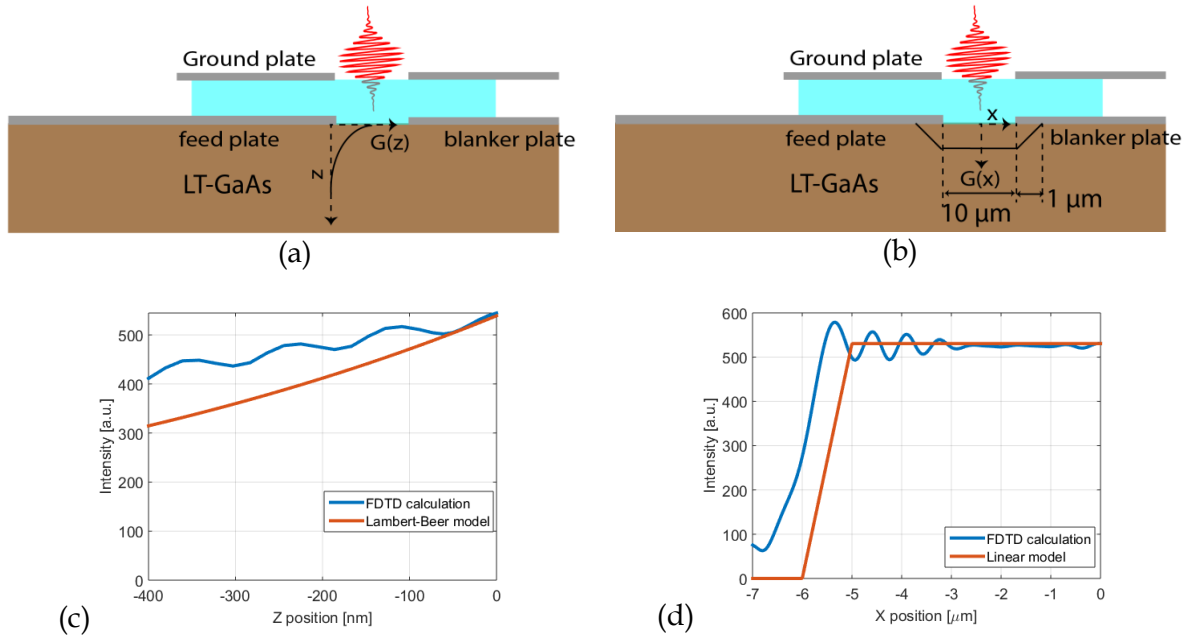


Figure 4.3: In our computational model, we use (a) an exponential decay of the intensity of the laser in the z -direction according to Lambert-Beer, and (b) a linear variation of the laser intensity in the y -direction. (c) FDTD calculation (blue line) of the laser intensity as function of z position in the GaAs at the center of the photoconductive switch. The glass-GaAs interface is located at $z = 0$. The red line is the laser intensity used in the calculation in Comsol. (d) FDTD calculation of the laser intensity as function of x at a depth of 10 nm below the glass-GaAs interface. The red line is the laser intensity assumed in the Comsol calculation. A broadband p -polarized plane wave located above the ground plate is injected in the FDTD simulation, the resulting laser intensity is integrated over a range from 750 to 850 nm.

The conductivity can be calculated by solving the ordinary differential equation (4.3):

$$\sigma = \langle \mathbf{v} \rangle n e / |E| \quad (4.6)$$

Note that the conductivity is dependent on the field and in turn the field is dependent on the conductivity. Therefore the conductivity and Maxwell's equations are solved in an iterative loop, which does increase the CPU resources required for the simulation.

The calculation time can be reduced by assuming that the electric field over the switch is only slowly varying in time compared to the time it takes for the electrons to accelerate to the drift velocity. In that case the conductivity of the photoconductive switch can be modelled as the convolution of the laser pulse and the velocity response of the carriers based on a Drude-Lorentz model assuming a constant electric field:

$$\sigma(t) = \frac{en(t)v(t)}{E} = \frac{e}{E} \int_{-\infty}^{\infty} G(t-t')v(t')dt' = \frac{e^2}{m^*} \int_{-\infty}^{\infty} \left(1 - e^{-\frac{t-t'}{\tau_s}}\right) G(t-t')dt' \quad (4.7)$$

The model of the time-dependent conductivity of the Auston switch, equation (4.7), is used to calculate the time-dependent electric field in the blanker, as shown in Figure 4.4b. The electric field between the two deflector plates inverts on a time scale of about 500 fs. As shown in

Figure 4.4, a time delay of about 200-400 fs is present between the conductivity built-up and the moment when the deflection field starts to change. This is caused by propagation delays over the 15 μm long deflector plate.

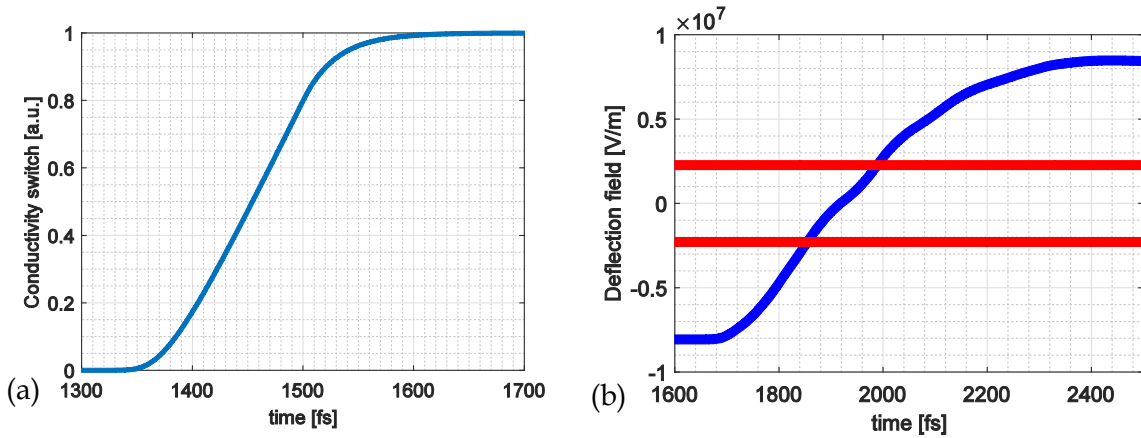


Figure 4.4: (a) Conductivity of the photoconductive switch versus time calculated using equation (4.7) assuming a 25 fs Gaussian short laser pulse. The conductivity is used to calculate (b) the deflection field in the blanker as a function of time. In the area between the red lines the electron beam can partially pass the blanking aperture that accepts an half opening angle of 0.4 mrad.

The assumption of a relatively slowly varying electric field over the switch is valid for low laser powers because both models give a comparable result, as shown in Figure 4.5. The time-dependent deflection field is shifted by about 100 fs for the full Drude-Lorentz model, however this can be compensated by adjusting the path length of the laser pulse used to illuminate the photoconductive switch.

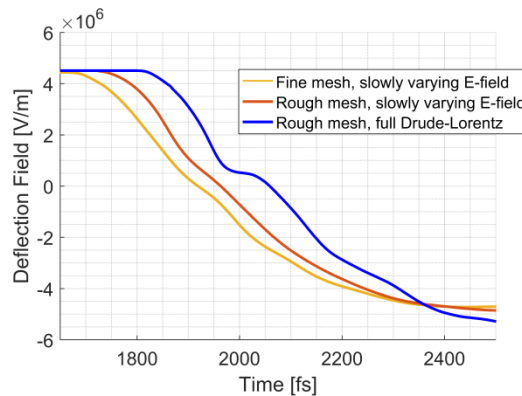


Figure 4.5: Deflection field versus time for the mesh and conductivity model as used in Figure 4.4 (yellow line). A coarser mesh using the same conductivity model, gives essentially the same time-dependence for the deflection field (red line). With the same coarse mesh and the Drude-Lorentz as described by equation (4.3) also a similar time-dependence is obtained (blue line).

All electrodes are assumed to be perfect electrical conductors with zero thickness. Absorption and dispersion in the semiconductor are assumed to be negligible because the length of the deflector plate is small. The permittivity of GaAs varies only slightly from DC to THz frequencies, up to the point where the frequency approaches a phonon resonance, located around 8 THz.²⁰

Around the phonon resonance the real and imaginary part of the permittivity vary significantly. To check the contribution of these frequencies to the deflection field, we filtered the data with a Butterworth first order low pass filter, shown in Figure 4.6. We observe no change in the amount of time required to invert the deflection field in the deflector and thus conclude that it is reasonable to neglect the absorption due to the phonon resonance.

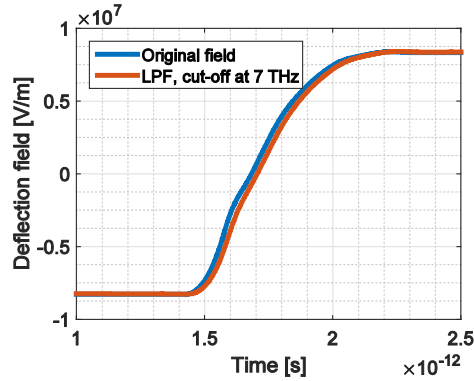


Figure 4.6: Deflection field as function of time, the blue curve is the original data and the red curve is the filtered data. The field is filtered with a first order Butterworth filter with a cut-off frequency of 7 THz to evaluate the influence of GaAs permittivity changes around the phonon resonance.

4.3. Particle tracing of the electron beam and beam quality

In the previous section we calculated the time-dependent electromagnetic fields, in this section we use this field to trace electrons through the blanker. This enables us to calculate the electron pulse length as well as potential blurring and energy spread increase in the beam.

The particle tracing module of COMSOL is used to calculate the trajectory of the electrons using Newton's second law. The Lorentz force acting on the electrons is calculated from the time-dependent magnetic and electric fields. Interaction between the particles and fields induced by the moving electrons are neglected.

The FW50 spot size of a 4 nA electron beam will be 50 nm in the UFB for a realistic half opening angle of 0.4 mrad at 30 keV, a 16 nA will have a FW50 spot size of 100 nm. A reduced brightness of $5 \cdot 10^7$ A/(m²·V·sr²) is assumed, typical for a Schottky electron source, and an acceleration voltage of 28.5 kV. A Schottky source can have, and a cold field emitter does have, higher values for the reduced brightness as shown by van Veen *et. al.* and others.²⁷⁻²⁹ In the simulation we want to include a broader part of the beam than only FW50, so we take a 200 nm focused electron beam spot in between the blanker plates with a half opening angle of 0.4 mrad. Every 10 fs a bunch of 51 electrons is injected in the simulation, to determine the amount blur induced by the deflector, in practice an ultrafast electron pulse cannot have more than 0.5 electrons per pulse otherwise statistical electron interactions will reduce the brightness and increase the energy spread. The result of the particle tracing calculations is shown in Figure 4.7.

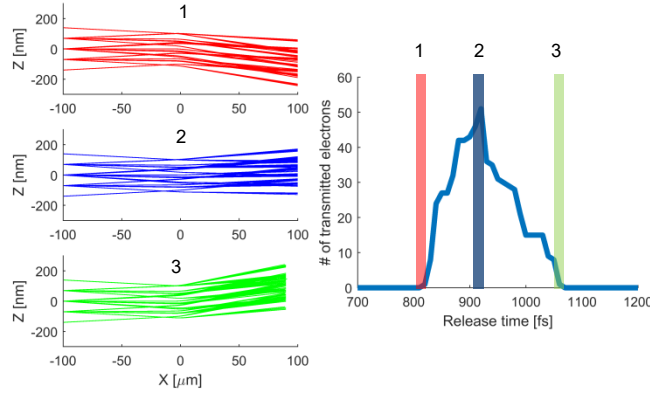


Figure 4.7: (1-3) Distance to the electron optical axis as function of position along the optical axis for release times of (1) 820 fs (2) 960 fs and (3) 1090 fs. The electrons are injected at $x = -100 \mu\text{m}$ with a velocity of $1 \cdot 10^8 \text{ m/s}$ and are converging to a 200 nm crossover between the deflector plates located at $x = 0 \mu\text{m}$. The colors of the rays indicate the different release times, in the right panel, which shows the amount of electrons transmitted through the blanker aperture as function of release time. An electron is transmitted through the aperture when the exit angle is smaller than the half-opening angle of the beam. In the simulations, a bunch of electrons is injected every 10 fs.

The loss of brightness or blurring of the beam is analyzed by tracing the electron trajectories in a linear fashion back from the final position in the simulation to the beam blanker. We performed this analysis for two situations, one where the deflection field goes from positive to negative and the inverted case, see Figure 4.8. The mesh size for this simulation is equal to ‘Simulation 1’, defined in Appendix A. In all cases a focus is created at the beam blanker with a beam displacement less than a couple of nanometers. This clearly shows that the increase of emittance can be neglected. We expect such a result for the reason that the residence time of electrons in the deflector is short, so the beam displacement is very small.

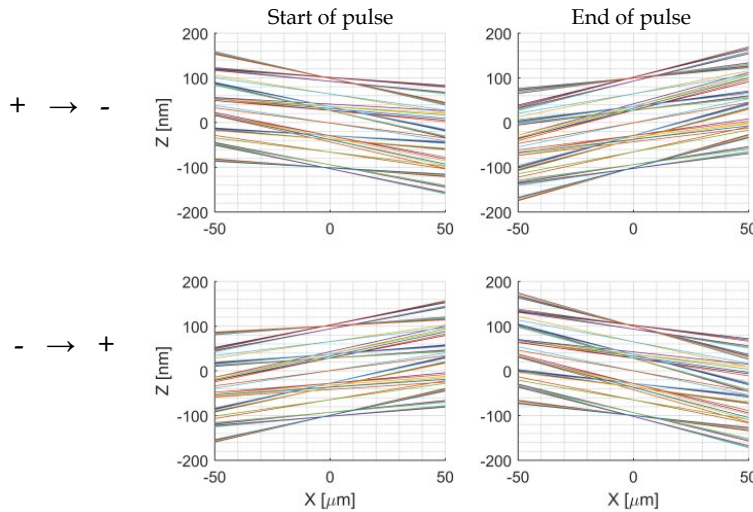


Figure 4.8: Distance to the electron optical axis as function of position calculated by geometrically tracing back the electron trajectories. The top row shows the rays when the field sweeps from positive to negative and the bottom row shows the rays when the field sweeps from negative to positive. The left column shows the trajectories just before the first electrons are transmitted through the aperture and the right column the trajectories just after the last electrons transmitted through the aperture. The blanker is located at $x = 0 \mu\text{m}$, the blur at all these positions is less than 5 nm.

For each electron, the amount of deflection depends on the arrival time of the electron in the deflector with respect to the time dependent electric field, the residence time of the electron in the deflector, and the rate of change of the field in the deflector. The net effect is that electrons

in the front of the electron pulse have a different deflection angle when exciting the deflector than electrons in the back of the pulse. The net effect is a blur as the pulse seems to originate from different points in the conjugate image plane in the deflector. This blur is analytically estimated by calculating the equation of motion of an electron through the deflector and by considering the exponentially time varying field in the deflector as a simple linear ramp in field. The position and deflection of an electron in the back and front of a pulse is used to trace back where they appear to come from. This results in the following analytical equation, derived with the aid of Maple:

$$y = \frac{qEL^3\tau_e}{24\phi\sqrt{\frac{2q\phi}{m}\tau_f^2}} \quad (4.8)$$

where τ_e is the electron pulse length, τ_f is the time constant of the exponentially rising field in the deflector, E is the maximum electric field, ϕ is the beam acceleration voltage, L is the length over which the electron travels through the deflector. For the MEMS UFB the blur will be equal to 0.3 nm, which will be a sub angstrom contribution to the probe size in the sample plane and can be neglected.

4.4. Energy gain introduced by the blanker

An electron approaching a static deflector will be accelerated and, when leaving the deflector, going to infinity, it will be decelerated back to its initial kinetic energy because the field is conservative. However, as in the UFB the voltage at the deflector is modulated in time, an electron can acquire a net energy gain or loss. The net energy gain or loss in the deflector, ΔE , is deterministically dependent on the position and injection time of the electron. The electron beam is monochromatic in the numerical calculation, hence in reality the results should be convoluted with the 0.6 eV FW50 energy spread of a Schottky source, or the 0.3 eV of a cold field emitter.³⁰

Figure 4.9a shows an ‘open’ design of the UFB and Figure 4.9c shows the energy gain of an electron travelling through such an ‘open’ blanker as a function of both release time and position along the electron optical axis. The energy gain in this case is several electron volts. This relatively large energy gain is caused by the fringe fields around the deflector which increase the effective length of the deflector. We suppress this effect with a ‘tunnel-type’ UFB where the deflector electrode is encapsulated with ground plates to reduce the spatial extent of the fringe fields (Figure 4.9b). The effect on the energy gain in the tunnel-type UFB is shown in Figure 4.9d. The tunnel-type UFB also has a lower potential at the optical axis, only 3.7 V, which further helps to reduce the energy gain.

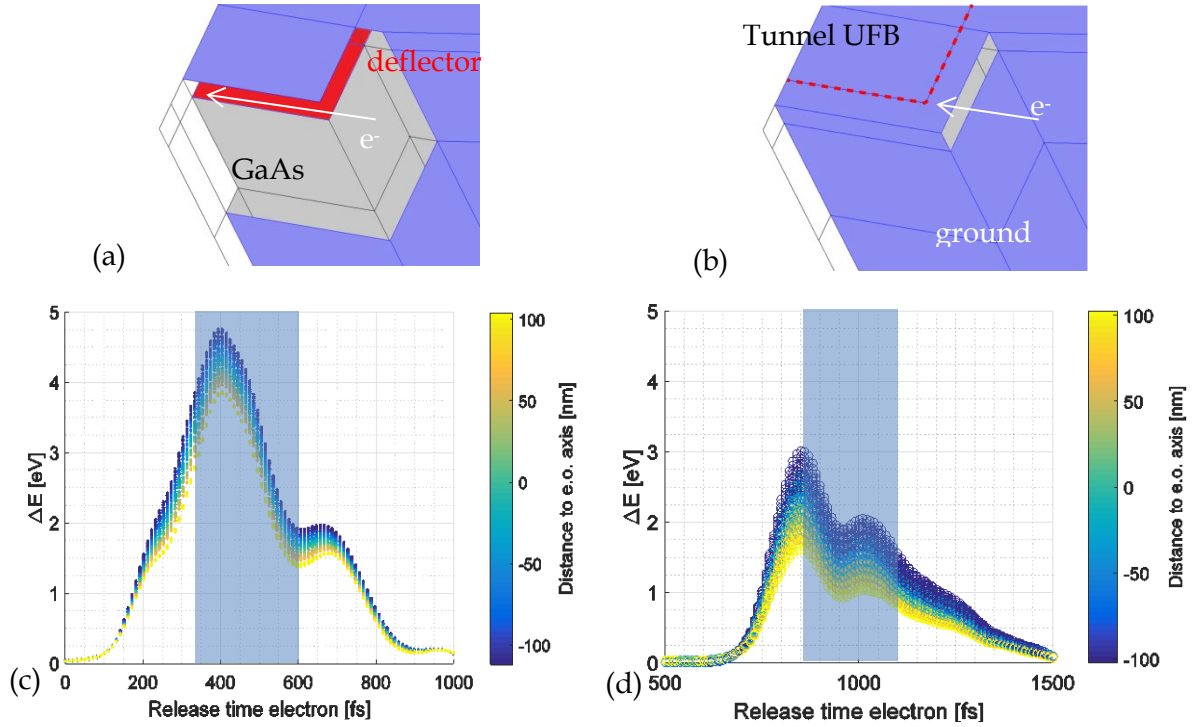


Figure 4.9. (a) Schematic indication of an open type design of the UFB. (b) Same for a tunnel type design where fringe fields outside the blanker are shielded by the encapsulation. The red dashed line in the tunnel-type UFB indicates the contour of the deflector plate. (c, d) Energy gain of an electron as a function of release time in the simulation for (c) open design and (d) tunnel-type design. The color indicates the z position of the electron in the crossover, negative z values are closer to the deflector plate. The z -range of the electron trajectories varies from -100 nm to $+100$ nm from the optical axis, the total distance between the deflector plates is $1\ \mu\text{m}$. The voltage at the deflector plate inverted from $+10$ V to -10 V, hence all electrons have some net energy gain. Electrons released between $t = 310$ fs and $t = 570$ fs are transmitted through the blanker aperture if it is located on the electron optical axis and accepts an half opening angle of 0.4 mrad, this region is marked in blue in the graph.

As shown in Figure 4.9 the energy gain is in the range of several electron volts. Electrons with the same release time also have an energy dispersion, depending on their trajectory through the beam blanker. Trajectories closer to the deflector plate result in higher energy gain because the potential difference between entrance and exit of the deflector is higher. This effect can be minimized by reducing the probe size in the blanker. It also shows the importance of the (mechanical) stability of the UFB with respect to the electron optical axis. If the UFB is vibrating with an amplitude of about 100 nm the energy spread of the electron beam will be noticeably increased. The same holds when the vibration amplitude of source multiplied with the magnification is on the order of 100 nm.

We note that electrons acquire on average ± 4 eV energy for the open UFB design, with the sign depending on whether the voltage flips from positive to negative or the inverse. Hence, due to chromatic aberrations of the lens, two spots will be visible in the image plane. For a final lens with a $C_c = 10$ mm and an half opening angle of 5 mrad the two spots are separated by about 14 nm at 28.5 kV. An additional blanker might be used to pick up only the even or odd pulses in order to mitigate this effect. The effect could be further reduced by making a new design in which both deflector plates would be excited by opposite voltage pulses.

4.5. Estimation energy gain of the UFB

For a better understanding we will discuss analytical models to approximate the energy gain. This is useful because it allows to minimize the energy spread for a certain required peak current and electron pulse length.

The deflection of the electron beam is quite small and the energy gain is negligible compared to the total energy of the electron beam, hence we can assume a constant velocity and zero beam displacement. For this reason the energy gain can be estimated as follows:

$$\Delta E(t_0) = q \int_{-\infty}^{+\infty} E_x(x, t_0 + x/v) dx \quad (4.9)$$

where $E_x(x, t)$ is the electric field component along the electron optical axis as function of time and position, v is the velocity and t_0 is the release time of the electron in the simulation.

As a first estimation of the energy gain quasi-static electric fields are assumed. The term 'quasi-static' implies a potential that can be described as a product of a spatial function, $\varphi(\mathbf{x})$, and a temporal one, $f(t)$:

$$\phi(\mathbf{x}, t) = \varphi(\mathbf{x})f(t) \quad (4.10)$$

The quasi-static approximation is checked using our simulation data of the fields in combination with equation (4.9). For the spatial distribution $\varphi(\mathbf{x})$ we use the initial potential, $f(t)$ is approximated by using the normalized deflection field in the centre of the deflector. With this method, the quasi-static energy gain as a function of arrival time is calculated and compared with the energy gain calculated with equation (4.9) and using the full time-dependent fields. This enables us to check whether approximation of the fields as quasi-static is valid or not. The result is shown in Figure 4.10. For the tunnel UFB design the quasi-static approach provides an adequate approximation with a relative error smaller than 20% while for the open UFB design the deviation with the quasi-static approach can be substantial, up to a few eV. The tunnel-type design limits the spatial extent of the fringe fields so retardation effects in the potential are suppressed.

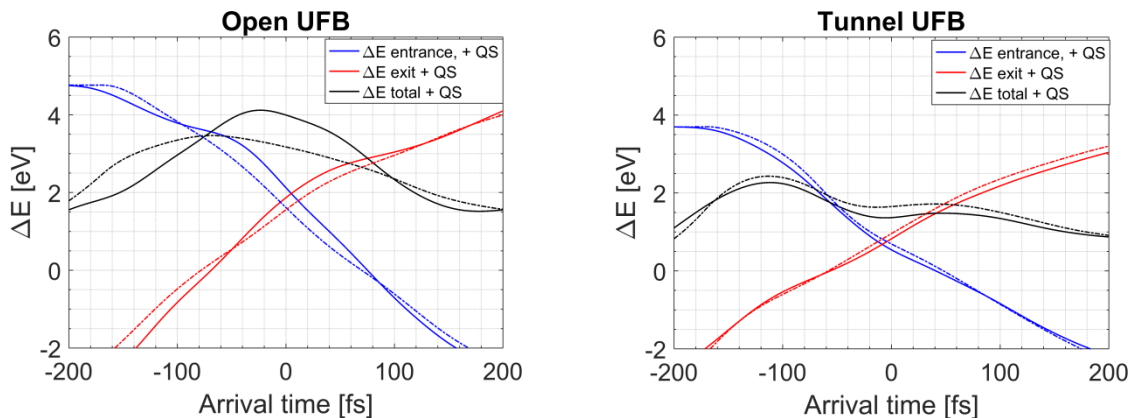


Figure 4.10: Energy gain as a function of electron arrival time in the UFB for (left panel) the open design and (right panel) the tunnel-type design. Solid lines indicate the total energy gain (black line), the energy gain when entering the deflector (blue line) and when leaving the deflector (red line). The dashed lines are the calculated energy gains when the fields are approximated as being quasi-static. (left) Calculated energy gain for the open design and (right) calculated energy gain for the tunnel design.

The energy gain is a function of arrival time and we are interested in an analytical expression for the energy gain. For the analytical approximation of the energy gain a description of the potential $\phi(x)$ and the time-dependent function $f(t)$ is required. The potential along the electron-optical axis is approximated with a square potential, see Figure 4.11.

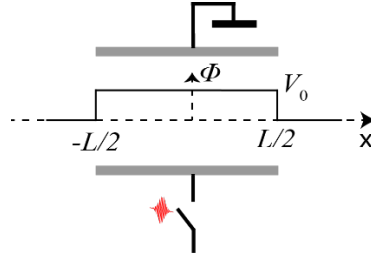


Figure 4.11: Potential, ϕ , along the electron optical axis, x . The potential has a square shape with an amplitude equal to V_0 , the deflector has a length equal to L .

The time-dependent function is described with a polynomial:

$$f(t + \tau) = \alpha_1 \left(\frac{x}{v} + \tau \right) + \alpha_2 \left(\frac{x}{v} + \tau \right)^2 + \alpha_3 \left(\frac{x}{v} + \tau \right)^3 + \dots \quad (4.11)$$

where τ is the arrival time of the electron in the deflector. Note that $f(t)$ is a dimensionless function, so the parameters a_1, a_2 , etc. have units of $[s^{-1}]$, $[s^{-2}]$, etc. Zeroth order terms are taken out of the polynomial because they do not affect the final energy. We calculated the energy gain for the different terms in the polynomial using equation (4.11) (see Appendix B):

$$\begin{aligned} \Delta E_1(\tau) &= V_0 \alpha_1 \frac{L}{v} \\ \Delta E_2(\tau) &= 2V_0 \alpha_2 \frac{L\tau}{v} \\ \Delta E_3(\tau) &= V_0 \alpha_3 \left(\frac{1}{4} \frac{L^3}{v^3} + \frac{3L\tau^2}{v} \right) \end{aligned} \quad (4.12)$$

The first term describes the fact that all electrons either gain or lose a constant amount of energy, depending on the sign of a_1 . The second term describes that the blanker is either compressing or expanding the electrons pulse, like a buncher. Whether the beam blanker expands or compresses the pulse depends on the sign of a_2 . This effect is known from the literature, Thong discussed that a parallel plate blanker acts as a buncher and that the bunching effect can be reduced substantially by using symmetrical fields¹³, as in that case the potential is zero along the electron optical axis. Third order effects introduce a combination of a constant energy difference and a quadratic energy change as function of the arrival time in the beam blanker.

All ultrafast beam blankers, to our knowledge, currently for use in UEM use sinusoidal fields. Sinusoidal fields have the advantage that they can easily be amplified with resonant structures, necessary to generate high slew rate deflection fields resulting in short electron pulses. The UFB presented here is different because the deflection field has a broad spectrum in the frequency domain. We generate high slew rate deflection fields, by deflecting the beam

with fields in the THz frequency domain instead of at GHz frequencies. A fundamental difference between both approaches is that the second order term for the energy gain is zero when sinusoidal fields are used, as shown in Table 4.1.

	First order:	Second order:	Third order:
Sinusoidal field: $V(t) = V_0 \sin(2\pi t/\tau_f)$	$\alpha_1 = 2\pi/\tau_f$	$\alpha_2 = 0$	$\alpha_3 = 8\pi^3/6\tau_f^3$
Exponential field: $V(t) = V_0(1 - 2\exp(-t/\tau_f))$	$\alpha_1 = 2/\tau_f$	$\alpha_2 = -1/\tau_f^2$	$\alpha_3 = 1/3\tau_f^3$

Table 4.1: Expressions for the expansion terms in the time-dependent part of the blanking potential in quasi-static approximation for both sinusoidal and exponential deflection fields.

With the terms in Table 4.1 and using reduced brightness, B_r , current, and FW50 electron pulse length Δt , the expressions for the energy gain can be rewritten with the aid of the Maple software, to find (see Appendix B):

$$\Delta E_1 = 4\sqrt{2} \frac{V_0 \sqrt{I}}{E_0 \Delta t d_p \pi \sqrt{q/m} \sqrt{B_r}} \quad (4.13)$$

$$\Delta E_2(\tau) = -16\sqrt{2} \frac{IV_0 \sqrt{\phi}}{(\pi d_p E_0 \Delta t)^2 \sqrt{q/m} LB_r} \tau$$

where E_0 is the initial strength of deflection field in the UFB, d_p , is the FW50 probe size and I is the DC beam current in the UFB. The equations clearly show the importance of a small distance between the deflector plates, d : the first order term increases linearly with d and the second order quadratically. A high reduced brightness source is also essential for the UFB, it allows more current in the pulse for a given energy gain.

The approximations for the energy gain are compared with the numerical simulation. The normalized deflection field is fitted to calculate the a -coefficients in the polynomial (see the inset in Figure 4.12), which yields values of $-4.47 \cdot 10^{12} \text{ s}^{-1}$, $5.34 \cdot 10^{24} \text{ s}^{-2}$ and $-8.39 \cdot 10^{35} \text{ s}^{-3}$ for a_1 , a_2 , and a_3 , respectively. Subsequently equation (1.12) is used to calculate the energy gain as function of arrival time in the blanker. The result of this calculation is shown in Figure 4.12.

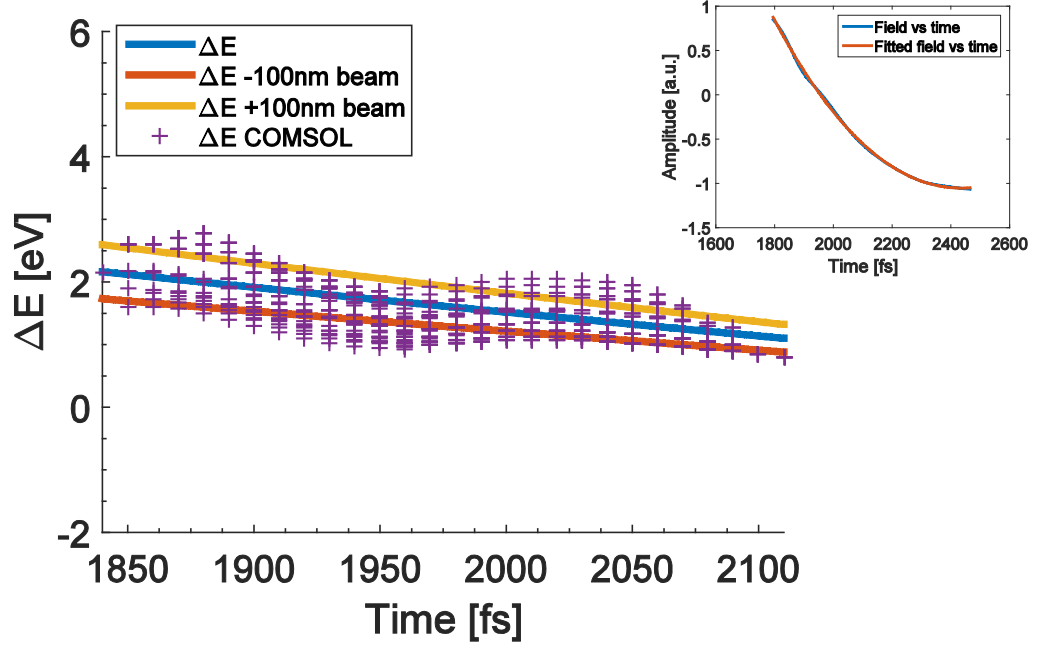


Figure 4.12: Energy gain as function of arrival time in the tunnel like deflector calculated with Comsol (purple crosses). The blue line is the energy gain as function of time for a beam propagating along the electron optical axis calculated with equation (4.12). (inset) Result of the polynomial fit to fit the deflection field in the deflector. The yellow and red line describe the energy gain of the 100 nm off-axis beams.

With the simplified quasi-static model and a square like potential a reasonable estimation of the energy gain for a tunnel-type UFB is obtained. Only the small oscillations in the energy gain as function of arrival time are not described with the approximations we use. Using a similar approximation of the energy gain around the open-type UFB will not work, due to the significant effect of non-quasi-static fields on the energy gain.

4.6. Estimation energy spread

As a result of the time- and trajectory-dependent energy gain in the blanker that we numerically calculated in the previous section, the energy spread in the electron beam will change. In the remainder of the section we will refer to this as the energy spread introduced by the UFB. A second parameter is the first order constant energy gain, ΔE_1 , introduced by the UFB because it's value determines whether an additional blanker is required to intercept the even or odd electron pulses. It is important to know the range of beam currents and electron pulse lengths in which the energy spread and constant energy gain are low. In

Figure 4.13a, the constant energy gain is plotted for a range of pulse lengths and beam currents, as calculated using the simplified quasi-static approximations. This clearly shows that for electron pulse length longer than 400 fs and current below 5 nA both even and odd pulses from the blanker can be used, as there is a 0.4 eV energy difference between the even and odd pulses.

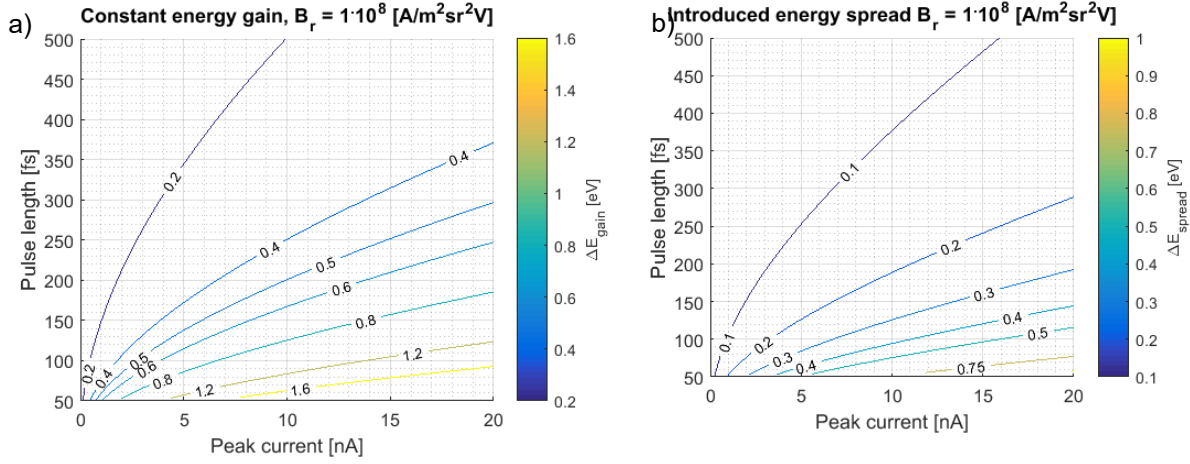


Figure 4.13: (a) Constant energy gain as function of current and FW50 pulse length at 28.5 keV beam energy. For low currents and long electron pulses the energy gain is small compared to the source energy spread and both even and odd electron pulses can be used. (b) Energy spread in the electron pulse as function of current and pulse length. In both figures we assume a probe size of 175 nm in the UFB. The peak current is the current in the electron pulse which is equivalent to the average beam current between the blarker plates. The Comsol energy spread calculation presented in Figure 4.12 corresponds to a pulse length of 125 fs and a current of 16 nA.

The calculated energy spread is shown in Figure 4.13b, for the situation where the separation between the blarker plates is 1 μm . The energy spread introduced by the UFB is estimated by the squared addition of the difference in off-axis energy gain over the FW50 spot size, the difference in second order energy gain over the FW50 pulse length and the third order effect. The latter has a very small contribution, lower than 0.025 eV. The energy spread depends on the size of the electron spot in the UFB, for which we took a value of 175 nm. The energy spread can be further reduced by increasing the probe size, however the larger the probe size the more electrons hit the sides of the UFB. The spot in the UFB is a magnified image of the virtual source which has a certain shape, for example a Gaussian. A Gaussian probe of 175 nm FWHM will have a 10^{-4} fraction in the tails that extend into the deflector plates. It is unknown how many of these electrons scatter such that they end up in the sample chamber. However, if only a small fraction of the scattered electrons ends up in the sample chamber, the resulting background signal may still be significant and visible in a pump-probe measurement as the duty cycle of the blarker is only 10^{-5} .

4.7. Temporal distortion of the electron pulse due to energy spread and magnetic lens

An electron pulse traveling through free space over a distance L_s at an energy ϕ will be delayed by time $-\Delta t$ if it acquires an additional energy δE . This Δt is described by:

$$\Delta t = L_s \left(\frac{1}{v + \Delta v} - \frac{1}{v} \right) = -L_s \frac{\Delta v}{v^2 + v\Delta v} \approx -L_s \frac{\Delta v}{v^2} = -L_s \frac{\delta E}{2\sqrt{\frac{2e}{m}}\phi^{3/2}} \quad (4.14)$$

The equation shows that there is an approximate linear relationship between the energy loss and the broadening of the electron pulse. At a beam energy of 30 keV the dispersion is 160

fs/eV·m, hence a 1 eV energy difference over a drift space of 0.2 m will induce a pulse broadening of 32 fs. This 0.2 m is a typical value for the distance between the UFB and the sample. Thus the beam blanker cannot generate electron pulses shorter than about 20 fs, provided that the source has an energy spread of 0.6 eV. Note that the electron source is even further away from the sample, so this effect will be stronger when the pulses are created by direct laser irradiation of the source.

The final lens of the microscope will also induce a broadening of the pulse as discussed by Weninger and Baum.³¹ They calculated the temporal distortion for an electron pulse originating from a photocathode and focused by a magnetic lens. We calculated the temporal distortion of an electron pulse originating from a crossover located before the final magnetic lens as shown in

Figure 4.14. The temporal distortion is small, less than 5 fs for typical opening angles.

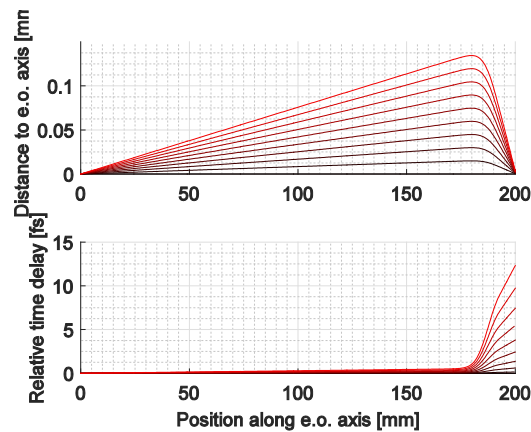


Figure 4.14: Temporal distortion of the electron pulse induced by the magnetic lens in a typical SEM system. The position of the UFB is at $x = 0$, the beam energy is 30 keV and the crossover in the UFB is demagnified on the sample by means of a magnetic lens, calculated with EOD. The most outer ray in the graph corresponds to a half-opening angle of 0.8 mrad, where 0.4 mrad is a typical working value. Thus, the temporal distortion induced by the magnetic lens is typically less than 5 fs.

The combination of the energy spread of the source, the energy spread induced by the UFB and the temporal distortion implies that the electron pulse lengths will be increased by roughly 30 fs.

4.8. Influence of even versus odd UFB voltage switching

In our concept of an UFB, the deflector electrode inverts from positive to negative voltage for even pulses and oppositely for uneven laser pulses.^{10,11} For an even laser pulse the electrons in the pulse will encounter a net energy gain. However for uneven pulses there will be a net energy loss. For the even pulses the deflector is at the anode side of the switch and for the uneven pulses at the cathode side, hence a difference in electron pulse length is expected. For electron pulses of a few 100 fs and shorter, an additional deflector would be required to intercept the odd pulses to reduce the effective energy spread and obtain shorter electron pulses.

In all our simulations, we put the deflector plate at the anode side of the photoconductive switch. We expect a significant difference in performance whether the deflector is at the anode

or cathode side of the photoconductive switch. Higher amounts of terahertz radiation are generated when the laser spot illuminates the switch at locations closer to the anode side, because the mobility at the anode is higher than at the cathode.³²⁻³⁴ At the anode, electrons in the GaAs layer will be taken up quickly due to their low effective mass, while this process will be slower at the cathode. Hence when the deflector plate is at the anode it will be quickly discharged because electrons are injected at a high rate into the deflector plate.

4.9. Conclusions

A full time-dependent electromagnetic FEM simulation of a photoconductive switch integrated with a MEMS-sized deflector is performed in combination with particle tracing of an electron beam to study the dynamics of the resulting pulsed electron beam. The numerical calculations show that it is possible to invert the deflection field on a time scale of about 500 fs. This value is comparable with measured THz pulse lengths created with LT-GaAs photoconductive switches illuminated with femtosecond laser pulses.^{21,35}

The particle tracing simulations show a negligible increase in emittance, demonstrating that the brightness of the electron pulse will remain high. Depending on the chosen opening angle of the electron beam, electron pulse lengths shorter than 150 fs can be achieved.

The numerical calculations further show that, in case the fringe fields extend far enough outside the UFB, the effective increase of deflector length with retardation effects of the EM fields outside the deflector have a significant effect on the energy gain of an electron after propagating through the deflector. Analytical equations of the time-dependent fields extending outside the deflector are hard to derive, hence numerical calculations are required to calculate the energy gain. In a tunnel-type design where the fringe fields are confined by shielding the deflector electrode with conducting grounded plates, the energy spread in the pulse will be limited to 0.5 eV. This is comparable to or lower than the energy spread of a Schottky electron source. In such a case the induced energy gain can be quite accurately estimated, provided that it is known how fast the deflection field inverts. The encapsulation of the deflector electrode in the tunnel-type design reduces the energy spread for two reasons. The first one is that it limits the extent of the fringe field and hence the effective length of the deflector. The second reason is that, because of the more limited spatial extent of the potential outside the deflector, retardation effects in the potential can be neglected, i.e. it prevents the electron beam from further acceleration by the electromagnetic wave emitted from a non-shielded deflector.

Finally, we argued that the further temporal distortion of the electron pulse by the final (magnetic) lens in a SEM is less than 10 fs and that temporal broadening of the electron pulse between the UFB and sample is about 30 fs. Thus, we expect that electron pulses of about 100 fs are achievable using a laser-triggered beam blanker in a SEM, with negligible increase in emittance and with only a marginal increase in energy spread.

4.10. Acknowledgements

This work is part of the research program of the Foundation for Fundamental Research on Matter (FOM), which is part of the Netherlands Organisation for Scientific Research (NWO), through grants 10PR2826 and 16VAL11N. We also like to thank Aurele Adam, Ying Tang, and Lei Wei for their technical support with Comsol and the use of their CPU cluster.

Appendix A – Sensitivity of simulation results to mesh refinement

In order to check the convergence and accuracy of the simulation a set of simulations is performed with different mesh sizes. The most important part of the electromagnetic fields is the region along the electron-optical axis. Hence, the x and z of the electric field components for different mesh sizes have been plotted in Figure 4.15.

In principle, the mesh size has to be a factor 10 smaller than the wavelength involved. At a frequency of 10 THz this corresponds to $3\ \mu\text{m}$ in vacuum and $1\ \mu\text{m}$ in GaAs. The deflector electrode is meshed with triangles with sides of 400-600 nm and up to $5\ \mu\text{m}$ deep in the GaAs layer below the deflector electrode the mesh size is smaller than or about $1\ \mu\text{m}$.

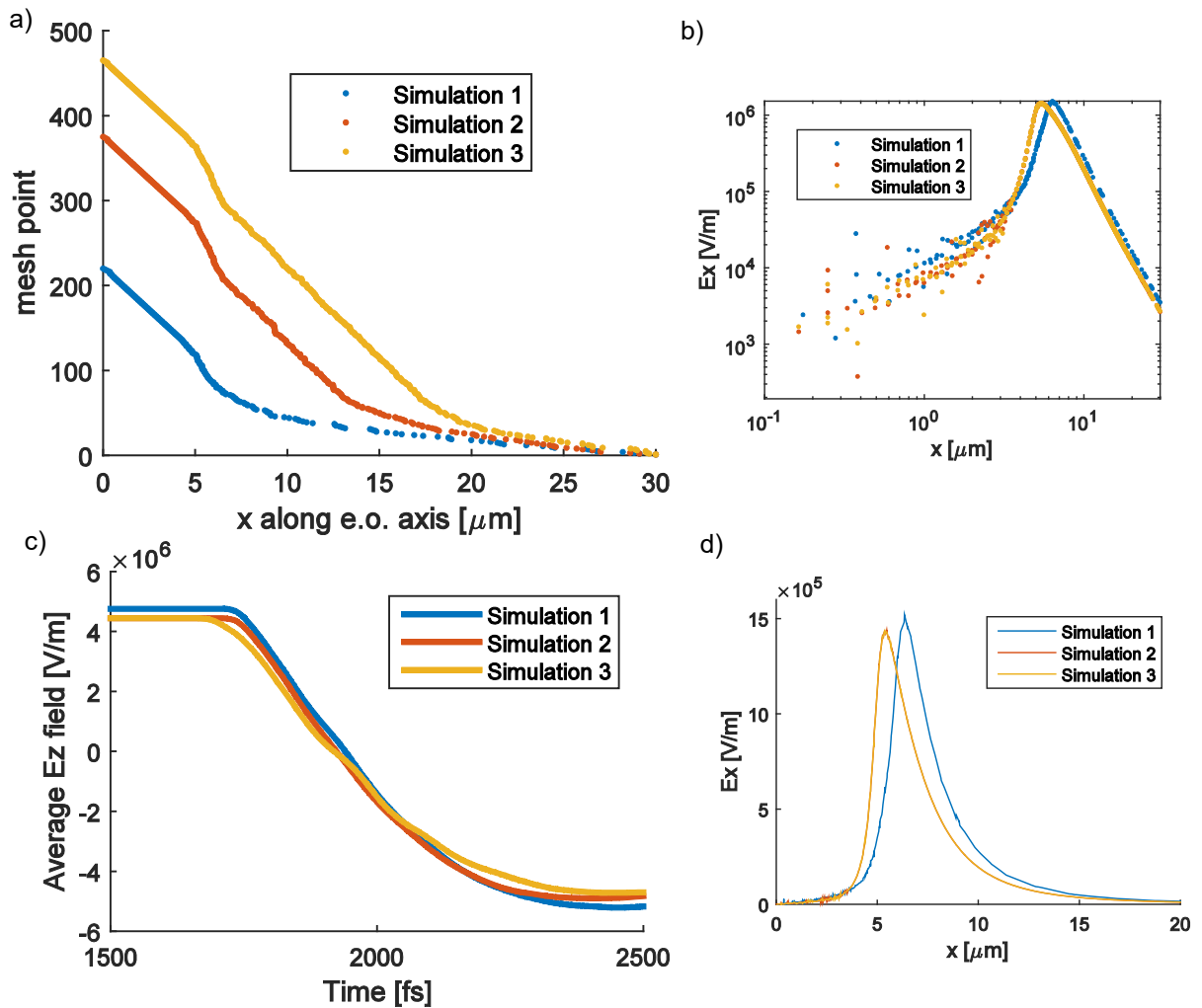


Figure 4.15: (a) Number of mesh points for 3 different simulations, the deflector is from $x = 0$ to $5\ \mu\text{m}$. (b and d) Electrostatic field, component along the electron optical axis, it is clearly visible that the simulation with the lowest amount of mesh points has a peak in the E_x field outside the blanker plates. (c) Averaged deflection field along the e.o. axis, over a length of $10\ \mu\text{m}$, the time dependence of simulation 1 and 2 is comparable. Simulation 3 has a slower time response and some weak oscillations are visible. In order to run simulation 3 in a system with a finite memory the mesh size in the GaAs chip has been reduced, this might have changed the temporal response slightly.

We concluded that ‘simulation 2’ gives the most reliable results. The reason for not choosing the even finer mesh of ‘simulation 3’ is that an additional mesh refinement box was placed around the deflector plate. This box intersected part of the deflector plate and might have

caused reflections over there. Due to different meshing the local impedance might differ slightly and hence reflections are induced, the reflections are visible in Figure 4.15 (bottom left).

For simulation 3 the total capacitance of the deflector plate is 6.60 fF, for simulation 2 the value is 6.76 fF.

Appendix B – Energy spread induced by quasi-static fields

For the analytical equations we assume quasi-static electric fields, so we can write down the following equation for the energy change of an electron after traveling through the deflection system:

$$\Delta E(\tau) = - \int_{x=-\infty}^{+\infty} f(t+\tau) \frac{d\phi(x)}{dx} dx \quad (4.15)$$

where $\phi(x)$ is the potential along the electron-optical axis, only depending on x because we assume it is a quasi-static field. The function $f(t)$ describes the time dependence of the field in the blanker. Using integration by parts we can rewrite equation (4.15) in the following equation:

$$\begin{aligned} \Delta E(\tau) &= f\left(\frac{x}{v} + \tau\right) \phi(x) \Big|_{-\infty}^{+\infty} + \int_{x=-\infty}^{+\infty} \phi(x) \frac{df\left(\frac{x}{v} + \tau\right)}{dx} dx \\ \Delta E(\tau) &= \int_{x=-\infty}^{+\infty} \phi(x) \frac{df\left(\frac{x}{v} + \tau\right)}{dx} dx \end{aligned} \quad (4.16)$$

where we assume that $\phi(x)$ is zero at infinity. In general $f(t)$ can be approximated by a polynomial:

$$f(t-\tau) = \alpha_1 \left(\frac{x}{v} + \tau\right) + \alpha_2 \left(\frac{x}{v} + \tau\right)^2 + \alpha_3 \left(\frac{x}{v} + \tau\right)^3 + \dots \quad (4.17)$$

The linear part in the polynomial gives the following:

$$\Delta E_1(\tau) = \int_{x=-\infty}^{+\infty} \phi(x) \frac{\alpha_1}{v} dx \quad (4.18)$$

Notice that for a linear ramp of the potential in time no bunching of electrons is to be expected, i.e. the induced energy change is independent of the arrival time τ of the electrons in the blanker. For the non-linear term in the polynomial we can describe the following energy change:

$$\Delta E_2(\tau) = \int_{x=-\infty}^{+\infty} \phi(x) \frac{2\alpha_2 \left(\frac{x}{v} + \tau\right)}{v} dx \quad (4.19)$$

In this case the integral depends on the time τ , in a very simple and rough approximation ϕ can be described as:

$$\begin{aligned} \phi(x) &= V_0 & -\frac{1}{2}\beta L < x < \frac{1}{2}\beta L \\ \phi(x) &= 0 & \text{otherwise} \end{aligned} \quad (4.20)$$

Were L is the length of the blanker plate and β is a correction for the fringe field. From this simple description of the potential we can evaluate the integrals in equations (4.18) and (4.19) and for the third order effect:

$$\begin{aligned}\Delta E_1(\tau) &= V_0 \alpha_1 \frac{\beta L}{v} \\ \Delta E_2(\tau) &= 2V_0 \alpha_2 \frac{\beta L \tau}{v} \\ \Delta E_3(\tau) &= V_0 \alpha_3 \left(\frac{1}{4} \frac{\beta^3 L^3}{v^3} + \frac{3L\beta\tau^2}{v} \right)\end{aligned}\quad (4.21)$$

where α parameters depend on the typical associated time constant of the deflection field, the parameters for sinusoidal and exponential fields are given in the main text in Table 4.1.

The equations can be rewritten in terms of beam current, beam energy and pulse length. These parameters are relevant for designing a system with minimal energy spread. The reduced brightness is defined as follows:

$$B_r = \frac{4I}{\pi^2 d_p^2 \alpha^2 \phi} \quad (4.22)$$

The electron pulse length, Δt , is estimated as:

$$\begin{aligned}E(t) &\approx E_0 \alpha_1 t \\ \Delta t &= \frac{E_b}{E_0 \alpha_1}\end{aligned}\quad (4.23)$$

where E_b is the deflection field strength when the beam is just fully intercepted by the blanking aperture. E_0 is the initial electric deflection field strength. The half-opening angle of the beam is equal to:

$$\alpha = \frac{E_b L}{4\phi} = \frac{E_0 \alpha_1 L \Delta t}{4\phi} > \alpha_1 = \frac{4\phi \alpha}{E_0 L \Delta t} \quad (4.24)$$

These equations of the relation between pulse length and opening angle and reduced brightness can be inserted in the equations describing the different orders in the energy spread. The equation for the first order energy gain is combined with equation (4.22) and (4.24) as follows:

$$\Delta E_1 = \frac{V_0 \alpha_1 L}{v} = \frac{V_0}{v} \frac{4\phi \alpha}{E_0 \Delta t} = 4\sqrt{2} \frac{V_0}{\sqrt{q/m} E_0 \Delta t d_p \pi \sqrt{B_r}} \frac{\sqrt{I}}{E_0 \Delta t d_p \pi \sqrt{B_r}} \quad (4.25)$$

Notice that the first order energy gain is independent of beam energy. For the 2nd ordered energy spread we can write.

$$\Delta E_2(\tau) = 2V_0\alpha_2 \frac{L\tau}{v} = -\frac{V_0L\tau}{2\alpha_1^2 v} = \frac{8V_0\phi^2\alpha^2\tau}{(E_0\Delta t)^2 Lv} = -16\sqrt{2} \frac{IV_0\sqrt{\phi}}{(\pi d_p E_0\Delta t)^2 \sqrt{q/mLB_r}} \tau \quad (4.26)$$

The arrival time in this equation can be taken out because it depends on the pulse width Δt , we use $\tau = \Delta t$, to get the FW50 energy spread:

$$\Delta E_2 = -\frac{32IV_0\sqrt{\phi}}{(d_p E_0)^2 \Delta t \sqrt{2q/mLB_r}} \quad (4.27)$$

For the third order we can write the following equations:

$$\begin{aligned} \Delta E_3(\tau) &= V_0 \frac{\alpha_1^3}{24} \left(\frac{1}{4} \frac{L^3}{v^3} + \frac{3L\tau^2}{v} \right) \\ \Delta E_3(\tau) &= \frac{4}{3} \sqrt{2} V_0 \left(\frac{mI}{B_r q} \right)^{\frac{3}{2}} \left(\frac{1}{E_0 \Delta t d_p} \right)^3 + \frac{32V_0\phi I^{3/2} \sqrt{2m/q}}{E_0^3 L^2 \pi^3 d_p^3 B_r^{3/2}} \frac{\tau^2}{\Delta t^3} \end{aligned} \quad (4.28)$$

where we estimated $\alpha_3 = \alpha_1^3 / 24$.

Appendix C – Maple worksheet of the blur calculation

[> restart;

[Taylor expansion to time of the electric field in the deflector:

> $taylor_e := taylor\left(1 - 2 \cdot \exp\left(-\frac{t}{\tau_f}\right), t=0, 3\right);$

$$taylor_e := -1 + 2 \frac{1}{\tau_f} t - \frac{1}{\tau_f^2} t^2 + O(t^3)$$
 (1)

> $taylor_e := convert(taylor_e, polynom);$

$$taylor_e := -1 + \frac{2t}{\tau_f} - \frac{t^2}{\tau_f^2}$$
 (2)

[Transversal acceleration of an electron in the deflection field:

> $a := \frac{q \cdot E}{m} \cdot (taylor_e);$

$$a := \frac{q E \left(-1 + \frac{2t}{\tau_f} - \frac{t^2}{\tau_f^2} \right)}{m}$$
 (3)

>

[Transversal velocity, v:

> $v := int\left(a, t=-\frac{t0}{2} + \tau \dots \frac{t0}{2} + \tau\right);$

$$v := -\frac{q E \left(\left(\frac{t0}{2} + \tau \right)^3 - \left(-\frac{t0}{2} + \tau \right)^3 \right)}{3 m \tau_f^2} + \frac{q E \left(\left(\frac{t0}{2} + \tau \right)^2 - \left(-\frac{t0}{2} + \tau \right)^2 \right)}{m \tau_f} - \frac{q E t0}{m}$$
 (4)

[where t0 is the residence time of the electron in the field, tau is the time in the e- pulse with respect of the zero crossing of the electric field. Integration of v yields the following transversal displacement:

> $y := int\left(int\left(a, t=-\frac{t0}{2} + \tau \dots t\right), t=-\frac{t0}{2} + \tau \dots \frac{t0}{2} + \tau\right);$

$$y := -\frac{q E \left(\left(\frac{t0}{2} + \tau \right)^4 - \left(-\frac{t0}{2} + \tau \right)^4 \right)}{12 m \tau_f^2} + \frac{q E \left(\left(\frac{t0}{2} + \tau \right)^3 - \left(-\frac{t0}{2} + \tau \right)^3 \right)}{3 m \tau_f}$$
 (5)

$$-\frac{q E \left(\left(\frac{t0}{2} + \tau \right)^2 - \left(-\frac{t0}{2} + \tau \right)^2 \right)}{2 m} + \frac{q E \left(-\frac{t0}{2} + \tau \right)^3 t0}{3 m \tau_f^2} - \frac{q E \left(-\frac{t0}{2} + \tau \right)^2 t0}{m \tau_f}$$

$$-\frac{q E \left(\frac{t0}{2} - \tau \right) t0}{m}$$

[In the following 2 equation we determine the virtual point of origin, i.e. the off axis position of the electron half-way the deflector where the electron appears to originate from:

> $delta_y := v \cdot \left(\frac{1}{2} \right) \cdot t0;$

$$\begin{aligned} \text{delta}_y := & \frac{1}{2} \left(\left(-\frac{q E \left(\left(\frac{t0}{2} + \tau \right)^3 - \left(-\frac{t0}{2} + \tau \right)^3 \right)}{3 m \tau_f^2} \right. \right. \\ & \left. \left. + \frac{q E \left(\left(\frac{t0}{2} + \tau \right)^2 - \left(-\frac{t0}{2} + \tau \right)^2 \right)}{m \tau_f} - \frac{q E t0}{m} \right) t0 \right) \end{aligned} \quad (6)$$

$$\begin{aligned} & > y_{sp} := y - \text{delta}_y; \\ y_{sp} := & -\frac{q E \left(\left(\frac{t0}{2} + \tau \right)^4 - \left(-\frac{t0}{2} + \tau \right)^4 \right)}{12 m \tau_f^2} + \frac{q E \left(\left(\frac{t0}{2} + \tau \right)^3 - \left(-\frac{t0}{2} + \tau \right)^3 \right)}{3 m \tau_f} \\ & - \frac{q E \left(\left(\frac{t0}{2} + \tau \right)^2 - \left(-\frac{t0}{2} + \tau \right)^2 \right)}{2 m} + \frac{q E \left(-\frac{t0}{2} + \tau \right)^3 t0}{3 m \tau_f^2} - \frac{q E \left(-\frac{t0}{2} + \tau \right)^2 t0}{m \tau_f} \\ & - \frac{q E \left(\frac{t0}{2} - \tau \right) t0}{m} - \frac{1}{2} \left(\left(-\frac{q E \left(\left(\frac{t0}{2} + \tau \right)^3 - \left(-\frac{t0}{2} + \tau \right)^3 \right)}{3 m \tau_f^2} \right. \right. \\ & \left. \left. + \frac{q E \left(\left(\frac{t0}{2} + \tau \right)^2 - \left(-\frac{t0}{2} + \tau \right)^2 \right)}{m \tau_f} - \frac{q E t0}{m} \right) t0 \right) \end{aligned} \quad (7)$$

$$\begin{aligned} & > y_{sp} := \text{simplify}(y_{sp}); \\ y_{sp} := & \frac{q E t0^3 (\tau - \tau_f)}{6 m \tau_f^2} \end{aligned} \quad (8)$$

Determine the position of the virtual crossover in the deflector of the front and back of the electron pulse:

$$\begin{aligned} & > y1 := \text{subs} \left(\tau = \frac{1}{2} \tau_e, y_{sp} \right); \\ y1 := & \frac{q E t0^3 \left(\frac{\tau_e}{2} - \tau_f \right)}{6 m \tau_f^2} \end{aligned} \quad (9)$$

$$\begin{aligned} & > y2 := \text{subs} \left(\tau = -\frac{1}{2} \tau_e, y_{sp} \right); \\ y2 := & \frac{q E t0^3 \left(-\frac{\tau_e}{2} - \tau_f \right)}{6 m \tau_f^2} \end{aligned} \quad (10)$$

$$\begin{aligned} & > y_{blur} := y1 - y2; \\ y_{blur} := & \frac{q E t0^3 \left(\frac{\tau_e}{2} - \tau_f \right)}{6 m \tau_f^2} - \frac{q E t0^3 \left(-\frac{\tau_e}{2} - \tau_f \right)}{6 m \tau_f^2} \end{aligned} \quad (11)$$

$$> y_{blur} := \text{simplify}(y_{blur});$$

$$y_blur := \frac{q E t_0^3 \tau_e}{6 m \tau_f^2} \quad (12)$$

$$> t_0 := \frac{L}{v_0};$$

$$t_0 := \frac{L}{v_0} \quad (13)$$

$$> v_0 := \text{sqrt}\left(\frac{2 q \cdot \phi}{m}\right);$$

$$v_0 := \sqrt{2} \sqrt{\frac{q \phi}{m}} \quad (14)$$

$$> y_blur;$$

$$\frac{q E L^3 \sqrt{2} \tau_e}{24 \left(\frac{q \phi}{m}\right)^{3/2} m \tau_f^2} \quad (15)$$

$$> \text{simplify}(y_blur);$$

$$\frac{E L^3 \sqrt{2} \tau_e}{24 \phi \sqrt{\frac{q \phi}{m}} \tau_f^2} \quad (16)$$

The following parameters are used for the MEMS UFB described in the paper:

$$> \phi := 30e3; \tau_f := 300e-15; q := 1.6e-19; L := 1e-5; m := 9.11e-31; E := \frac{10}{1e-6};$$

$$\tau_e := 100e-15;$$

$$\begin{aligned} \phi &:= 30000. \\ \tau_f &:= 3.00 \cdot 10^{-13} \\ q &:= 1.6 \cdot 10^{-19} \\ L &:= 0.00001 \\ m &:= 9.11 \cdot 10^{-31} \\ E &:= 1.0 \cdot 10^7 \\ \tau_e &:= 1.00 \cdot 10^{-13} \end{aligned} \quad (17)$$

$$> y_blur := \text{subs}(y_blur);$$

$$y_blur := 2.126001483 \cdot 10^{-10} \sqrt{2} \quad (18)$$

>
>
>
>
>
>

Bibliography

1. Weppelman, I. G. C. *et al.* Pulse length, energy spread, and temporal evolution of electron pulses generated with an ultrafast beam blanker. *Struct. Dyn.* **6**, (2019).
2. Siwick, B. J., Dwyer, J. R., Jordan, R. E. & Miller, R. J. D. An atomic-level view of melting using femtosecond electron diffraction. *Science* **302**, 1382–5 (2003).
3. Barwick, B., Flannigan, D. J. & Zewail, A. H. Photon-induced near-field electron microscopy. *Nature* **462**, 902–6 (2009).
4. Zewail, A. H. Four-dimensional electron microscopy. *Science* **328**, 187–93 (2010).
5. Feist, A. *et al.* Quantum coherent optical phase modulation in an ultrafast transmission electron microscope. *Nature* **521**, 200–203 (2015).
6. Hommelhoff, P., Kealhofer, C. & Kasevich, M. A. Ultrafast Electron Pulses from a Tungsten Tip Triggered by Low-Power Femtosecond Laser Pulses. *Phys. Rev. Lett.* **97**, 247402 (2006).
7. Lassise, A., Mutsaers, P. H. A. & Luiten, O. J. Compact, low power radio frequency cavity for femtosecond electron microscopy. *Rev. Sci. Instrum.* **83**, 043705 (2012).
8. van Rens, J. F. M. *et al.* Theory and particle tracking simulations of a resonant radiofrequency deflection cavity in TM 110 mode for ultrafast electron microscopy. *Ultramicroscopy* **184**, 77–89 (2018).
9. Verhoeven, W., van Rens, J. F. M., Kieft, E. R., Mutsaers, P. H. A. & Luiten, O. J. High quality ultrafast transmission electron microscopy using resonant microwave cavities. *Ultramicroscopy* **188**, 85–89 (2018).
10. Kruit, P. & Weppelman, I. G. C. Device and method for generating charged particle beam pulses. (2016).
11. Weppelman, I. G. C., Moerland, R. J., Hoogenboom, J. P. & Kruit, P. Concept and design of a beam blanker with integrated photoconductive switch for Ultrafast Electron Microscopy. *Ultramicroscopy* **184**, 8–17 (2017).
12. Fowler, T. K. & Good, W. M. A theory on obtaining short bursts of ions from a beam of ions. *Nucl. Instruments Methods* **7**, 245–252 (1960).
13. Thong, J. T. L. Picosecond electron pulse generation via beam deflection-chopping in the SEM. *Meas. Sci. Technol.* 207–216 (1991).
14. Oldfield, L. C. A rotationally symmetric electron beam chopper for picosecond pulses. *J. Phys. E.* **9**, 455–463 (1976).
15. Lassise, A. C. Miniaturized RF Technology for Femtosecond Electron Microscopy. (Eindhoven University of Technology, 2012).
16. Van Rens, J. F. M., Verhoeven, W., Kieft, E. R., Mutsaers, P. H. A. & Luiten, O. J. Dual mode microwave deflection cavities for ultrafast electron microscopy. *Appl. Phys. Lett.* **113**, (2018).
17. Cook, B. Brightness Limitations in sources for static & ultra-fast high resolution electron microscopy. (Delft University of Technology, 2013).
18. Kealhofer, A. C. *et al.* All-optical control and metrology of electron pulses. *Science* (80-). **352**, 429–433 (2016).

19. Ryabov, A. & Baum, P. Electron microscopy of electromagnetic waveforms. *Science* (80-.). **2182**, 2179–2182 (2016).
20. Blakemore, J. S. Semiconducting and other major properties of gallium arsenide. *J. Appl. Phys.* **53**, (1982).
21. Jepsen, P. U., Jacobsen, R. H. & Keiding, S. R. Generation and detection of terahertz pulses from biased semiconductor antennas. *J. Opt. Soc. Am. B* **13**, 2424 (1996).
22. Piao, Z. S., Tani, M. & Sakai, K. Carrier dynamics and THz radiation in biased semiconductor structures. *SPIE Conf. Terahertz Spectrosc. Appl.* **3617**, 49–56 (1999).
23. Duvillaret, L., Garet, F., Roux, J.-F. & Coutaz, J.-L. Analytical modeling and optimization of terahertz time-domain spectroscopy experiments, using photoswitches as antennas. *IEEE J. Sel. Top. Quantum Electron.* **7**, 615–623 (2001).
24. Jellison, G. E. Optical functions of GaAs, GaP, and Ge determined by two-channel polarization modulation ellipsometry. *Opt. Mater. (Amst)*. **1**, 151–160 (1992).
25. Ordal, M. a, Bell, R. J., Alexander, R. W., Newquist, L. a & Querry, M. R. Optical properties of Al, Fe, Ti, Ta, W, and Mo at submillimeter wavelengths. *Appl. Opt.* **27**, 1203–9 (1988).
26. Lepeshov, S. I., Gorodetsky, A., Krasnok, A. E., Rafailov, E. U. & Belov, P. A. Enhancement of Terahertz Photoconductive Antennas and Photomixers Operation by Optical Nanoantennas. 1–19 (2016).
27. van Veen, A. H. V., Hagen, C. W., Barth, J. E. & Kruit, P. Reduced brightness of the ZrO/W Schottky electron emitter. *J. Vac. Sci. Technol. B Microelectron. Nanom. Struct.* **19**, 2038 (2001).
28. Bronsgeest, M. S., Barth, J. E., Swanson, L. W. & Kruit, P. Probe current, probe size, and the practical brightness for probe forming systems. *J. Vac. Sci. Technol. B Microelectron. Nanom. Struct.* **26**, 949 (2008).
29. Cook, B., Verduin, T., Hagen, C. W. & Kruit, P. Brightness limitations of cold field emitters caused by Coulomb interactions. *J. Vac. Sci. Technol. B Microelectron. Nanom. Struct.* **28**, C6C74 (2010).
30. Schwind, G. a., Magera, G. & Swanson, L. W. Comparison of parameters for Schottky and cold field emission sources. *J. Vac. Sci. Technol. B Microelectron. Nanom. Struct.* **24**, 2897 (2006).
31. Weninger, C. & Baum, P. Temporal distortions in magnetic lenses. *Ultramicroscopy* **113**, 145–151 (2012).
32. Ralph, S. E. & Grischkowsky, D. Trap-enhanced electric fields in semi-insulators: The role of electrical and optical carrier injection. *Appl. Phys. Lett.* **59**, 1972–1974 (1991).
33. Upadhyaya, P. C. *et al.* Excitation-density-dependent generation of broadband terahertz radiation in an asymmetrically excited photoconductive antenna. *Opt. Lett.* **32**, 2297–2299 (2007).
34. Berry, C. W. & Jarrahi, M. Principles of Impedance Matching in Photoconductive Antennas. *J. Infrared, Millimeter, Terahertz Waves* **33**, 1182–1189 (2012).
35. *Physics and Applications of Terahertz Radiation*. (Springer, 2014). doi:10.1007/978-94-007-3837-9

5 MEMS Fabrication of the UFB and incorporation in the SEM

The concept of a MEMS sized ultrafast beam blanker (UFB) controlled by a photoconductive switch to create ultrafast electron pulses is extensively discussed in Chapter 3.[1] Detailed numerical calculations of the pulse length and electron beam properties in terms of brightness and energy spread are discussed in Chapter 4 and [2]. From this numerical and back-of-the-envelope calculations we expect it to be possible to create electron pulses of a few 100 fs long at electron beam energies of 30 keV with a MEMS-made UFB, see Figure 5.1. The required dimensions are summarized in Figure 5.2.

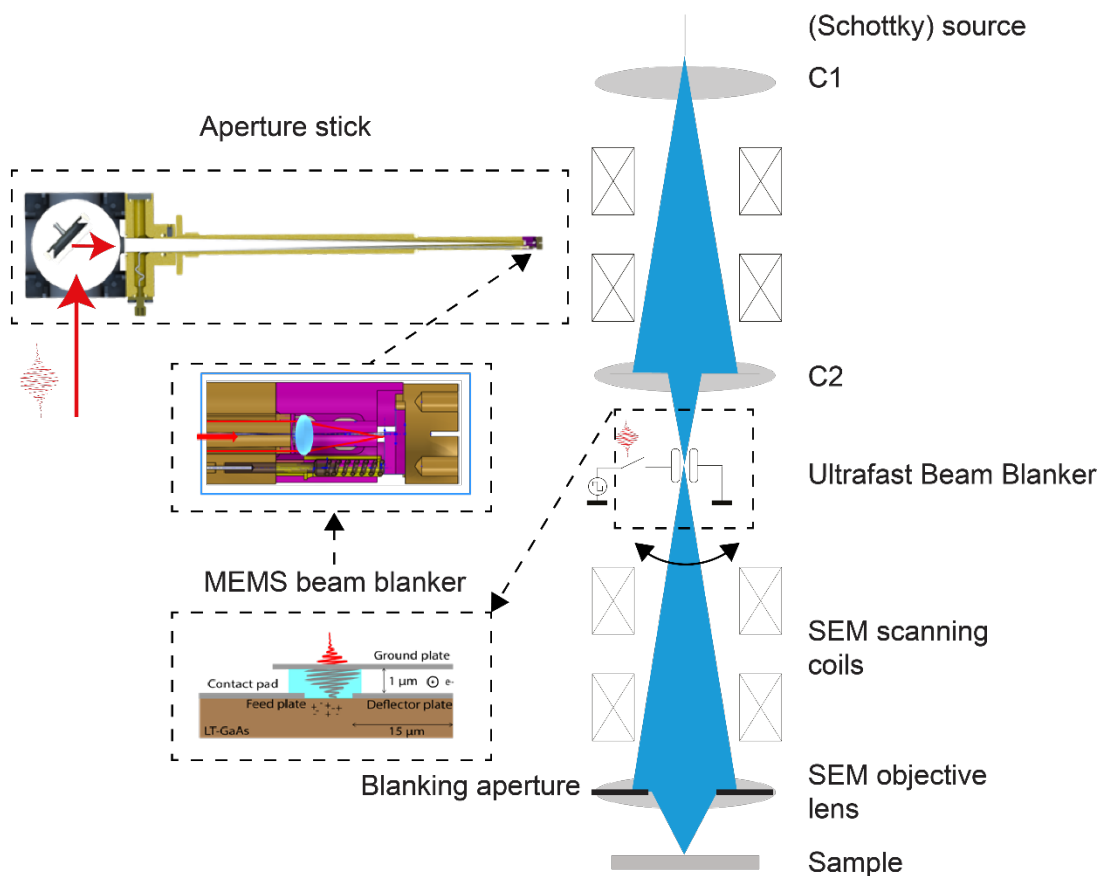


Figure 5.1: Schematic drawing of the whole system, on the right the column of the SEM, the ultrafast beam blanker is in a conjugate plane below the C2 condenser lens, the blanker has micrometer scale (MEMS) dimensions, the laser pulses are focused on it with a small 2 mm diameter lens, the laser beam is guide into the SEM column by means of an in house designed and built aperture stick, in the subsequent paragraphs of this chapter all subsystems are explained in detail.

In this chapter, we describe the fabrication, experimental implementation, and validation of the MEMS UFB. A detailed description and discussion of the MEMS fabrication of the UFB is presented in section 5.2. A design of a blanker stick to incorporate and align the chip in a standard commercial SEM is discussed in paragraph 5.5. The steps necessary to mount the chip on the blanker stick, the optical alignment procedure and alignment of the blanker with respect to the electron optical axis are discussed in the same paragraph. Initial characterization of the electron pulse length and spatial resolution is discussed in section 5.6. We start first with a brief summary of the requirements for the MEMS UFB.

5.1 UFB fabrication requirements

The UFB consists of a 10 by 10 μm photoconductive switch connected to 2 electrodes, one feed electrode with a contact pad connected to an electronic circuit, see Figure 5.2. The other electrode is the blanker plate, 15 μm long, the voltage on this plate is used to deflect the electron beam. The photoconductive switch consists of LT-GaAs. The device has to be made of vacuum compatible materials and should be electrically conductive to prevent charging.

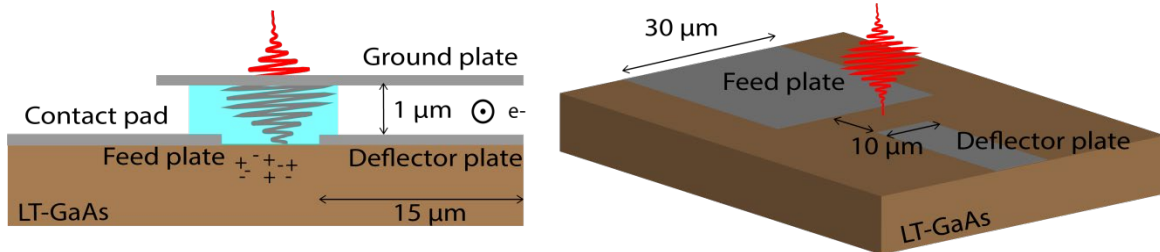


Figure 5.2. a) Side view of the ultrafast beam blanker design, with the contact pad to supply a voltage to the feed plate, and the ground and deflector plate indicated. The electron beam traverses the space between the ground and deflector plane perpendicular to this plane. The ground plate is located at 1 μm distance from the feed and blanker plate, this is achieved by a thin SiO_2 layer. (b) View of the LT-GaAs plane from (a), with the feed and deflector plates with their dimensions.

LT-GaAs is the photoconductive material for the switch, because of the high mobility and short carrier recombination time as discussed in Chapter 4.[1] In section 5.3 we will discuss the design and fabrication of the metal electrodes on the photoconductive switch, the design is optimized for high photoconductivity. Another requirement is that there is open access for both the laser and electron beam which axes are under a 90 degrees angle, hence a MEMS device with 3D geometry is required. The electron beam will propagate parallel to the chip at a distance of about 500 nm, see Figure 5.2. Mechanical tilt alignment of the chip with respect to the electron-optical axis is only possible when the electron beam propagates for a relatively short distance close to the chip, we aim for a 1:10 ratio.

Due to the small required dimensions, standard microfabrication techniques are used to fabricate the MEMS UFB. These include lithography, dry/wet etching, and thin film deposition, as discussed in the following section.

5.2 Overview of UFB microfabrication and quality control process

The whole device is fabricated on top of a LT-GaAs wafer. Deep trenches of several 100's of μm deep have to be made in the (LT)-GaAs wafer, to enable free access of the electron beam to the deflector. Deep trenches in Si MEMS devices are typically created with Bosch processes or KOH wet etches. However, there are no dry and wet etch techniques for GaAs that have a sufficiently high selectivity. Hence, the deflector and photoconductive switch are fabricated at the edge of a GaAs chip.

A GaAs wafer with a 1-2 μm thick LT-GaAs layer is purchased from Xiamen Ltd. It has a < 15 ps carrier lifetime according to the supplier, the latter property will ensure that the photoconductive switch will return in sub nanosecond timescale back to a dark state. The 2 inch LT-GaAs wafer is diced in pieces of 9 by 9 mm and cleaned in an acetone bath for 10 minutes, in an ultrasonic bath, and for 1 minute in IPA and dried with pressurized N_2 gas.

Before we describe the fabrication in detail, a short, general overview of the fabrication steps is shown in Figure 5.3 below.

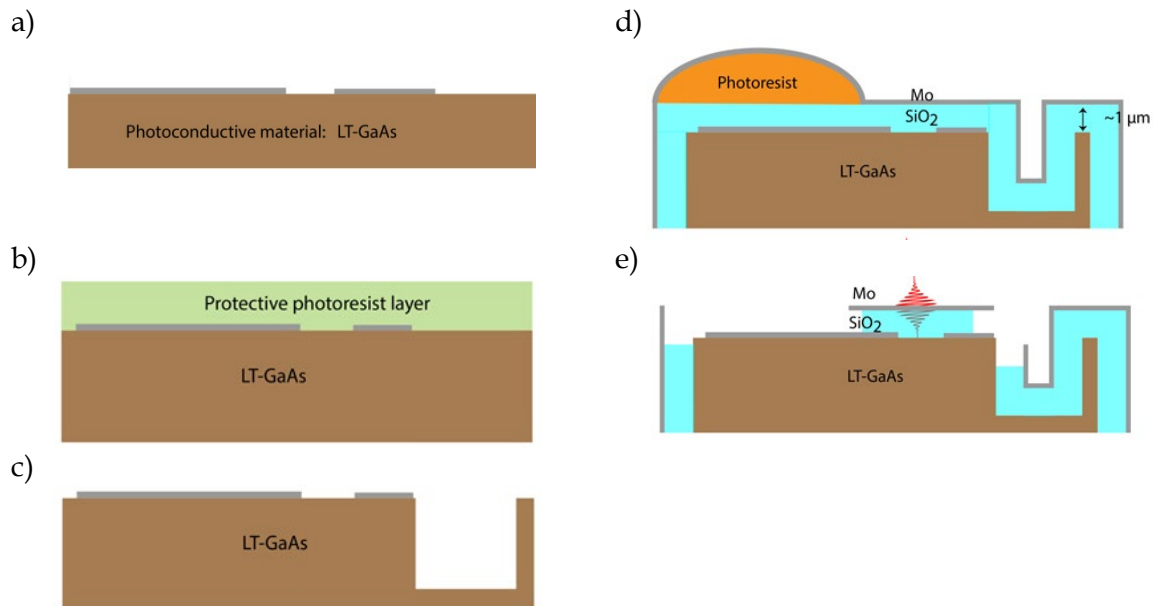


Figure 5.3: General overview of the microfabrication steps for our UFB. (a) The feed plate and blanker plate are defined on the GaAs wafer with e-beam lithography. (b) A photoresist layer is added to protect the electrodes during the dicing process. (c) After dicing and stripping the photoresist, a trench is milled in the chip with a Focused Ion Beam (FIB) defining the length of the blanker plate. (d) A glass and Mo layer are added to the device and photoresist above the contact pad. A FIB mill is used to remove the Mo at the blanker tip, the photoresist is removed with acetone. (e) A subsequent BHF etch is used to etch glass and create an undercut. Molybdenum is chosen as a conductor for the reason it has a conductive oxide layer, is quite strong and it is resistant against BHF.

Within this general fabrication scheme, a few critical steps can be defined, which are listed in Table 5.1 together with the purpose of each step. To monitor the fabrication process, several control steps and intermediate quality control measurements are implemented, which are also indicated in the Table 5.1. For each step, the (process) design, fabrication details, and the results of control and quality tests will be discussed in the next paragraphs, as also indicated in the .

Table 5.1: overview of all microfabrication steps for the MEMS UFB

Fabrication step	Purpose	Control	Corresponding step in Figure 5.3	Described in
Ar sputter etch	Stripping oxide	-		Paragraph 5.3
e-beam lithography	Creating grating pattern for electrodes	-		
Cr & Au deposition	Making electrodes	SEM inspection	(a)	
<i>First quality control test: Dark and photo-current measurement</i>				Figure 5.6
Photoresist deposition	Protection	-	(b)	
Dicing	Creating sharp tip	SEM inspection		

FIB milling	Creating trench	SEM inspection	(c)	
SiO ₂ & Mo deposition	Defining blanker plates	SEM inspection	(d)	
Etching & FIB milling	Opening blanker	SEM inspection	(e)	
<i>Second quality control test: feed vs deflector voltage measurement</i>				Figure 5.10
<i>Third quality control test: dark resistance and resistance to ground measurement</i>				Figure 5.12

5.3 Design and fabrication of photoconductive switch electrodes

5.3.1 Grating electrode design

Maximizing the photoconductivity is of essential importance for the performance of the UFB. In Chapter 3 the importance of the semiconductor material to the conductivity is described in detail. Two contributions to the conductivity can be discerned, the first one is the conductivity between the metal electrode and the semiconductor material, where a Schottky barrier is formed. Ideally the barrier height is reduced to zero and the metal semiconductor interface behaves like an ohmic contact. The latter can be achieved by using metal (alloys) where either the metal diffuses partly in the semiconductor or the other way around, which may require a heat treatment.[3] The second factor determining the photoconductivity is the amount of e-h pairs induced by the laser pulse, which we want to maximize.

The deflector has a capacitance of about 7 fF, hence for a 20 V potential change some 10^6 charges are required. The laser creates about 10^8 carriers over the whole photoconductive switch as discussed in chapter 4. This is relevant because it implies that only the carriers in the first 100 nm from the deflector electrode are required to invert the deflector plate voltage. Hence, a properly designed electrode ensures that a large amount of free carriers is generated close to the electrode. However, a standard planar electrode as depicted in Figure 5.2 has the disadvantage that the electrode acts as a mirror and only a few carriers are generated under the electrode. In recent years developments in the field of nanophotonics have led to improved electrode designs. Berry *et al.* demonstrated that a grating shaped electrode (see Figure 5.5b for an example) enhances the photocurrent with a factor of 100.[4] The use of metals who support a plasmon resonance in the grating enhances the photocurrent even further as light will be concentrated and absorbed even closer to the electrode. The latter requires a glass layer with a certain thickness, which complicates the fabrication of the deflector, hence the glass layer is omitted in the design of the MEMS UFB. Nevertheless a significant enhancement of the amount of light directly around the electrodes is to be expected as finite difference time domain (FDTD) simulations performed with Lumerical clearly show in Figure 5.4.

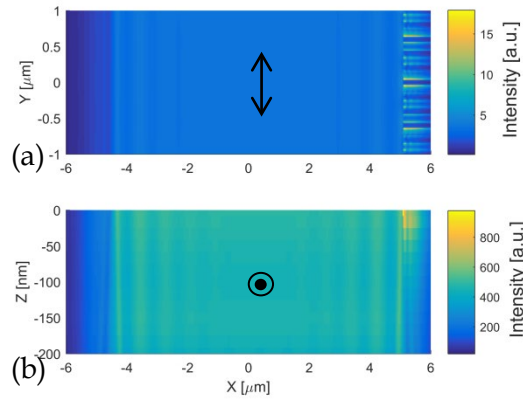


Figure 5.4: Numerical simulations indicating the laser intensity below an electrode and grating shaped electrode, assuming a plane wave illumination. On the left there is Au planar electrode from -6 to $-5 \mu\text{m}$ and on the right from $x=5 \mu\text{m}$ there is a grating electrode of 50 nm thick Au with a pitch of 200 nm . (a) Top view of the photoconductive switch, the color indicates the laser intensity at a depth of 10 nm below the surface, integrated over a bandwidth from 750 to 850 nm . (b) Cross section of the photoconductive switch showing the depth-dependence of laser intensity. The color indicates the intensity integrated over the y axis. The figure clearly shows the significant intensity enhancement directly underneath the grating electrode. The arrow in (a) indicates the polarization of the laser

From the FDTD calculations we determined the amount of light absorbed in the LT-GaAs layer. The FDTD calculation is performed with and without a glass spacer layer above the photoconductive switch. In case a $1 \mu\text{m}$ glass spacer layer between the ground plate and deflector/feed plate is kept at the location of the photoconductive switch, 77% of the 800 nm incident light would be absorbed by the LT-GaAs layer. Due to an applied wet etch, indicated in Figure 5.3e, glass above the GaAs and metal electrodes will be removed, which results in a drop of amount of light absorbed in the GaAs layer to 55% .

5.3.2 Fabrication of the photoconductive switch with grating electrodes

Fabrication of the grating requires electron beam lithography (EBL) as the dimension of the grating are in the hundreds of 100 nm range. The grating consists of 100 nm lines, with a 200 nm pitch. In the same lithography step we define the deflector and feed electrode in combination with a contact pad. The pattern written with EBL is shown in Figure 5.5. A positive resist AR 6200.09 with a thickness of 250 nm and a dose of $225 \mu\text{C}/\text{cm}^2$ is used, proximity correction is used to define the grating structure properly.

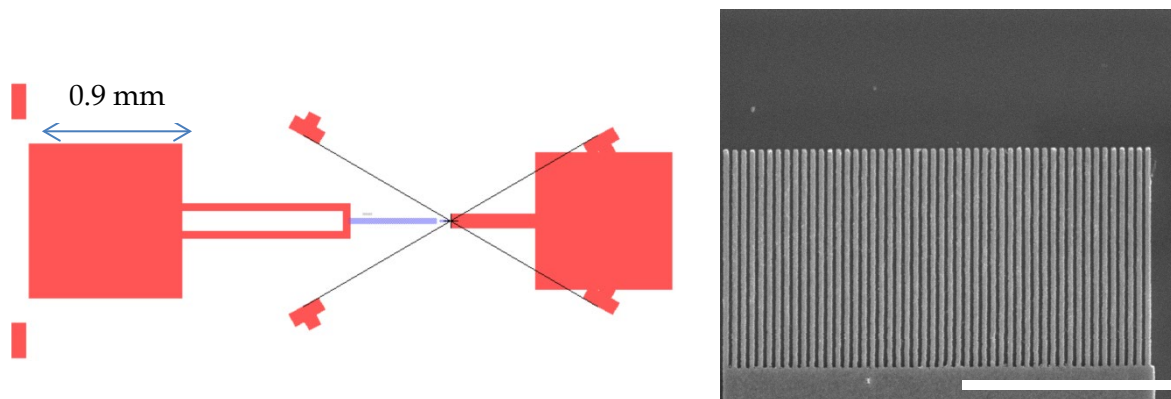


Figure 5.5: In red/blue the area exposed with the electron beam. The 0.9 mm square is the contact pad, the "T" shapes are dicing markers, the contact pad on the right is used to measure the electrical response of the photoconductive switch. (b) SEM image of the Au grating electrode, the scale bar is equal to $5 \mu\text{m}$.

According to the literature a native insulating oxide layer forms on the GaAs surface [5], so a short clean with BHF is advisable, or alternatively a 10% solution of Ammonium hydroxide for 10 s, just before e-beam evaporation. [6] We employed a 120 s Argon sputter etch just before e-beam evaporation to physically remove the oxide layer, at an ion beam energy of only 200 eV to prevent doping the LT-GaAs with Argon ions. [7] Subsequently an adhesion layer of 5 nm Cr followed by 50 nm of Au at a rate of 0.5-1 Å/s is evaporated. The device is now in the state depicted in Figure 5.3a, and the electrode is shown in Figure 5.5. The resulting dark resistance is measured and shown in Figure 5.6. Non-ohmic behavior is visible around bias voltages of 1 V and the magnitude of the dark resistance is around 2 GΩ. With the deflector plate capacitance of 7 fF this results in an RC time of 7 μs. From this we conclude that the dark resistance is high enough for a MEMS UFB.

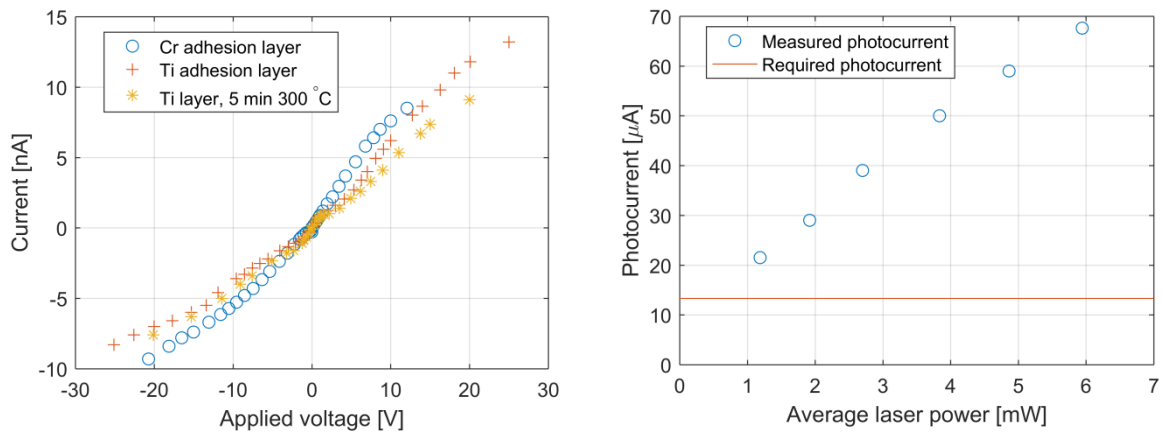


Figure 5.6: (a) Dark current through the photoconductive switch as function of voltage applied on the deflector electrode with the feed plate electrode grounded, in case of a 5 nm Cr adhesion layer and a 5 nm Ti adhesion layer, the Ti adhesion layer is also annealed for 5 minutes at 300 °C. The dark resistance of the photoconductive switch is in the order of 2 GΩ and is not significantly different in case a Cr adhesion layer is used. (b) Photocurrent when illuminated with p-polarized light using a Ti adhesion layer, the laser spot is located at the anode and a fixed 20 V bias is applied over the photoconductive switch. The laser is focused in a spot size of about 10 μm. The red line indicates the average required photocurrent to (de)charge the deflector plate with a capacitance of 7 fF at a rate of 95 MHz.

Figure 5.6a shows that if a Ti adhesion layer would be used instead of Cr, the dark resistance is comparable. Also, in Figure 5.6b we see that the photocurrent when illuminating the grating with femtosecond laser pulses is slightly lower than that measured by Berry *et al.* [4] Another important observation is that enough charges diffuse to the electrode, ensuring that the voltage at the deflector plate can be inverted when a femtosecond laser pulse illuminates the photoconductive switch.

5.4 Fabrication and quality control of the MEMS deflector

5.4.1 Microfabrication process of the deflector

The MEMS deflector needs to be accessible for the electron beam and the main challenge is to keep the aspect rotation low so that the rotational alignment with respect to the electron optical axis is feasible. To this end, the chip is diced, with a wafer dicer, in a triangular shape and the deflector is fabricated at the tip. The chip is protected with a layer of 1 μm S1813 photoresist during the dicing process mainly to protect the metal electrodes, see Figure 5.3b. The wafer

dicing parameters are optimized to reduce chipping, we found that 20,000 rpm and a feed speed of 0.5 mm/s is optimal. A typical dicing result is shown in Figure 5.7.

Monolayers of the photoresist can remain on the surface of the chip and cause adhesion problems for the BHF wet etch in the final process step, so complete removal of S1813 photoresist is essential. An O₂ plasma etch at 1000 W and 0.5 mbar pressure for 8 minutes is repeated 3 times to strip the photoresist layer.

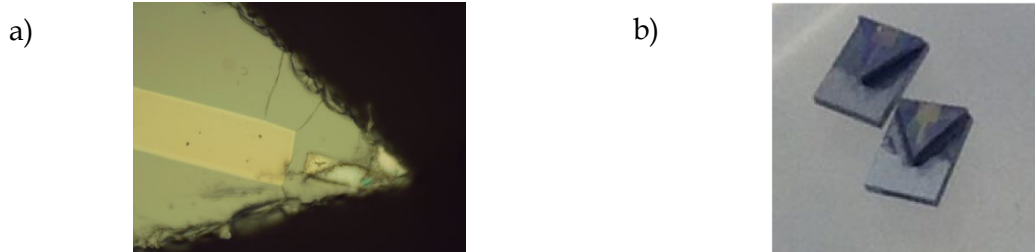


Figure 5.7: (a) Optical reflection microscope image of the chip, the LT-GaAs is green, the Mo electrodes have a yellow color. (b) Photograph of the LT-GaAs chip glued on a 3 by 4 mm Si chip. The figure shows the chip at the processing step indicated in Figure 5.3b.

The triangular shaped GaAs chip is hard to handle and manipulate with tweezers so before the other subsequent fabrication steps, the chip is glued on a 3 by 4 mm Si chip with Araldite 2020, as shown in Figure 5.7b.

The wafer dicer is not accurate enough to remove the GaAs around the deflector electrode. Therefore a FIB mill process is used to create a channel in the chip, as shown in Figure 5.8. The FIB mill defines the exact length of the deflector electrode, which should be 15 μm to get a deflector plate capacitance of 7 fF according to the COMSOL simulations presented in Chapter 4. The chip is now in the state schematically depicted in Figure 5.3c.

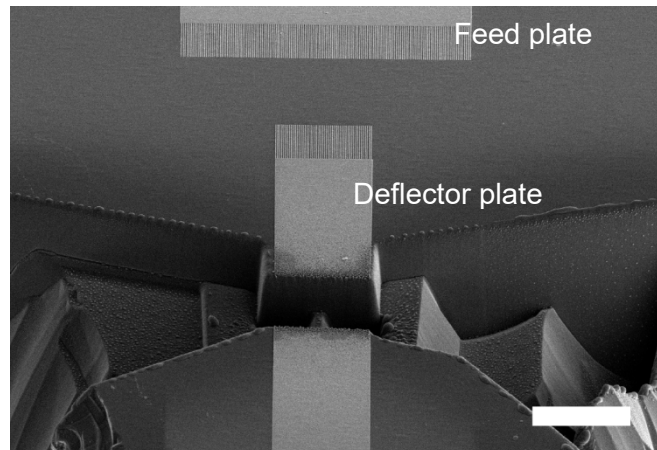


Figure 5.8: SEM image under 45 degrees of the trench milled with a FIB. The ratio between the length of the trench and the depth should be at least 10, an acceleration voltage of 30 kV and currents in the range of 2-20 nA are used. The FIB mill is performed under an angle of 8 degrees, some redistribution is visible but the photoconductive switch and deflector electrode do remain intact. The image is taken after processing step c, as indicated in Figure 5.3. The scale bar is 10 μm

A 1 μm thick spacer layer of SiO₂ is deposited in 16 minutes with Plasma Enhanced Chemical Vapor Deposition (PECVD) at a pressure of 1 Torr and at 300 degrees Celsius. The SiO₂ layer determines the spacing between the blanker plates and electrically separates the ground plate from the deflector and feed electrodes. A good adhesion between the SiO₂ layer and GaAs is

important. Tests have indicated that PECVD deposition at reduced temperatures or at faster rates will result in ripping off the Mo top layer during the BHF wet etch. The plasma bends around the edges of the chip and causes increased deposition at the edges. We prevent this by surrounding the chip with an aluminum plate, indicated in Figure 5.9.



Figure 5.9: Image of the circular Al metal plate in the PECVD machine (left) after deposition of Glass, in the centre the chip is visible (right). In this way we ensure that the plasma 'sees' a flat surface.

The whole device is coated with a 200 nm Mo layer, this metal layer is used as an electrical ground plate and prevents charging of the device and reduces the out coupling of RF fields applied on the electrodes, see the top layer in Figure 5.3d. The contact pad is manually covered with resist by using a resist pen, indicated in Figure 5.3d, before the coating with Mo. Sputter coating is used to deposit the Mo layer, with a recipe developed by Martin Kamerbeek. This recipe is optimized for reducing stress in the deposited Mo layer with a measured value below 250 MPa tensile stress. Note that the stress at the edge of the chip may be different. Sputter coating is a method with good step coverage so that the sides of the chip will also be coated with a conductive Mo layer. The chip is now in the state schematically depicted in Figure 5.3d. In the subsequent steps the glass between the blanker plates and above the contact pad is removed, as is the metal layer at the photoconductive switch.

The Mo layer at the sides of the blanker, i.e. the points where the electron beam enters and leaves the deflector, is removed with a FIB mill, these points are indicated with red circles in Figure 5.10. Also the Mo layer above the photoconductive switch is removed with a FIB mill. Milling of the Mo layer above the photoconductive switch could in principle also be done after the BHF wet etch of glass, which would reduce the optical reflection losses as the SiO_2 at the switch is not etched away. However, the risk is that the SiO_2 is etched away by BHF and the GaAs of the photoconductive switch would be contaminated with Gallium during milling and that the grating shaped electrodes might also be damaged.

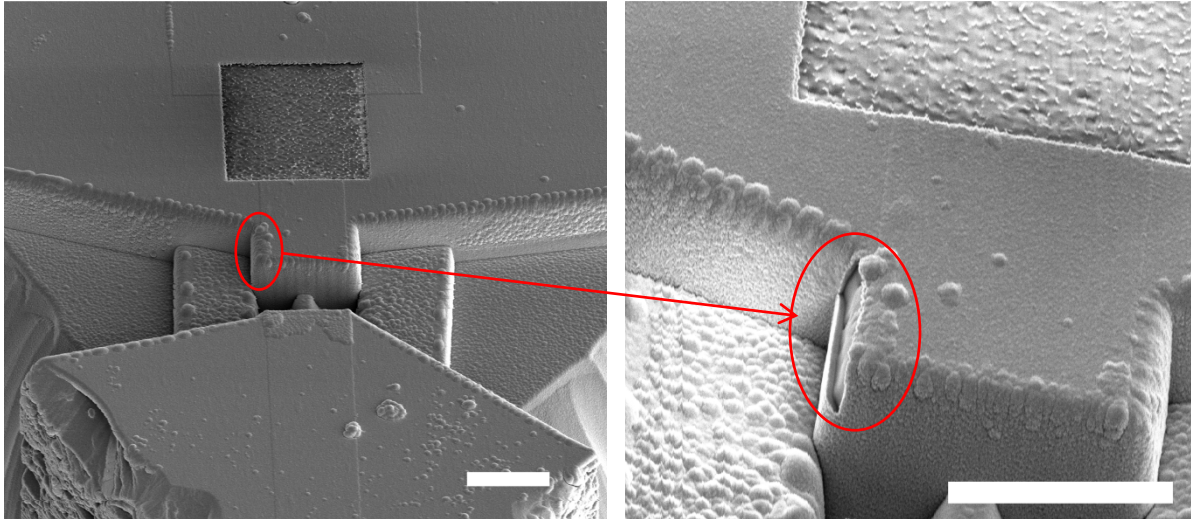


Figure 5.10: (a) SEM image of the blanker chip, in the state as sketched in Figure 5.3d, the Mo layer above the photoconductive switch is removed with a FIB mill process. (b) SEM image where the Mo layer at the left side of the deflector (inside the blue ellipse) is removed, subsequently the Mo layer on the right side will also be milled away. SE images are collected throughout the FIB mill to determine when the Mo layer is etched away.

The resist above the contact pad is removed with acetone and the whole device is dipped in IPA afterwards.

A wet etch process of 6 minutes in a buffered oxide (BHF), 7:1 diluted, followed by a thorough water rinse, removes glass between the deflector plates and the SiO₂ above the contact pad. There is a risk that metal particles released by the wet etch short the feed and ground plate, which is checked with an ohmmeter. The final result after MEMS fabrication is shown with a SEM image of the UFB in Figure 5.11a.

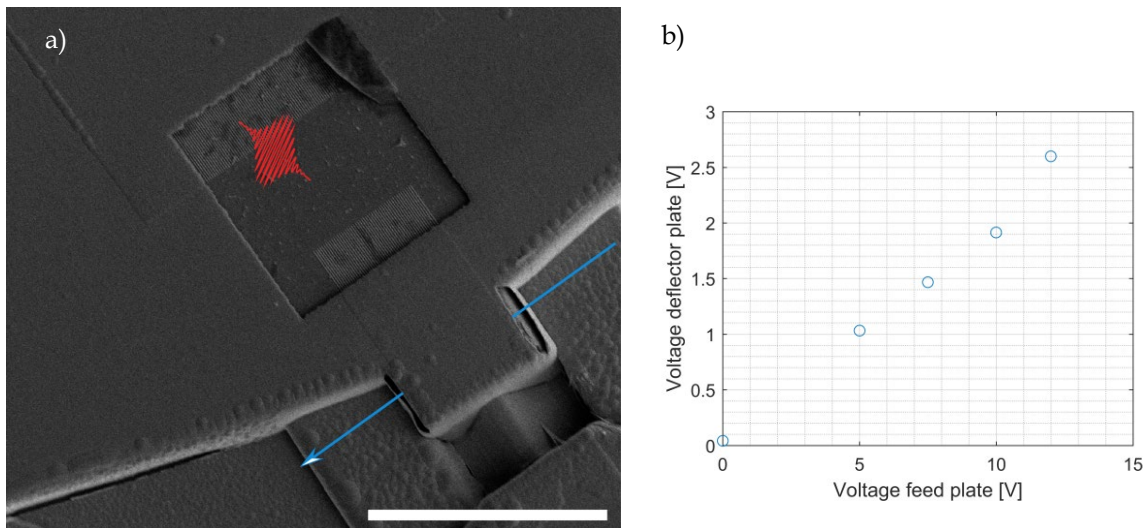


Figure 5.11: (a) SEM image of the final device. Blue arrow indicates the electron beam trajectory, red wavepacket indicates the photoconductive switch and the grating electrode is visible at the feed plate and deflector plate. The scale bar is 20 μm . (b) Voltage contrast measurement, a negative DC voltage is applied on the feed plate and from the grey level in the image the voltage at the deflector plate is inferred, the measurement clearly shows that most of the voltage drop occurs over the photoconductive switch, which has a resistance a factor 4 higher than the resistance between the deflector plate and ground.

5.4.2 Deflector voltage and resistance measurements

A basic functionality check of the device is executed by applying a constant DC voltage on the feed plate and to measure the resulting deflector plate voltage with voltage contrast in a SEM. Voltage contrast in the SEM is a change in SE yield induced by an applied voltage. We use this method as it is difficult to measure with a probe because of the micrometer dimensions. The change in SE yield at the feed plate as a function of applied voltage is used as a calibration, so the measured SE yield at the deflector plate can be related to the deflector plate voltage.

The result is shown in Figure 5.11b. It is clear from this figure that about 2/3 of the voltage drop occurs over the photoconductive switch and the rest over the resistance between the deflector plate and surrounding ground plates. Due to the complexity of material composition and geometry of the device it is not possible to (numerically) calculate the conductivity between the different electrodes. Nevertheless, the measurement clearly indicates a high enough resistance between the deflector plate and ground plate to maintain a voltage at the deflector plate.

In order to determine the dark resistance of the photo-switch and the resistance of the deflector plate to ground, we model the UFB with the circuit drawn in Figure 5.12. The transfer function of the MEMS UFB from feed plate to deflector plate is measured by deflection of the electron beam when a sinusoidal voltage sweep is applied on the feed plate. This is possible because the deflection angle is linearly related to the voltage at the deflector plate. From our model, the transfer function, i.e. the ratio of the voltage at the feed, V_0 , and deflector plate, V_{def} , would be given as:

$$\begin{aligned} \frac{V_{def}}{V_0} &= \frac{1}{\sqrt{\beta^2 + \omega R_{s,off} C_{def}^2}} \\ \left. \frac{V_{def}}{V_0} \right|_{f=0} &= \frac{R_{def}}{R_s} = \frac{1}{\beta} \end{aligned} \quad (5.1)$$

were the variables and assumed electrical circuit are defined in Figure 5.12 and β which is the ratio of V_{def}/V_0 at 0 Hz, determined from the voltage contrast measurement in Figure 5.11b.

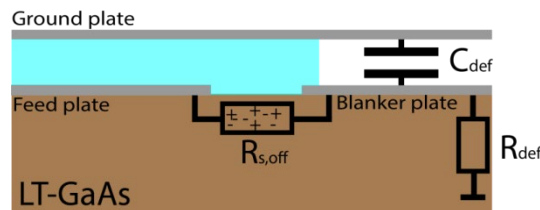


Figure 5.12: Schematic of the circuit of which the transfer function is described in equation (5.1). The photoconductive switch in dark state is modelled as a resistance of $R_{s,off}$. The deflector is modelled as a capacitor, C_{def} , a resistance R_{def} is present between ground and the deflector electrode. The metal electrodes are modelled as perfect electrical conductors.

Deflection of the electron beam is measured with a YAG scintillator screen, the SECOM platform collects the light with a light objective lens and is magnified and imaged on a camera. [8] The acceleration voltage of the electron beam is 6.5 kV, a 20x magnification water immersion light objective lens and tube lens are used to collect the CL.

The frequency dependent deflection data is fitted to a circuit model of the MEMS blanker, the details are discussed in Appendix A, the result is shown in Figure 5.13. A value of about 10 M Ω is determined for $R_{s,off}$ and about 3 M Ω for R_{def} . The data and fit of the model is shown in Figure 5.13. Numerical calculations indicate that the capacitance of the deflector is 6.6 fF. Thus, with an R_{def} of 3 M Ω , an RC time of 22 ns is obtained. This should be sufficient as the laser repetition time is 10 ns, i.e. the photoconductive switch will be back to dark state before the feed plate voltage is inverted (which occurs between 2 laser pulses).

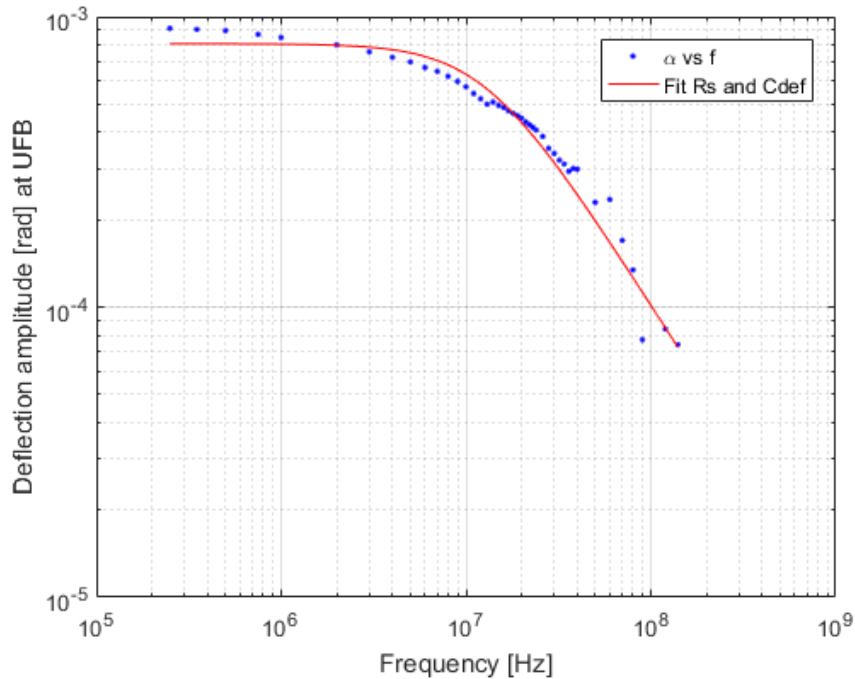


Figure 5.13: Deflection angle induced by the UFB as function of frequency by a sinusoidal voltage applied on the feed plate, the applied peak to peak voltage is about 3 V. The blue dots are measured deflection values and the red line is a fit as described by equation (5.1), the deflection angle and voltage are proportional.

The fabrication procedure discussed in this section clearly shows that the photoconductive switch and deflector can be integrated in a single MEMS device, see Figure 5.11. In the subsequent section of this chapter the integration of the chip in an EM to test the performance is described.

5.5 Design blanker stick and alignment laser

5.5.1 Design of the blanker stick

The advantage of the MEMS blanker is that it is so small that it can be inserted via standard entry ports in both TEMs and SEMs, normally used for aperture strips, sample holders and standard beam blankers. The opening diameter for that type of entry port is only 6.4 mm in case of a FEI microscope. In this section we describe the requirements and design of a dedicated blanker stick which fits in such a standard entry port.

The requirement for the blanker stick is that it has to guide the laser beam into vacuum via a window to the blanker chip and focus the laser beam on the 10 by 10 μm wide photoconductive

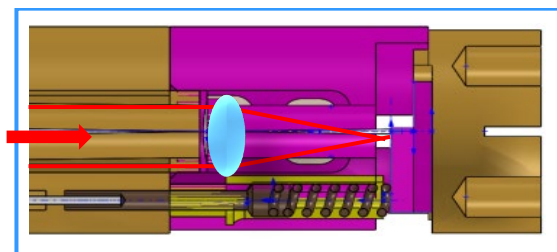
switch. Also, a coaxial feedthrough is required to guide the electrical feed signal to the contact pad of the photoconductive switch. The combination of these 2 requirements in combination with the limited space available poses a technical challenge. A possibility to replace the blanker chip is also required, because the chip can get damaged or not perform as expected. Another requirement is a means to mechanically move the blanker in the plane perpendicular to the electron optical axis, i.e. the x-y plane, in order to align the blanker to the electron optical axis. For this the standard FEI system is used, which has also axial rotation. Due to the low, 1:10, aspect ratio of the MEMS UFB no alignment is needed along the rotation axis perpendicular to axial axis.

The design of the blanker stick is shown in Figure 5.14. A beam splitting mirror is used to couple the laser into the blanker stick, which allows a camera to be used to image the MEMS UFB and laser spot to assist in the alignment. The field of view (FOV) needs to be large enough to do so. For this reason, the light pipe between the vacuum window and optical lens has to be as wide as possible, while the maximum diameter of the blanker stick is decreasing from 10 mm to 6.4 mm. Hence the light pipe is tapered, as depicted in Figure 5.14. Due to the limited FOV, the blanker chip has to be mounted quite accurately with an accuracy of about 50 μm with respect to the optical axis.

a)



b)



c)

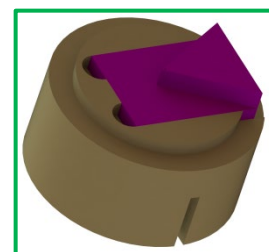


Figure 5.14: a) CAD drawing of the blanker stick. Via a beam splitter (BS) and vacuum window the laser is coupled into the blanker stick. A coaxial cable is connected to the contact pad on the blanker chip. b) Zoom-in of the end of the blanker stick (blue area in (a)). A 2 mm diameter, 0.15 NA, Newport KGA430-B aspheric lens focuses the laser beam on the photoconductive switch. c) Picture of the replaceable blanker holder (green area in (a)) with the blanker chip glued with silver paint in this holder. The holder is made such that the photoconductive switch is in the centre ($<100 \mu\text{m}$). The blanker holder is glued with Stycast 1266, so the holder can be removed when needed.

5.5.2 Blanker mounting and alignment of the laser optics

Proper alignment between the optical lens in the blanker stick and the photoconductive switch is required to minimize reflection losses in the blanker stick and to get the chip in the focal

plane. First, we ensure that the laser beam is aligned with respect to the optical axis with a set of pinholes, schematically depicted in Figure 5.15.

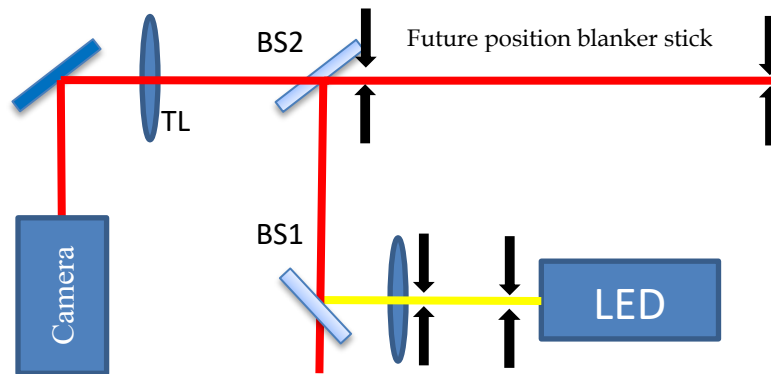


Figure 5.15: Schematic of the optical setup to align the laser into the blanker stick. The laser enters from below BS1 and is directed with a 80% reflecting beam splitter (BS2) through a set of apertures to properly align the laser path. A yellow LED source illuminates the chip and couples into the beam line via a 25% reflection beam splitter (BS1) at 800 nm, to create a reflection image of the blanker chip with a 125 mm tube lens (TL) onto the Guppy CMOS camera.

Secondly, the blanker holder is connected to a XYZ translation stage. The XYZ translation stage moves the MEMS UFB blanker into the centre of the optical axis. The blanker holder is glued with Stycast 1266 to the blanker stick and dries for 24 hours. The contact pad and coaxial cable are connected with conductive silver paint.

As shown in Figure 5.15 the laser pulse propagates through several optical components and the blanker stick before illuminating the photoconductive switch inducing reflection losses. The total transmission of the optical components and blanker stick is measured to be some 20%, and 47% if a positive 500 mm lens is used.

5.5.3 Mounting of the blanker in the SEM and electron optics alignment

An FEI Quanta FEG 200 SEM is used to test the chip. The blanker stick is inserted in the entry port normally used for a commercial beam blanker. We use the SEM as depicted in Figure 5.16a. Normally there is a variable aperture (VA) present above the UFB, to set the opening angle of the electron beam. Because of the close proximity, about 10 mm and the required half-opening angle of about 0.2 mrad, the VA is hard to use. For this reason the 500 μm differential pumping aperture is replaced with a smaller 40 μm aperture.

The gun shift/tilt coils are used to scan the electron beam over the blanker plates. The C2 lens excitation, see Figure 5.16a, is adjusted such that a sharp negative image of the blanker is obtained. A sharp negative image of the UFB in combination with a sharp image of the sample indicates that the blanker is in a conjugate focal plane. In that case the electron probe size is about 100-200 nm at the position of the blanker, smaller than the 1 μm separated deflector plates. The blanker has to be in conjugate mode, to prevent sweeping of the electron beam over the sample plane while deflecting the electron beam. For proper alignment of the SEM, the blanker has to be retracted and the gun shift coils are used to align the electron beam through the centre of the objective lens. Subsequently the blanker can be shifted back and also be aligned with respect to the electron optical axis by mechanical means up to a few micrometer accuracy. A small final shift of the electron beam is done with the gun tilt/shift coils to align

the electron beam between the blanker plates. The result of this alignment procedure is shown in Figure 5.16b and Figure 5.16c. no degradation in the resolution of the SEM is observed when the UFB is inserted. We note that in this image the UFB is made via the process described in the previous sections except that the deflection electrode was made of evaporated Mo instead of Au.

The MEMS UFB is only exposed to the electron beam after pumping down for about 8 hours and at pressures below $2.5 \cdot 10^{-6}$ mbar to ensure minimal contamination of the blanker plates. Adsorbed volatile material at the blanker plates can decompose under influence of the electron beam and leave non-volatile material on the blanker plates. This we have encountered once when exposing the MEMS UFB to the electron beam directly after pump down.

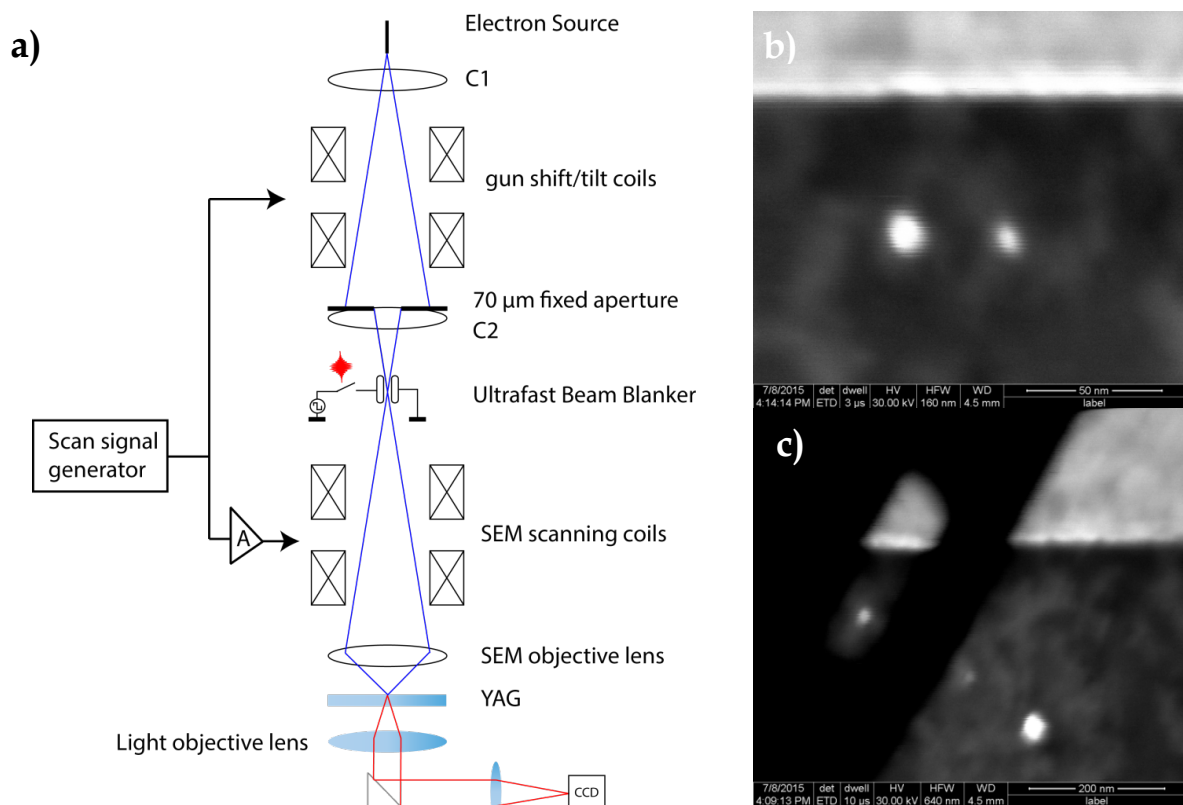


Figure 5.16: (a) Schematic of the SEM column. The electron beam is focused between the blanker plates by the condenser lenses. The gun shift/tilt coils scan the electron beam over the blanker and simultaneously, the standard SEM scanning coils scan the electron beam over the sample. In this way we generate, simultaneously, a negative image of the UFB and a normal image of the sample. (b) SEM image with a retracted blanker at a beam current of about 4.7 nA, an acceleration voltage of 30 kV and (c) SEM image with the blanker inserted. The resolution is largely maintained when inserting the blanker.

The laser is aligned on the photoconductive switch by using a camera, see Figure 5.17.

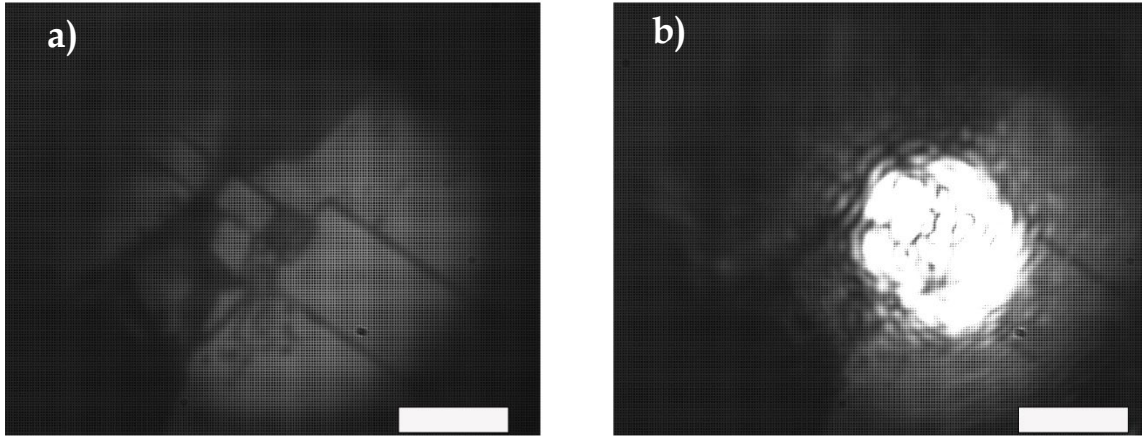


Figure 5.17: (a) Image of the UFB in the SEM, the photoconductive switch is the black square in the centre of the image. (b) The laser aligned onto the photoconductive switch. We calculate the laser spot size to be about $10\ \mu\text{m}$, using geometrical optics. The laser spot size on the image appears to be $\sim 40\ \mu\text{m}$. At an acceleration voltage of $30\ \text{kV}$, spot number 1, a C2 lens excitation of about $0.48\ \text{A}$ is required. The scale bar is $30\ \mu\text{m}$.

5.6 Initial characterization electron pulse length and performance

An in-house developed streak camera, described in [9] and Chapter 2 of this thesis, is used to investigate the performance of the UFB MEMS chip. The deflector of the streak camera is directly located below the pole piece, as indicated in Figure 5.19a. When used as a streak camera the sample is replaced by a YAG screen. The deflection of the electron beam is then imaged with an inverted optical microscope underneath the sample, called the SECOM system. The SECOM platform has been developed in our group and is extensively described in [8], [10], and in Chapter 2. The streak camera converts the temporal profile of an electron pulse into a spatial one by sweeping the electron beam over the YAG screen.

In the experiment described here, a continuous beam from the Schottky source is deflected in one direction by the UFB and in the perpendicular direction by the streak camera. A square wave of $-5\ \text{V}$ to $+5\ \text{V}$ with a rise time of about $2\ \text{ns}$ is applied to the deflector plates of the streak camera. A $-10\ \text{V}$ to $+10\ \text{V}$ square wave is applied at the feed plate of the UFB, the signal inverts between each subsequent laser pulse, the time τ between the laser pulse and square wave at the voltage plate is varied. The experiment will show whether the laser pulse induces the switch to a conductive state. The result is shown in Figure 5.19b/c, notice that the total deflection amplitude and deflection speed (indicated by the blue gaps in Figure 5.19c) increase when the switch is illuminated with laser pulses. It should be noted that the deflector plate voltage is not in phase with the feed plate voltage when the laser is off due to the capacitance of the deflector plate, see Figure 5.12, the square wave has a frequency of $47.5\ \text{MHz}$ and Figure 5.13 shows that the amplitude transfer is reduced more than $3\ \text{dB}$, hence the phase delay will be about 90 degrees, as plotted in Figure 5.18. Hence at certain time intervals the voltage at the feed plate and deflector plate will be inverted with respect to each other.

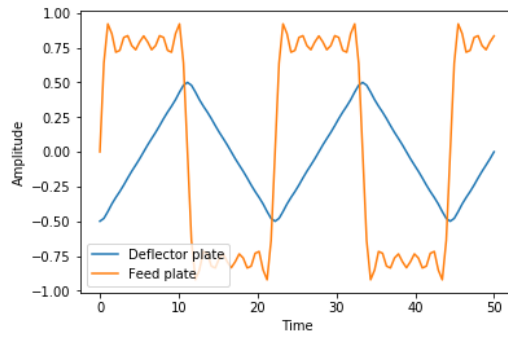


Figure 5.18: Schematic of the voltage applied at the feed plate (orange color) and the responding voltage at the deflector plate assuming resistance and capacitance values derived from Figure 5.13. The amplitude of the deflector plate voltage is higher than in reality for illustrative reasons.

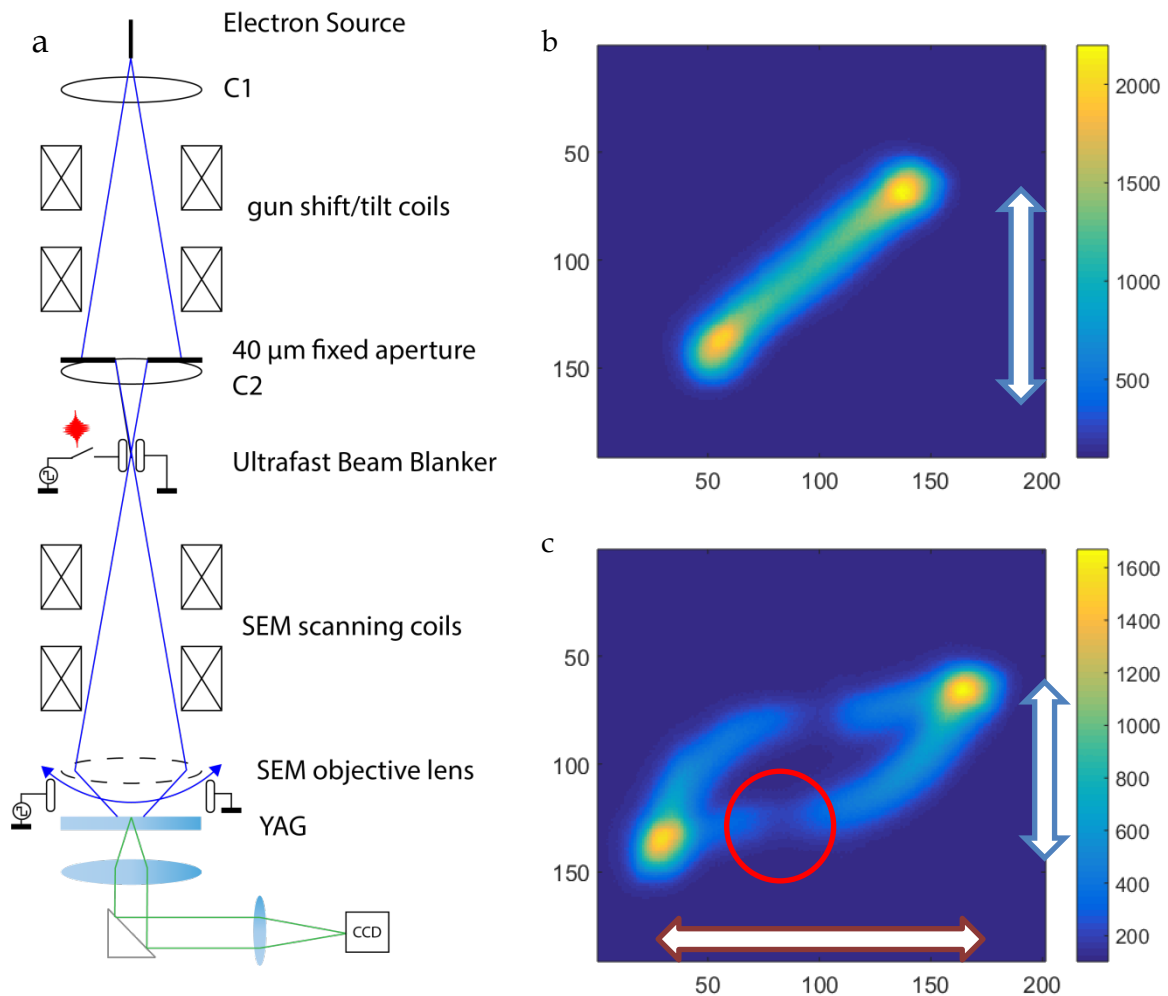


Figure 5.19: (a) Schematic of the SEM column, the final lens excitation is such that the beam on the YAG screen is only weakly focused, such that the deflection of the electron beam can be imaged with a camera. A 20x 0.75 NA optical objective lens is used below the YAG to have a reasonable FOV and relatively high light collection efficiency. (b) Deflection of the electron beam induced by the streak camera (blue arrow), when the photoconductive switch is not illuminated by the laser. Deflection in perpendicular direction is caused by the square wave voltage applied on the feed plate which is transferred to the deflector plate, the temporal alignment between the streak camera and deflector plate voltage is such that both invert voltage at the same time, hence the streak has the shape of a line. (c) Same as (b) but the switch is illuminated by laser pulses so deflection is induced by the laser (red arrow), simultaneously the beam is deflected by the streak camera (blue line). The alignment of the laser is optimized by maximizing the deflection amplitude. Time is counter clockwise in (c), the length of the blue arrow corresponds to about 2 ns [9], the length of the red arrow is about 3 ns, this is determined from Figure 5.20 where the arrival time of the laser pulse is shifted by 1 ns. It was found that the 2 lighter blue spots (of which the bottom one is indicated with a red circle) disappear when the laser beam is blocked, hence the pattern reads as follows: The yellow spot in the bottom left is a parking spot of the beam. From here, the beam follows the inversion of the feed plate, which is now faster than in (b) due to the presence of remaining photoconductivity of the switch as $e-h$ pairs created by a previous laser pulse are still present. When the pulse illuminates the switch the beam sweeps more rapidly (indicated by the red circle) and deflects afterwards slowly to the parking spot in the top right of the image. Both (b) and (c) have the same pixel scale. The laser power on the photoconductive switch is estimated to be a few mW, increasing the laser power by a factor 4 did not change the total deflection amplitude.

The deflection of the electron beam is induced by a combination of 2 effects, due to the finite dark resistance of the photoconductive switch the beam deflects when applying a square wave to the deflector plates, causing the deflection visible in Figure 5.19b, and also shown already in Figure 5.13. Secondly, when applying laser pulses, the beam deflects more rapidly due to the photoconductivity, this is a desired effect. Also the amplitude of the deflection increases, from Figure 5.13, it can be derived that a DC 10 V applied on the feed plate results in 2.3 V on the deflector plate. At 47.5 MHz the voltage at the deflector plate is reduced by another factor 5, see Figure 5.13. Hence when the laser pulses do illuminate the photoconductive switch the

expected increase in deflection amplitude between laser off (Figure 5.19b) and laser on (Figure 5.19) is expected to be a factor 20, the measured increase is only a factor 1.7. If the photoconductive switch goes slowly to the dark state the switch would effectively be always on and the deflection amplitude would still go up by a factor of 20 as the feed and deflector plate would effectively be shorted. The lower than expected deflection amplitude can either be caused by a too short recombination time which is somewhat unlikely as LT-GaAs has recombination times of at least a few 100 fs, while the manufacturer specified a recombination time of 15 ps. Another possibility is that the photoconductivity of the switch is too low or that the expected laser power on the switch is not sufficient, however we do not observe an increase in deflection amplitude when further increasing the laser power.

When comparing Figure 5.19b and c a more rapid change in deflector voltage is occurring before the laser pulse illuminates the switch. This indicates that the dark resistance of the switch is decreased by the laser pulses, which in turn indicates that the switch does not go back fast enough to its dark state.

Figure 5.20 shows the direction of time in the streak camera patterns, when the delay time τ is increased the voltage ramp on the UFB is delayed with respect to the laser pulse. Hence the laser induced gap in the streak pattern will shift closer to the starting point of the voltage ramp when τ is increased. Based on this reasoning, Figure 5.20b,c shows that the direction of time is counter clockwise in the streak camera images.

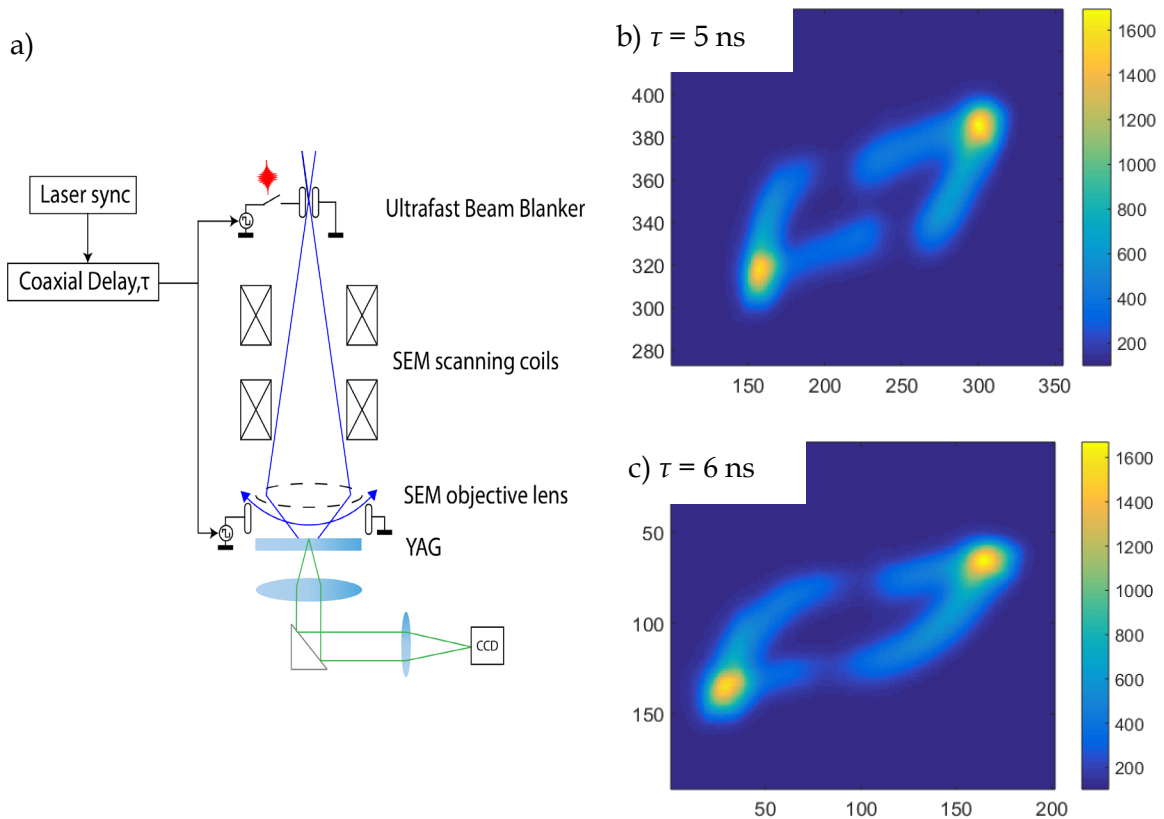


Figure 5.20 a) An electronic sync signal is derived from a photodiode in the laser, the sync signal is fed to a coaxial delay box delaying the laser sync, so triggering of the pulse generators for the UFB and streak camera are delayed by a time constant τ compared to the time a laser pulse illuminates the photoconductive switch. b) Streak camera pattern as in Figure 5.19c with a delay, τ , of 5 ns (set by the coaxial delay box) and (c) 6 ns. Notice that when the square wave of the pulse generator gets delayed in time with respect to the laser pulse the low intensity part of the streak (created by the laser) moves closer to the starting point of the voltage ramp, hence time runs counterclockwise in the streak camera figures. The figure also shows that at $\tau = 5$ ns that the photoconductivity is too low to fully invert the voltage at the deflector plate after the laser pulse.

In a subsequent experiment electron pulses are created with the MEMS UFB blanker. A blanking aperture is inserted in the pole piece to create the pulses. The electron pulses then excite Cerium atoms in a YAG screen, which decay under emission of a photon. These photons are collected and detected with an avalanche photo-diode (APD). A time-correlator builds up a histogram with photon counts as function of the arrival time of emitted CL with respect to the electron pulse[9], see Figure 5.21.

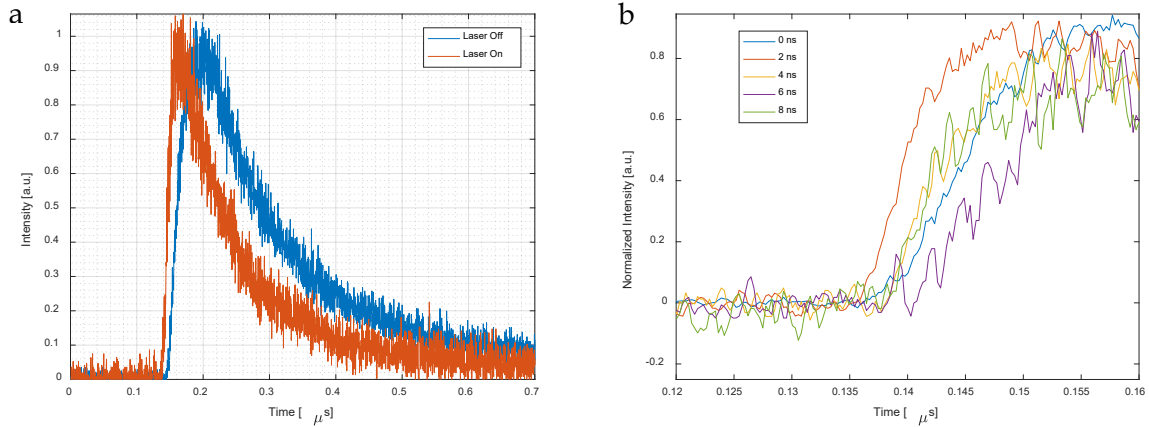


Figure 5.21: (a) Histogram of CL counts from the YAG screen as function of time with a pulsed electron beam created with the UFB, in case with the laser off (blue line) and with a 10 mW laser beam (red line). (b) Counts as function of time for different temporal delays between the laser pulse and the switching of the voltage at the feed plate, the trace shown in (a) is with a delay of 2 ns.

Electron pulses are observed also when the laser is off (see Figure 5.21a) in combination with a square wave applied over the feed plate, due to the dark resistance of the photoconductive switch [1]. In Figure 5.21a, the measured photon counts from the scintillator, exposed to electron pulses, are shown as function of time. This clearly shows that the CL signal rises faster and with earlier onset when the laser illuminates the photoconductive switch. Measuring sub 100 ps pulse durations is challenging with this method for two reasons: First, the peak emission of YAG is delayed by about 4 ns after excitation with an electron pulse, we also observe this with 100 ps short electron pulses created with a standard commercial beam blanker. Secondly, the APD in our setup has a time jitter of 350 ps.

Figure 5.21b shows that a shift in the temporal delay between the train of laser pulses and the square wave applied at the feed plate of the UFB causes a difference in rise time, indicating a change in the electron pulse length. The rise time is shortest at a delay of 2 ns, our interpretation is that the laser pulse then illuminates the switch at the moment the voltage difference between the deflector and feed plate is the largest and the photoconductivity causes the deflector plate to change voltage quickly. The rise time is slower at other delay settings, indicating that the deflector plate probably mainly changed voltage (around and before the zero crossing of the deflector plate voltage). Notice that the blanking aperture and UFB are not necessarily perfectly aligned with respect to each other, i.e. a non-zero voltage might be required at the deflector plate to transmit the electron beam through the blanking aperture, hence zero crossing of the voltage is defined as the voltage at which there is maximum transmission of the electron beam through the blanking aperture. Hence, the electron pulse length increases due to laser pulse illumination of the photoconductive switch while there is a zero crossing of the feed plate voltage signal, i.e. the effect of the laser pulse is reduced. A temporal shift in the zero crossing is also visible when the laser is illuminating the photoconductive switch, indicating a swifter inversion of the voltage at the deflector plate.

5.7 Discussion

The fabrication process described in this chapter to integrate a photoconductive switch and MEMS blanker utilizes a combination of a wafer dicer and FIB milling. GaAs is a difficult material in MEMS as there is no easy method to etch deep trenches with a high aspect ratio.

Fabrication of the device on a larger scale might require another method, it might be advantageous in the future to switch to a Si based process while still using a photoconductive switch made of LT-GaAs. For example Kai Ma *et al.* [11] have demonstrated the possibility to grow LT-GaAs on Si surfaces, others have succeeded to transfer micron sized pieces of LT-GaAs to a Si substrates. [12] Such a method could be adjusted and incorporated in our process flow.

The design of the photoconductive switch could be further improved for photoconductivity. Hybrid designs where a photoconductive switch is combined with an array of nano-antennas are shown to improve the in coupling of laser light into the GaAs and improve the thermal resistance. [13]

A rejection ratio (i.e. ratio of beam current after the blanking aperture to beam current before the deflector when a voltage sufficient to blank the electron beam is provided) of $2.7 \cdot 10^{-3}$ is measured, see Appendix B, for the beam blanker operating at 10 kV beam acceleration voltage, in combination with a 40 μm aperture at a distance of about 100 mm above the UFB hence the half-opening angle is about 0.2 mrad. For the given aperture size and beam energy, we used the lowest possible current and spot size in the blanker. At higher beam energies the rejection ratio might be better due to lower scattering probabilities and smaller probe sizes in the UFB. However, a 100 fs pulse will have a duty cycle of $1 \cdot 10^{-5}$ at 100 MHz repetition rate, significantly lower than the background due to the non-zero rejection ratio. Because we can measure this background signal the energy of the background electrons will be relatively high, small additional fields around the UFB to get rid of these electrons won't work. Probably the best option would be to install another blanker above the UFB. This blanker can park the beam between the electron pulses somewhere on the blanker chip between consecutive pulses. Duty cycles at 100 MHz of about 10^{-2} are required to get the signal and background at the same level, hence pulse lengths of about 100 ps are required. In principle a dedicated blanker can be inserted above the blanker chip at the location of the variable aperture stick, this blanker has to deflect a focused beam over only a couple of micrometres corresponding to deflection angles in the 0.1 mrad range. A deflection voltage of about 200 mV is enough, a signal with a rise time of 0.26 ns/V can do that in about 50 ps.¹

5.8 Conclusion

We have fabricated a MEMS UFB blanker integrated with a photoconductive switch, the photoconductivity is enhanced by grating shaped electrodes.

An insert for a commercial SEM has been designed and assembled which is used to align the MEMS chip with respect to the electron beam and is used to couple the laser beam into the vacuum and focus it on the photoconductive switch. We have aligned the chip with respect to the electron beam and laser beam. A small shift with the gun tilt/shift coils is enough to shift the electron beam next to the blanker and the system can be used in DC mode. This is an

¹ We assume that the blanker is located 10 mm above the UFB, has a length of 3 mm, a separation of 100 μm between the blanker plates and a beam energy of 30 keV.

advantage for practical use in ultrafast experiments because it enables to easily search for a point of interest at the sample with a relatively high DC current. Subsequently the electron beam can be brought in pulsed mode by shifting the electron beam between the deflector plates of the UFB and a time resolved experiment can be performed. An additional advantage of operating the SEM in non-pulsed mode is that it is relatively effortless to align the EM as there is an extensive amount of signal in DC mode.

We have demonstrated that illumination of the photoconductive switch with a laser beam causes a deflection of the electron beam. A custom made streak camera is used to demonstrate that the UFB produces electron pulses. The electron pulses are also measured with an avalanche photodiode and time-correlator. Exact values for the pulse length are not measured as the resolution is limited by the equipment, but both the measurements with the APD and streak camera indicate an upper limit of 0.5 ns. The resolution of the electron beam is maintained while traversing the MEMS UFB, the probe size is limited by stage vibrations and below 10 nm. This spatial resolution is acceptable for a SEM in general and good enough spatial resolution to measure nanophotonic systems and diffusion of charges well below the diffraction limit of light.

Streak camera patterns indicate that the photoconductive switch is still conductive 10 ns after and laser pulse, also the photoconductivity of the switch should be further enhanced and characterized. To conclude, we have shown laser induced deflection of the electron beam but in order to reach the anticipated pulse lengths both the photoconductivity and dark resistance need to be improved, as the deflection amplitude under illumination is about a factor 10 less than expected. Another effect which is to be ruled out is the possibility that a laser pulse enhances the conductivity between the deflector plate and ground. For this reason the carrier dynamics around the photoconductive switch should be measured, which could be done with time resolved EM in voltage contrast mode like in Figure 5.11. In such a measurement electron pulses are used to probe the time dependent voltages around the photoconductive switch. Electron pulses of sub 100 ps, as described in Chapter 2, would be sufficient to measure the carrier dynamics around the photoconductive switch in this way.

Bibliography

- [1] I. G. C. Weppelman, R. J. Moerland, J. P. Hoogenboom, and P. Kruit, "Concept and design of a beam blanker with integrated photoconductive switch for Ultrafast Electron Microscopy," *Ultramicroscopy*, vol. 184, pp. 8–17, 2017.
- [2] I. G. C. Weppelman, R. J. Moerland, L. Zhang, E. Kieft, P. Kruit, and J. P. Hoogenboom, "Pulse length, energy spread, and temporal evolution of electron pulses generated with an ultrafast beam blanker," *Struct. Dyn.*, vol. 6, no. 2, 2019.
- [3] a. Piotrowska, A. Guivarc'h, and G. Pelous, "Ohmic contacts to III–V compound semiconductors: A review of fabrication techniques," *Solid. State. Electron.*, vol. 26, no. 3, pp. 179–197, 1983.
- [4] C. W. Berry, N. Wang, M. R. Hashemi, M. Unlu, and M. Jarrahi, "Significant performance enhancement in photoconductive terahertz optoelectronics by incorporating plasmonic contact electrodes," *Nat. Commun.*, vol. 4, p. 1622, 2013.
- [5] V. L. Rideout, "A review of the theory and technology for ohmic contacts to group III–V

- compound semiconductors," *Solid. State. Electron.*, vol. 18, no. 6, pp. 541–550, 1975.
- [6] R. P. Vasquez, B. F. Lewis, and F. J. Grunthaler, "Cleaning chemistry of GaAs(100) and InSb(100) substrates for molecular beam epitaxy," vol. 791, no. 100, pp. 1–5, 1983.
- [7] P. Rabinzohn, G. Gautherin, B. Agius, and C. Cohen, "Cleaning of Si and GaAs crystal surfaces by ion bombardment in the 50 to 1500 eV range," *J. Electrochem. Soc.*, vol. 131, no. 4, pp. 905–914, 1984.
- [8] A. C. Zonneville *et al.*, "Integration of a high-NA light microscope in a scanning electron microscope," *J. Microsc.*, vol. 252, no. 1, pp. 58–70, Oct. 2013.
- [9] R. J. Moerland, I. G. C. Weppelman, W. H. Garming, P. Kruit, and J. P. Hoogenboom, "Time-resolved cathodoluminescence microscopy with sub-nanosecond beam blanking for direct evaluation of the local density of states," *Opt. Express*, vol. 24, no. 21, pp. 499–504, 2016.
- [10] A. C. Narváez *et al.*, "Cathodoluminescence Microscopy of nanostructures on glass substrates," *Opt. Express*, vol. 21, no. 24, pp. 29968–29978, 2013.
- [11] K. Ma, S. Member, R. Urata, D. A. B. Miller, and J. S. Harris, "Low-Temperature Growth of GaAs on Si Used for Ultrafast Photoconductive Switches," *IEEE J. Quantum Electron.*, vol. 40, no. 6, pp. 800–804, 2004.
- [12] X. Zheng *et al.*, "Femtosecond response of a free-standing LT-GaAs photoconductive switch," *Appl. Opt.*, vol. 42, no. 9, pp. 1726–31, Mar. 2003.
- [13] S. I. Lepeshov, A. Gorodetsky, A. E. Krasnok, E. U. Rafailov, and P. A. Belov, "Enhancement of Terahertz Photoconductive Antennas and Photomixers Operation by Optical Nanoantennas," pp. 1–19, 2016.

Appendix A – Characterization of the MEMS blunker by impedance

As discussed in the main text, the electrical properties of the MEMS blunker have been measured by measuring the deflection of the electron beam. A beam acceleration voltage of 6.5 kV is used, the deflection angle is linearly related to the voltage at the deflector plate.

For the MEMS UFB deflector there always has to be a crossover at the deflector, otherwise the beam cannot fit in between the 1 μm separated deflector plates. This requirement implies that the beam at the YAG screen is defocused in order to resolve the deflection amplitude. Hence the deflection will consist of a convolution of the voltage signal at the deflector plate of the UFB, a sinusoidal wave, and a defocused spot. A sinusoidal wave will be imaged as a line on YAG screen with an intensity I and coordinate x along the line:

$$\begin{aligned}
 x &= A \sin(\omega t) \\
 I(x)\Delta x &= I_0\Delta t = 2I_0 \frac{\Delta t}{\Delta x} \Delta x \\
 \frac{dt}{dx} &= \frac{1}{\omega A \sqrt{1 - \frac{x^2}{A^2}}} \\
 I(x)\Delta x &= I_0\Delta t = \frac{1}{\omega A \sqrt{1 - \frac{x^2}{A^2}}} 2I_0\Delta x \\
 I_0 &= \int_{-A}^A \frac{\alpha}{\omega} \frac{1}{A \sqrt{1 - \frac{x^2}{A^2}}} dx = \frac{\alpha}{\omega} 2\pi \\
 I(x) &= \frac{I_0}{2\pi A} \frac{1}{\sqrt{1 - x^2/A^2}}
 \end{aligned} \tag{5.2}$$

where A is the deflection amplitude, $I(x)$ the intensity in arbitrary units and I_0 the normalized intensity. The electron beam has a top-hat like profile as indicated in Figure 5.22a. In Matlab we calculated the convolution between the function $I(x)$, as defined in equation (5.2) and the normalized cross section of the electron beam profile for a range of deflection amplitudes A . From the convolution we determine the point where the convolved function is above 0.35 and define that as the peak to peak convolved deflection amplitude and use it to determine the real peak-to-peak deflection amplitude in the images.

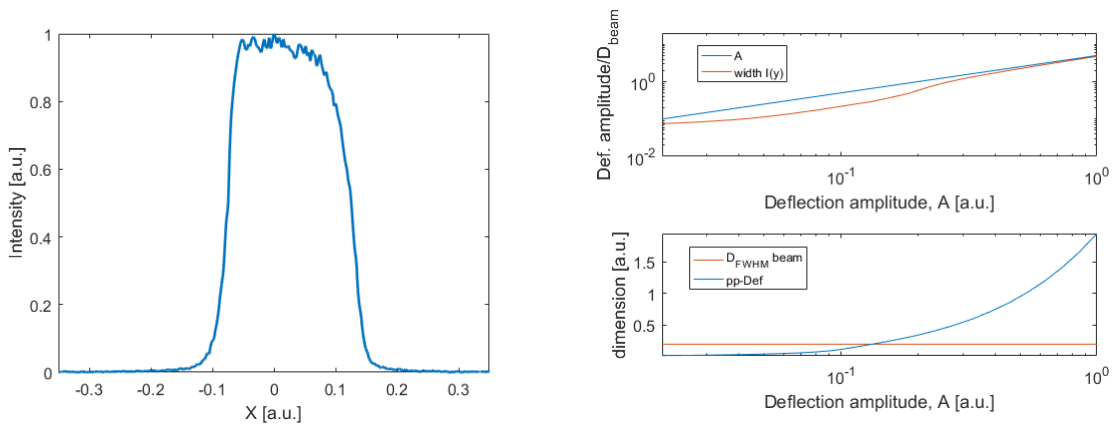


Figure 5.22: (a) Cross section of the beam spot on the camera, there is no time-dependent voltage applied on the UFB. The profile is convoluted with $I(x)$ defined in equation (5.2) and the width of the resulting line profile is plotted in (b), in combination with the blue line indicating A . (c) Corresponding variation of the deflection amplitude.

The deflection angle at the sample is calculated back to the deflection angle at the MEMS UFB blanker using the known half-opening angle at the UFB which is equal to 0.4 mrad.

Appendix B – Background signal elastically scattered electrons

The temporal resolution is not sufficient to measure the expected sub picosecond pulse lengths. However it is useful in order to check whether the pulse length is in the picosecond regime before switching to more cumbersome pump-probe experiments. Also we can easily discriminate the even and odd pulses arriving from the MEMS UFB.

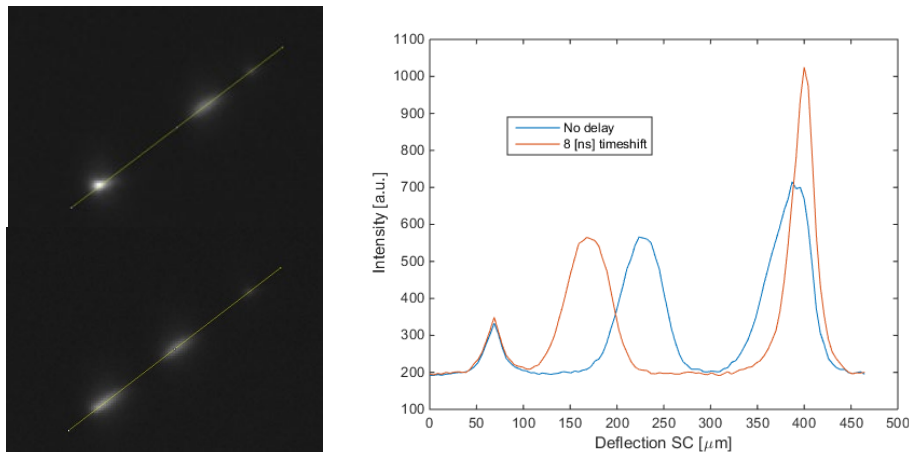


Figure 5.23 CCD image showing 3 spots, the profile along the yellow line is given in the right graph, red curve. Three spots are clearly visible, the center one is generated with a partially shorted photoconductive switch, no laser is used in this case. The left spot is generated by electrons who pass through the blanking aperture while the beam should be blanked by the photoconductive switch, demonstrating the non-zero rejection ratio of the UFB. The big spot on the right is the combination of the latter effect and the second electron pulse. In the blue curve the electrical signal on the streak camera is delayed with 8 ns, the corresponding CCD image is shown in the bottom right. The beam acceleration voltage is 10 kV, the duty cycle of the square wave applied on the UFB is 1 μ s.

In Figure 5.23 we show a test of the streak camera where a UFB chip is used with a photoconductive switch which seemed to be shortened. Hence, the blanker worked like a normal blanker the applied electrical signal is 'directly' transferred to the deflector plate. The word 'directly' is somewhat ambiguous due to the unknown conductivity of the photoconductive switch, we applied a voltage with a rise time of about 2 ns and the resulting electron pulse is 8 ns. However, the measurement shows the finite rejection ratio of the beam blanker. The distance of the UFB to the electron beam is small, hence some electrons can scatter with the UFB and be transferred through the blanker aperture. By calculating the ratios of the integrated intensities of the electron pulse and background (centre spot blue curve, Figure 5.23, and left spot respectively) a rejection ratio of $2.7 \cdot 10^{-3}$ is estimated. In reality the rejection rate might be worse due to the non-linear conversion to photons in YAG, low energy electrons absorbed in the conductive W layer above the YAG won't be detected. To put this number in perspective a duty cycle of 1.10^{-4} is expected for a 1 ps electron pulse at a repetition rate of 100 MHz. Hence the signal in a time resolved experiment will always be weaker than the background signal.

6 Valorisation and applications

In this thesis a new method to create femtosecond electron pulses has been developed. In our technique, see [1], a photoconductive switch is integrated with an electron blanker in a MEMS device that can be inserted into an existing commercial SEM. Possible advantages of this approach are:

- (i) Our ultrafast beam blanker (UFB) can be inserted into the SEM beam line via standard entry ports that are normally used for other accessory components like apertures and beam deflectors. Thus existing SEM users can upgrade their available SEM into an ultrafast-SEM by purchasing an accessory. This is obviously an attractive feature from a commercial point of view but it may also open the field of ultrafast-(S)EM to a wider group of users.
- (ii) A user can quickly switch between pulsed and continuous beam mode of operation. This is an important advantage because the current at pulsed mode will be low, hence the high current, continuous beam mode operation is preferred for finding the region of interest. As discussed in Chapter 4, the beam brightness in pulsed mode is the same as in the case of a continuous beam and the energy spread can be kept at low values compared to the energy spread of a standard high-brightness Schottky electron source.[2]
- (iii) The use of a photoconductive switch ensures a high-flexibility, i.e. the repetition rate is directly determined by the laser and the electron pulses are almost jitter-free locked to the laser pulse. The electron pulse length and hence the current can be varied by adjusting the laser illumination power and the voltage applied over the device, as shown in Chapter 3. [3]

In the previous chapters, we described calculations and computational studies of a MEMS sized UFB, the fabrication of a MEMS sized UFB, the incorporation in a SEM, the triggering of the UFB with a laser pulse, i.e. the deflection of the electron beam after illumination of the MEMS UFB with a laser pulse however sub picosecond electron pulses have not been demonstrated. To describe a path towards that goal and to discuss the path to a market ready product we discuss the status of our UFB in terms of Technology Readiness Levels (TRLs), or the process to go from conceptual idea to a market-ready product, in this chapter. TRLs indicate the sequence of steps that have to be taken in this process. We will then discuss the critical elements in the current design, potential disadvantages, and further considerations or potential improvements that have to be taken into account in the final steps towards a commercial prototype. In the remainder of the chapter, the feasibility of other potential applications, namely use in ultrafast-TEM, ultrafast-SEM, and in pulse compression will be discussed.

6.2 Valorisation

The process of going from a basic idea towards an actual product is complex and involves many different steps and considerations. For this reason so-called technology readiness levels (TRLs) are used to help making decisions concerning the translation of technology into actual products. The TRL scheme is widely used, e.g., by organisations like NASA, ESA, DOE, the oil and gas industry, or in the Netherlands by TNO. An example of such a TRL scheme is given in Table 6.1. The scheme can help in identifying what the status of a project is and what steps still need to be taken in the road towards valorisation, there is of course not necessarily a linear flow from TRL1 to TRL9. A project can be at a high TRL level while there are still open questions at a lower TRL level.

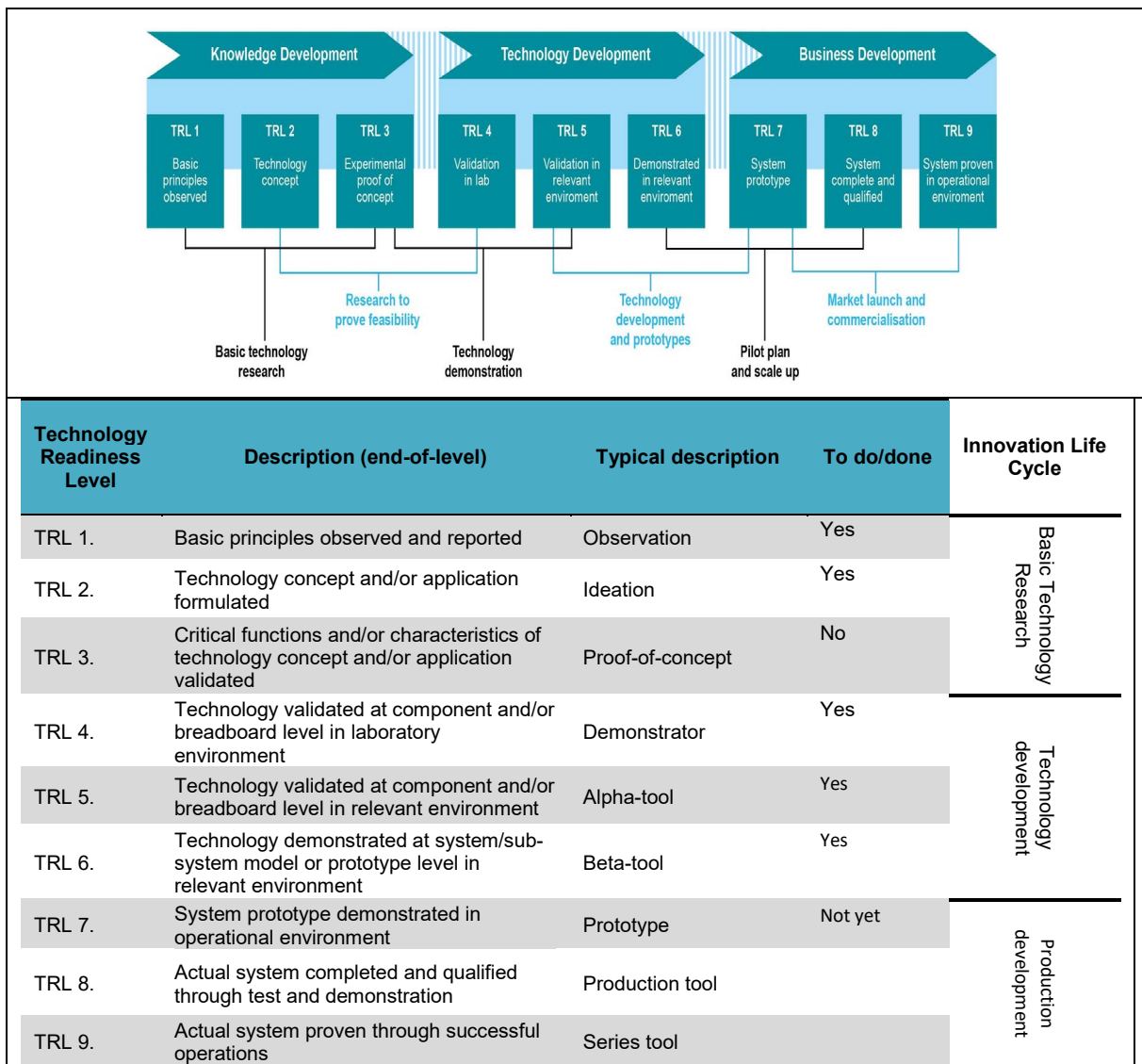


Table 6.1: Technology readiness levels (TLR) descriptions and status of the UFB, image courtesy from the TU Delft valorization center..

Regarding the actual basic technology research of our ultrafast blanker, quite some steps have been taken already. From the analytical and numerical calculations, discussed in Chapter 3 and 4 respectively, we know that the creation of sub picosecond electron pulse lengths is feasible, which is at TRL1/TRL2 level. In Chapter 5 a process flow is described to create a MEMS device integrated with a photoconductive switch. Essentially, this is a TRL3 step, as the

fabrication of the chip itself is already a critical aspect of the technology. The natural next step would be to measure with some relatively standard technique the (quantitative) change in voltage at the deflector plate as function of time. Optical techniques are hard for the reason they do require a pump-probe measurement of the refractive index at a high spatial resolution and it will be challenging to get quantitative data. Time-dependent voltage contrast would also demonstrate ultrafast voltage switching at the deflector plate, however femtosecond electron pulses will be required to perform such a measurement. A final option is to use an electron beamline and measure the deflection of the electron beam due to the voltage at the deflector plate. Building a beamline system with a good beam quality from scratch is quite some work but this can be reduced by the use of a commercial system. In our case, we used a Quanta 200 FEG SEM to carry out these characterizations. An important additional advantage of this choice is that the test-experiment is now conducted at the final system level in the relevant environment, which means that a tool at TRL6 level has been built to perform the proof-of-concept at TRL3 level. According to Table 6.1, the steps that have to be considered next then involve the translation from beta tool to actual prototype. The next section describes some of the design changes that we anticipate to be required to go towards a TRL7 level prototype. Further, we explore in a next section (6.2.2) the potential application and relevant considerations for use in Transmission EM (TEM) instead of SEM.

6.2.1 Towards a prototype - Design improvements

Design improvements are needed in both the processing steps of the chip production and the UFB holder. Critical elements in the current UFB design/beta tool are:

- Alignment and mounting of the blanker chip in the holder with respect to the light optical axis to ensure proper laser illumination of the photoconductive switch.
- MEMS fabrication with many individual steps, which can be prone to error/contamination, and may be complicated to scale to batch processing.

Potential disadvantages of the current implementation:

- The blanking aperture is inserted in the objective lens, thus fixing the opening angle limiting the beam current and the range of beam opening angles that can be used. It also limits the use of though-lens detectors. Also there is no mechanical means of aligning the aperture with respect to the electron optical axis.
- An additional aperture has to be inserted above the blanker to limit the opening angle in the blanker, which also reduces the beam current that can be achieved in continuous-beam mode.
- The blanker opening is very small ($1 \times 10 \mu\text{m}$), which may make the system sensitive to beam drift or mechanical drift of the blanker (which can typically be a few micrometer over a timescale of about 10-15 min). Some of it is potentially related to charging.

The alignment of the blanker chip with respect to the holder is quite critical and only a limited FOV is available. Also due to the small diameter of the blanker stick a misalignment of the laser beam can lead to a significant increase in reflection losses. The diameter of the entry port can be increased by either redesign of the aperture stick mechanism or by inserting a completely new column element somewhere below the last condenser lens. The latter would

have the disadvantage that it will be less easy to retrofit on a standard commercial EM, though newer generation SEM's columns can be designed which have by default more space.

A successful MEMS fabrication strategy requires the following outcome:

- Well functioning photoconductive switch, i.e. ohmic contact between the metal electrodes and the semiconductor and sufficiently fast decay of the photoconductivity to the dark state after laser pulse illumination.
- No electrical shorts between electrodes holding a voltage and ground.
- Contamination free and no electrical insulating layers close to the electron optical axis. The electron beam needs to be able to pass through the deflector, without charging issues.

The second and third requirement are relatively easy to check during the fabrication process with light and electron microscopes. The performance of the photoconductive switch is the most risky. In Chapter 5 we demonstrate that voltage induced SE can be used to quantify the voltage holding capacity of the electrodes surrounding the photoconductive switch. Ideally a pulsed electron beam would be used in combination of pulsed laser illumination of the switch, this would measure in a direct way the performance of the UFB. Subsequently this performance could potentially be related to parameters of the device which are more straightforward to measure like DC photocurrent, dark resistance of the switch and static SE contrast.

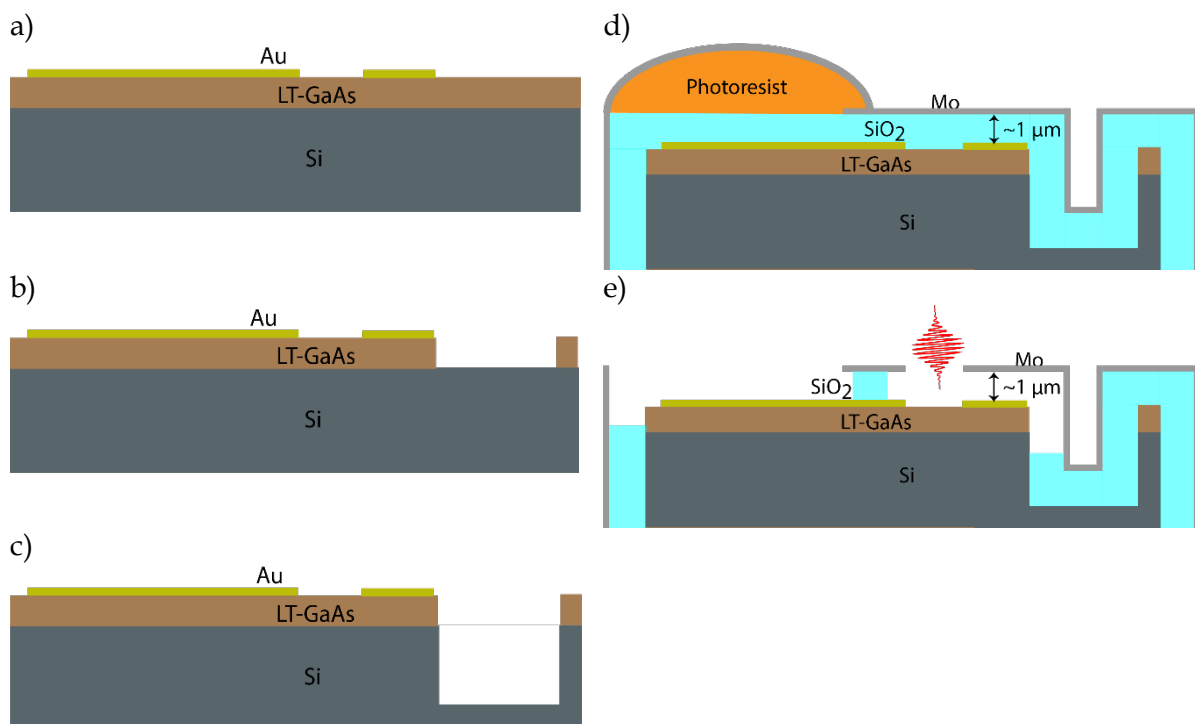


Figure 6.1: General overview of a modified Process, a) the LT-GaAs should be epitaxial grown on a Si wafer, the Au electrodes should be defined with electron beam lithography, like discussed in Chapter 5, b) the GaAs can be removed at selective locations with, for example, a chlorine based reactive ion etch, c) removal of Si with a dry BOSCH process or wet KOH etch to create space for the electron beam. Step d) and e) will be similar to the process flow described in Chapter 5.

The workflow discussed in Chapter 5 for the fabrication of the UFB can be scaled up to the amount of chips which can be fed to a FIB per day. One device is about 1 hour of FIB milling,

which should be done in the future with automatic scripts. For a further scale up in terms of volume the device should be built up on top a silicon wafer. Silicon has the advantage over GaAs that deep trenches can be made with Bosch and KOH etch methods, which both have a high selectivity. The LT-GaAs photoconductive switch should be fabricated on top with either epitaxial growth of LT-GaAs on top of a Si wafer as is done by Kai Mai *et al.*[4]

The UFB chips fabricated in this thesis (equal sided triangles with side lengths of 3 mm) are difficult to handle. If the device is fabricated on a square Si piece and when the entry port has a larger diameter the size of the chip can be increased which makes the device easier to manipulate with a tweezer and hence less prone to failure.

6.2.2 Incorporation in a TEM

The UFB could in principle also be employed in a TEM instead of a SEM, as the concepts and techniques used for insertion of apertures, blankers, etc in the two types of microscopes are quite similar. Moreover, quite some applications for ultrafast-TEM, in fact more than for SEM, have been reported in the literature.[5] To consider TEM applications (typical electron energies 100-300keV, compared to 2-30keV in SEM), it is relevant to know what the induced energy spread at relativistic energies is. At relativistic energies the deflection angle of a deflector can be described as:

$$\alpha = \frac{p_y}{p_x} = \frac{eV_{def}L}{d} \left(\frac{\gamma^2 m_0 c^2}{E_k^2 + 2E_k m_0 c^2} - \frac{1}{m_0 c^2} \right) \quad (6.1)$$

$$\alpha = \frac{eV_{def}L}{E_k d} \left(\frac{\gamma^2 m_0^2 c^4 - E_k^2 - 2m_0 c^2 E_k}{m_0 c^2 E_k + 2m_0^2 c^4} \right) = \frac{eV_{def}L}{E_k d} \beta_r$$

were γ is the Lorentz contraction factor, E_k the kinetic energy, m_0 the electron rest mass and c the velocity of light in vacuum. Two relativistic effects are described with the β term. The first relativistic effect is that, from the perspective of the electron, the length of the deflector is contracted. This affects the charge density on the plate and hence induces a change in the deflection field with a factor γ .

This relativistic correction term is incorporated in the first and second order energy term derived in Chapter 4:

$$\Delta E_1 = \gamma V_0 \alpha_1 \Delta T' = \gamma^2 V_0 \alpha_1 \left(\Delta T - \frac{vL}{c^2} \right) \quad (6.2)$$

$$\Delta E_2 = \gamma 2V_0 \alpha_2 \Delta T' \tau' = 2\gamma^3 V_0 \alpha_2 \left(\Delta T - \frac{vL}{c^2} \right) \tau$$

The terms with an accent denote the reference frame (of the moving electron) which has a velocity v along the electron optical axis. V_0 is the potential along the electron optical axis enhanced by a factor γ due to the contraction of the deflector plate. The second order energy gain has a term depending on the arrival time in the deflector, hence it depends on the pulse

length τ , τ' is the length of the pulse in the moving frame hence it is equal to $\gamma\tau$. The equations are rewritten in a form shown in the Appendix to calculate the energy spread with Matlab, the results are shown in Figure 6.3 for a 120 kV and a 200 kV beam, assuming a reduced brightness of $1 \cdot 10^8$ [A/m²sr²V].

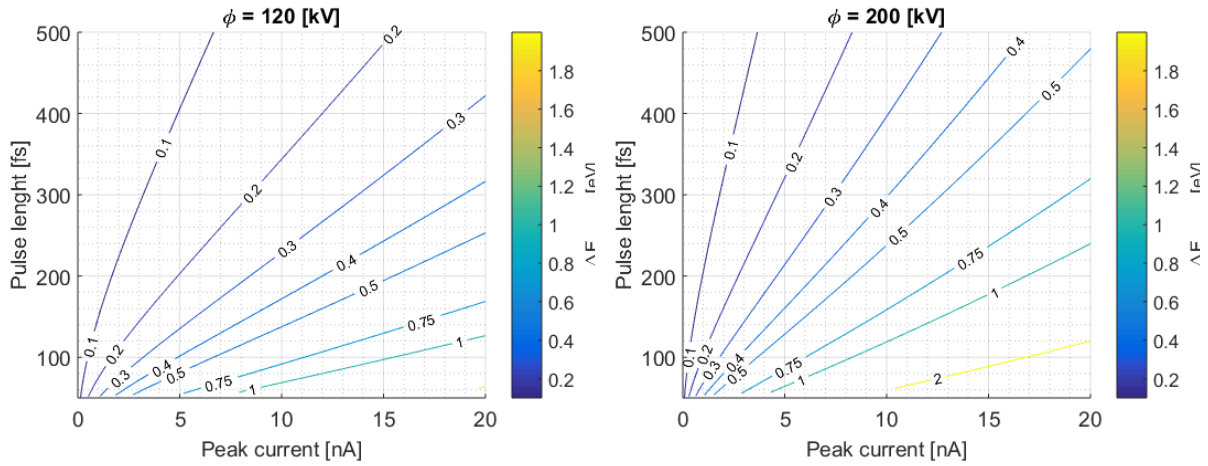


Figure 6.2: Energy spread induced by the UFB at relativistic energies, (a) at 120 keV and (b) at 200 keV, for different FW50 electron pulse lengths and DC beam currents at the UFB.

For pulse lengths above 300 fs the UFB can still be used with only a few 100 meV induced energy spread at 120 kV. For high beam energies, 200 keV, the energy spread increases significantly, but for beam currents below 5 nA and pulse lengths of 400 fs the UFB induces only a small additional energy spread of about 100 meV or less.

6.3 Application for Ultrafast SEM

The added value of a scanning electron microscope is its high surface sensitivity and the possibility to investigate bulk samples. The surface contrast can be utilized in secondary electron (SE) imaging mode where the contrast is strongly dependent on the limited few nanometers escape depth of SE1 electrons (SE's directly excited by the primary electron beam). Hence, in our vision an ultrafast SEM would be mainly used to study the dynamics of carriers in and around semiconductor nanostructures, a proof of principle experiment is given in Chapter 2 of this thesis. Examples of such are patterned photovoltaic devices[6], photodetectors[7], [8] and photoluminescence studies.[9]

Another approach for Ultrafast SEM is to use the electron pulse as a pump, and probe the dynamics by using fluorescence spectra and cathodoluminescence, see Sola-Garcia *et al.*[10]

6.4 Bunching and pulse shaping of femtosecond electron pulses

Electron pulses created by using the photo electric effect and laser-illumination of the electron source have typical pulse durations in the order of 200 fs or longer. In Chapter 4 we calculated that electron pulses of about 100 fs are achievable with an UFB. The reason is that, due to their energy spread, electron pulses broaden when they propagate from the source to the sample. Ultrafast beam blankers are less sensitive to dispersion because they are typically located closer to the sample and the electron pulse does not need to be accelerated from zero velocity

as is the case with photo-emission. Some applications may require a temporal resolution that cannot be achieved with blankers and/or photo-emission sources in an EM, for example, plasmon dynamics occurs on timescales as short as about 10 fs.

In order to overcome the limitation on the electron pulse length, several implementations for electron pulse compressors have been proposed. Most concepts use time-dependent electromagnetic fields to compress electron pulses[11]–[13], except two proposals, there is a novel idea from Grzelakowski and Tromp who propose a spherical electrostatic compressor. [14], [15] Another approach to use electrostatic fields, introduced by Mankos *et al.*, is to use an electrostatic mirror for pulse compression.[16] Already in the 1970s, Ura and co-workers implemented a buncher with RF fields to compress an electron pulse. [17] More recently the groups of Luiten and Baum developed/proposed RF cavities to compress electron pulses.[18], [19] Hilbert and Baum calculated that standing light waves are capable of compressing electron pulses using ponderomotive forces, however laser pulse energies of at least 10 μJ are required. [20]–[22] Optical near fields around a metal tip can be used to create a train of 100 attosecond electron pulses, separated in time by the period of the optical field which is about 2.5 fs as discussed by Feist *et al.* [23] For a pulse compressor a larger separation in time, and thus lower repetition rates, might be required to enable pump-probe experiments. Kealhofer *et al.* have shown that free space terahertz fields can be used for streaking and pulse compression.[11]

A MEMS based system including a photoconductive switch can in principle be used to compress electron pulses with far lower laser pulse energies and at high repetition rates. As shown in this thesis such a system can be directly implemented in the beam line of a commercial SEM. The second order energy gain depends on the arrival time in the UFB, hence the UFB can compress an electron pulse. As shown in Chapter 4, Figure 9, the open UFB generates an energy gain proportional, in some time ranges, to the arrival time in the blanker, in other words it can act as either a pulse expander or pulse compressor. Here we show that the time dependent energy gain can be increased significantly by a relatively small design change. The time dependent energy change can be increased significantly while simultaneously reducing the deflection angle towards zero.

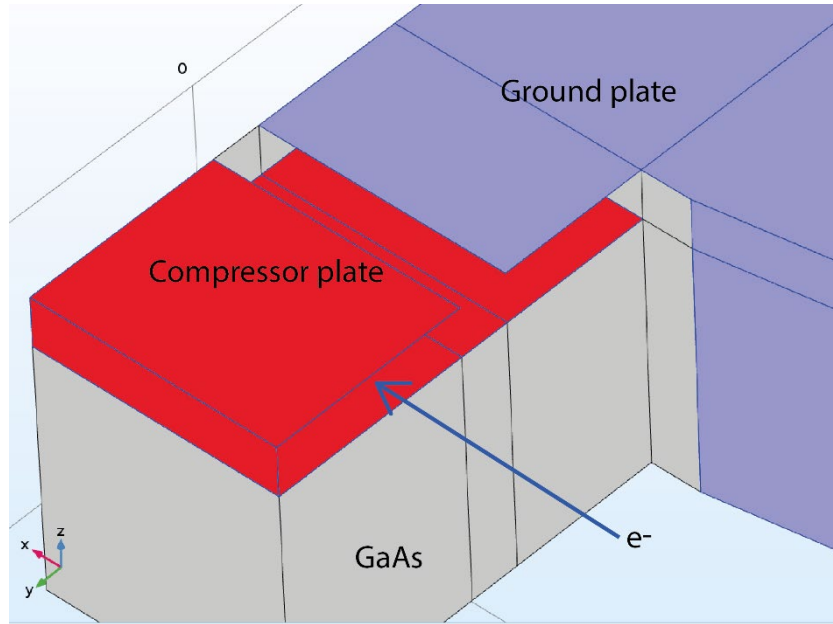


Figure 6.3: Simulation geometry of a pulse compressor or buncher. The red plate has a time dependent voltage generated with a photoconductive switch, the blue arrow indicates the electron optical axis. The electron will be accelerate or decelerate towards the compressor plate depending on the applied voltage. During the time an electron pulse is travelling between the compressor plates a change in voltage will not affect the beam energy, this allows the electron to have a net energy gain or loss.

The temporal focus of a compressor is located at [19]:

$$f = \sqrt{\frac{8q\phi^3}{m_e}} \frac{1}{g_E - g_{disp}} \quad (6.3)$$

where g_E is the linear time-dependent energy gain, equal to 72 meV/fs in the arrival time range -200 to 0 fs in Figure 6.5. Suppose we have a linear chirp of 0.6 eV in a 150 fs FWHM electron pulse. Hence at a beam energy of 30 keV, if the buncher is incorporated in a commercial SEM the temporal focal length should be at a distance of 0.2 m. The required g_E is equal to 26.8 eV/ps, lower than calculated in Figure 6.5 therefore it is easily achievable.

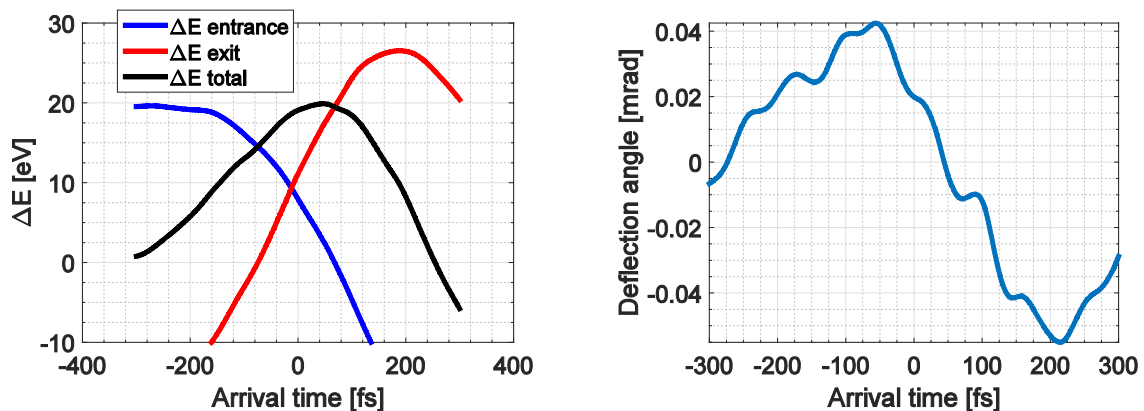


Figure 6.4: (a) Energy gain as function of arrival time. (b) The deflection angle as function of time, notice that the

We performed a calculation where the arrival times of electrons at the sample are calculated in the plane where the temporal focus is located, the result is shown in Figure 6.6, the electron pulse is compressed to a value of about 10 fs. The resulting electron pulse is larger due to

dispersion of the magnetic lens, discussed in Chapter 5, secondly there will be jitter in the system as discussed in chapter 4.[3]

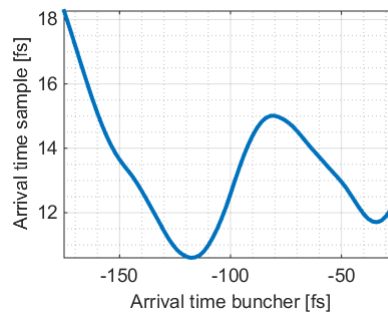


Figure 6.5: Calculated arrival times at the image plane/sample of an electron as function of arrival time in the buncher. The data shows that a 200 fs electron pulse is compressed into a pulse shorter than 10 fs. The energy chirp over the compressed electron pulse is 4.3 eV.

Note that such a time-dependent energy gain is achievable because voltages of up to 50 V can be applied over the photoconductive switch without voltage breakdown. [8]

6.5 Conclusion

We have shown several further improvements can and need to be made such that the ultrafast deflector described in this thesis can be used as an add-on in commercial microscopes. We showed that in principle the system can be used with 100-200kV beams used in STEM. We also showed with calculations that the MEMS chip can be used to manipulate and compress electron pulses with a small change in the geometry of the electrodes.

We would like to acknowledge Diederik Maas for discussing and explaining the TRL model used in this chapter. We also thank Erik Kieft for discussions and ThermoFisher and NWO for funding the valorisation study for this system (NWO-FOM 16VAL11N).

Bibliography

- [1] P. Kruit and I. G. C. Weppelman, "Device and method for generating charged particle beam pulses," WO2016076718 A3, 2016.
- [2] I. G. C. Weppelman, R. J. Moerland, L. Zhang, E. Kieft, P. Kruit, and J. P. Hoogenboom, "Pulse length, energy spread, and temporal evolution of electron pulses generated with an ultrafast beam blanker," *Struct. Dyn.*, vol. 6, no. 2, 2019.
- [3] I. G. C. Weppelman, R. J. Moerland, J. P. Hoogenboom, and P. Kruit, "Concept and design of a beam blanker with integrated photoconductive switch for Ultrafast Electron Microscopy," *Ultramicroscopy*, vol. 184, pp. 8–17, 2017.
- [4] K. Ma, S. Member, R. Urata, D. A. B. Miller, and J. S. Harris, "Low-Temperature Growth of GaAs on Si Used for Ultrafast Photoconductive Switches," *IEEE J. Quantum Electron.*, vol. 40, no. 6, pp. 800–804, 2004.
- [5] A. H. Zewail, "Four-dimensional electron microscopy.," *Science*, vol. 328, no. 5975, pp. 187–93, Apr. 2010.
- [6] M. C. Beard, J. M. Luther, and A. J. Nozik, "The promise and challenge of nanostructured solar cells," *Nat. Nanotechnol.*, vol. 9, no. 12, pp. 951–954, 2014.
- [7] L. Tang *et al.*, "Nanometre-scale germanium photodetector enhanced by a near-infrared dipole

- antenna," *Nat. Photonics*, vol. 2, no. April, pp. 226–229, 2008.
- [8] C. W. Berry, N. Wang, M. R. Hashemi, M. Unlu, and M. Jarrahi, "Significant performance enhancement in photoconductive terahertz optoelectronics by incorporating plasmonic contact electrodes," *Nat. Commun.*, vol. 4, no. 1, p. 1622, 2013.
- [9] M. Merano *et al.*, "Probing carrier dynamics in nanostructures by picosecond cathodoluminescence," *Nature*, vol. 438, no. 7067, pp. 479–482, 2005.
- [10] M. Solà-Garcia, S. Meuret, T. Coenen, and A. Polman, "Electron-induced state conversion in diamond NV centers measured with pump-probe cathodoluminescence spectroscopy," vol. 0, pp. 20–22, 2019.
- [11] A. C. Kealhofer, W. Schneider, D. Ehberger, A. Ryabov, P. Baum, and F. Krausz, "All-optical control and metrology of electron pulses," *Science (80-.)*, vol. 352, no. 6284, pp. 429–433, 2016.
- [12] T. van Oudheusden, P. Pasmans, S. van der Geer, M. de Loos, M. van der Wiel, and O. Luiten, "Compression of Subrelativistic Space-Charge-Dominated Electron Bunches for Single-Shot Femtosecond Electron Diffraction," *Phys. Rev. Lett.*, vol. 105, no. 26, pp. 1–4, Dec. 2010.
- [13] K. E. Echternkamp, A. Feist, S. Schäfer, and C. Ropers, "Ramsey-type phase control of free-electron beams," *Nat. Phys.*, vol. 12, no. 11, pp. 1000–1004, 2016.
- [14] K. P. Grzelakowski and R. M. Tromp, "Temporal and lateral electron pulse compression by a compact spherical electrostatic capacitor," *Ultramicroscopy*, vol. 130, pp. 36–43, 2013.
- [15] L. Yu *et al.*, "Space charge effects and aberrations on electron pulse compression in a spherical electrostatic capacitor," *Ultramicroscopy*, vol. 0, pp. 1–8, 2017.
- [16] M. Mankos, K. Shadman, and B. J. Siwick, "A novel electron mirror pulse compressor," *Ultramicroscopy*, vol. 0, pp. 1–7, 2016.
- [17] T. Hosokawa, H. Fujioka, and K. Ura, "Generation and measurement of subpicosecond electron beam pulses," *Rev. Sci. Instrum.*, vol. 49, no. 5, p. 624, May 1978.
- [18] A. C. Lassise, "Miniaturized RF Technology for Femtosecond Electron Microscopy," Eindhoven University of Technology, 2012.
- [19] A. Gliserin, A. Apolonski, F. Krausz, and P. Baum, "Compression of single-electron pulses with a microwave cavity," *New J. Phys.*, vol. 14, no. 7, p. 073055, Jul. 2012.
- [20] S. a Hilbert, C. Uiterwaal, B. Barwick, H. Batelaan, and A. H. Zewail, "Temporal lenses for attosecond and femtosecond electron pulses," *Proc. Natl. Acad. Sci. U. S. A.*, vol. 106, no. 26, pp. 10558–63, Jun. 2009.
- [21] P. Baum and A. H. Zewail, "4D attosecond imaging with free electrons: Diffraction methods and potential applications," *Chem. Phys.*, vol. 366, no. 1–3, pp. 2–8, Dec. 2009.
- [22] P. Baum and A. H. Zewail, "Attosecond electron pulses for 4D diffraction and microscopy," *Proc. Natl. Acad. Sci. U. S. A.*, vol. 104, no. 47, pp. 18409–14, Nov. 2007.
- [23] A. Feist, K. E. Echternkamp, J. Schauss, S. V. Yalunin, S. Schäfer, and C. Ropers, "Quantum coherent optical phase modulation in an ultrafast transmission electron microscope," *Nature*, vol. 521, no. 7551, pp. 200–203, 2015.

Appendix

The relativistic equations used to calculate the energy spread induced by the UFB, plotted in Figure 6.3, are derived in this Appendix. The non-relativistic equations for the energy spread are derived in Chapter 3 and dependent on the reduced brightness of the beam, the relativistically correct reduced brightness of the electron beam is equal to:

$$B_r = \frac{|q|}{mc^2} \frac{I}{2\pi^2 \beta^2 \gamma^2 \alpha^2 d^2} \quad (6.4)$$

where m is the rest mass of the electron, c the velocity of light, β is equal to v/c and γ is the Lorentz factor.

The equations of the first order energy spread are rewritten as:

$$\begin{aligned} \Delta E_1 &= \gamma V_0 \alpha_1 \Delta T' = \gamma^2 V_0 \alpha_1 \left(\Delta T - \frac{vL}{c^2} \right) \\ \Delta T &= \frac{L}{v}, \alpha_1 = \frac{\alpha \phi}{\beta_r E_0 L \Delta t} \\ \Delta T' &= \gamma \left(\Delta T - \frac{vL}{c^2} \right) = L \left(\frac{\gamma^2 m}{p} - \frac{p}{\gamma m c^2} \right) = L \beta_{E1} \\ \Delta E_1 &= \gamma V_0 \frac{\alpha \phi}{\beta_r E_0 L \Delta t} L \beta_{E1} = \frac{\gamma V_0 \alpha \phi \beta_{E1}}{\beta_r E_0 \Delta t} \end{aligned} \quad (6.5)$$

The half-opening α is linked to the reduced brightness and hence the current in the beam. The second order energy spread is determined as follows:

$$\begin{aligned} \Delta E_2 &= 2\gamma V_0 \alpha_2 \Delta T' \tau' = 2\gamma V_0 \alpha_2 \Delta T' \gamma \tau \\ \Delta T' &= \beta_{E1} L, \tau' = \gamma \tau \\ \Delta E_2 &= \frac{1}{2} \gamma^2 V_0 \frac{L \tau}{\alpha_1^2} \beta_{E1} \end{aligned} \quad (6.6)$$

Acknowledgements

First of all, I would like to thank my promotor Jacob for giving me the opportunity and freedom to do a PhD project in the charged particle optics group. Thank you for all your supervision and guidance! One of your often repeated claims was that when you open a random page in a PhD thesis you will find an error, which might be an interesting point to keep in mind while reading and writing an acknowledgements section.

Pieter, thank you for all the contributions, discussions and ideas to this thesis, your planning and agenda was always so meticulous that it even enabled you to suddenly disappear from dinner/ drinks to set tiles for your mother-in-law on a Sunday evening. Cees Hagen, thank you for your contribution to my EBID work and also for your contributions during project meetings and coffee breaks. Nalan, thank you for your hospitality, help with the SECOM platform, Turkish food and for showing me around Istanbul. Also it was always good politics to be in peaceful terms with at least one office mate.

Apart from the academic staff, there are many others I would like to thank for all their help with this thesis. First of all, I would like to thank Angela for introducing me to the SECOM platform and for all the good times we had working together and traveling to conferences. I was always listening with full attention to stories about India from Sangeetha, my contribution was to spice up the story when needed. For the rest we had really good times going out and traveling and always helping each other when needed, also can't forget the very few occasions you took me seriously, that's why we could get along so well. Marijke, it was great to have you around in the office also, we had to laugh often and I won't forget your thoroughly defined food standards and preparations like stirring clockwise at a certain side of the equator. I'm sure that helped with running your marathons and I still recall that creativity in pronunciation of names wasn't really appreciated. Wilco, I would like to thank you also for all our conversations and discussions and early morning beers. It was always interesting to observe Dutch people who actually are straightforward. Laura, it was great having you in the office too, unfortunately I left the group soon after you arrived.

Mauricio, it was nice to hang around with you for the short time you were in Delft and I never expected to meet you again on a trail deep in the stunning nature of the Pacific Northwest. You are the kind of person who just does stuff, usually that somehow still works out. Takashi Ichimura, it was nice to have you around and it was great to see that you really enjoyed The Netherlands. Hope you can travel back many times. Takashi Doi, Takanori and Hideto it was great to have you also around in the group, the same holds for Minoru though I was afraid going bankrupt during our trip to Monaco. Jayson, it was nice to have you around and I have respect for the decisions you took.

Robert, thank you for the many scientific and physics discussions we had, they gave me many insights, and it was great to help each other by spending hours on the system to get the data we needed. Also, thank you for teaching me how to use Comsol. for the many trips we did and all the beer we drank together. The graphics you made helped me explain the project in scientific presentations and papers.

Yen and Ting, I would like to thank you both for the many hours we spent together often till very late night, to hear your interesting perspectives on Chinese society and your perspectives on the world with great Chinese food. I'm sure your daughter Elene, is going to do great, I won't say whose contribution is going to ensure that.

Thomas, you added quite some energy to the CPO group. Leon, thank you for the many good scientific discussions we had with a drink and I won't forget the set of really nice videos you made with Diederik. Christiaan Z, thank you for your advice and discussions regarding the fabrication work I did in the cleanroom. It has helped me in my research, the exponential extrapolations based on a few data points you made were sometimes quite interesting. Martin, also many thanks for your feedback, tips and advice regarding my cleanroom work and for hanging out at Locus. Chris Post, thank you for teaching me how to do EBID and training me on how to use the SEM. Kerim, thank you for showing me the good Turkish places in the area. Maurice, thank you for all the nice scientific discussions. Gaudham, Aditya, Ryan, Luc, Neda, Aya and Xiaoli also came later during my time in the group and I recall fun and enjoyable time with all of you too. Shammi, thank you for inviting me to your wedding, that was an interesting experience for me.

The support, training and help from technicians in the group of my PhD project has been essential. Carel, thank you for all the knowledge on microfabrication, both theoretical and practical that I have learned from you. We spent many hours in the cleanroom together. Your stories met my threshold to believe them, also thanks for organizing the barbeques. Ruud van Tol, thank you for the many hours you put in the mechanical design and the enthusiasm with which you spoke about mechanical engineering. Jan de Loeff bedankt voor al je hulp gedurende mijn project, daarnaast heb ik veel van je geleerd over vacuümtechniek. Alles wat je maakte voor mij in de werkplaats zag eruit als een juweel, dat zou iets te maken kunnen hebben met mijn kantoorgenoten. Cor, Wim en Ger hebben ook veel essentiële onderdelen gemaakt, bedankt! Dustin, thank you for the many interesting conversations we had about FEI and American society over a beer, I have good memories about that, still, Roller Derby appears to me as a higher order aberration in sports. You, Meg and Emily will have a good time in Delft. Frans, thank you for everything I learnt from you about Labview, you did a great job and was modest about it, Monday till Friday 15:59:00 so you could be present for your second responsibility to keep beer flowing at the Vvtp bar. Han and Paul also thanks for the electronics and software assistance. Raymond, thank you for helping me out with the electronics for the frequency divider.

Anjella thank you for all your effort and compassion and help with all administrative issues. Malee also thank you for your help, and Margaret also thank you for the help with travel related things.

Aurele, thank you for letting us borrow the CPU cluster at the Optics group essential for the Comsol calculations in this thesis. Also, thank you for all the training you gave during my master thesis project which helped me during my PhD. I would also like to acknowledge Ying Tang and Lei Wei for their help with the CPU cluster and I would like to acknowledge Paul Planken for discussions regarding photoconductive switches.

Thijs thank you for building and verifying the dispersion compensation system as described in the second chapter of this thesis. Also it was nice working with you, discussing physics and having conversations about all kind of topics. Mathijs, thank you for the contribution to the second chapter of this thesis and the improvements you made on the setup, for hanging out and for all the scientific discussions. Miranda, it was nice to work with you on your master research project. Unfortunately I wasn't fully involved during the initial phase of your project. Yoram, I won't forget you and it was fun to have you in the group too. Martijn and Daan, it was nice working with you on the SECOM systems and hanging out in the Vvtp bar.

Erik Kieft, thank you for your comments and feedback on the project. Diederik Maas, thank you for introducing me to the concept of technology readiness levels used in the last chapter of this thesis.

Elizabeth, Daan and Ali, it is cool that you joined the Imaging Physics department. Daan, I have good memories from many years ago when we hung out in Barcelona and after your detour to the US, it is nice that we met again in the same department.

Life is good.

List of publications

Publications related partly or in full to the work described in this thesis:

- [1] M. W. H. Garming, I. G. C. Weppelman, M. Lee, T. Stavenga, P. Kruit, J. P. Hoogenboom, *Ultrafast Scanning Electron Microscopy with sub-micron optical pump resolution* (in preparation) (Chapter 2)
- [2] R. J. Moerland, I. G. C. Weppelman, M. W. H. Garming, P. Kruit, and J. P. Hoogenboom, *Time-resolved cathodoluminescence microscopy with sub-nanosecond beam blanking for direct evaluation of the local density of states*, **Optics Express** 24 (21), 24760-24772 (2016) (Chapter 2)
- [3] I. G. C. Weppelman, R. J. Moerland, J. P. Hoogenboom, P. Kruit, *Concept and design of a beam blanker with integrated photoconductive switch for ultrafast electron microscopy*, **Ultramicroscopy** 184, 8-17 (2018) (Chapter 3)
- [4] I. G. C. Weppelman, R. J. Moerland, L. Zhang, E. Kieft, P. Kruit, and J. P. Hoogenboom, *Pulse length, energy spread, and temporal evolution of ultrafast electron pulses generated with a laser-triggered beam blanker*, **Structural Dynamics** 6, 024102 (2019) (Chapter 4)

Other publications:

- [5] I. G. C. Weppelman, P. C. Post, C. T. H. Heerkens, C. W. Hagen, and J. P. Hoogenboom, *Fabrication of narrow-gap nanostructures using electron-beam induced deposition etch masks*, **Microelectronic Engineering** 153, 77-82 (2016)
- [6] A. C. Narvaez, I. G. C. Weppelman, R. J. Moerland, J. P. Hoogenboom, and P. Kruit, *Confocal filtering in cathodoluminescence microscopy of nanostructures*, **Applied Physics Letters** 104, 251121 (2014)
- [7] A. C. Narvaez, I. G. C. Weppelman, R. J. Moerland, N. Liv, A. C. Zonneville, P. Kruit, and J. P. Hoogenboom, *Cathodoluminescence microscopy of nanostructures on glass substrates*, **Optics Express** 21 (24), 29968 (2013)
- [8] R. J. Moerland, I. G. C. Weppelman, M. Scotuzzi, J. P. Hoogenboom, *Nanoscale imaging of light-matter coupling inside metal-coated nanocavities using pulsed electron beams*, **NanoLetters** 18, 6107-6112 (2018)
- [9] M. W. H. Garming, I. G. C. Weppelman, P. de Boer, F. Perona Martinez, R. Schirhagl, J. P. Hoogenboom, and R. J. Moerland, *Nanoparticle discrimination based on wavelength- and lifetime-multiplexed cathodoluminescence microscopy*, **Nanoscale** 9, 12727 (2017)

Patents:

- [10] A. C. Narvaez, I. G. C. Weppelman, J. P. Hoogenboom, *Method for positioning an optical component in a light imaging device for cathodoluminescence inspection and apparatus arranged for applying said method*, **WO2017014626, N2015192**
- [11] I. G. C. Weppelman and P. Kruit, *Ultrafast electron pulse generator*, **NL2013801** (Chapter 3)

Curriculum Vitae

Gerward Weppelman, born in Spijk (Lingewaal), January 29th, 1987.

Bachelor degree in Applied Physics, Delft University of Technology. Thesis subject 'Flashing geïnduceerde instabiliteit in de CIRCUS opstelling met vier parallelle kanalen' , received in 2008.

Master degree in Applied Physics, Delft University of Technology, Thesis subject: 'Design and Validation of a Terahertz Near-Field Imaging Setup based on a Fiber Probe', received in 2011

Internship: 'Investigation of the Purcell factor of Nitrogen-Vacancy Diamond Centers in Diamond Nanoparticle', The institute of Photonic Sciences, Barcelona

PhD candidate in the Charged Particle Optics group, started in 2011, subject: 'Ultrafast electron beam blanker' (this dissertation)